

M. Tech. Kirti Bhushan Mishra

**Experimental investigation and CFD
simulation of organic peroxide pool fires
(TBPB and TBPEH)**

Die vorliegende Arbeit entstand an der BAM Bundesanstalt für Materialforschung und -prüfung.

Impressum

**Experimental investigation and CFD simulation
of organic peroxide pool fires (TBPB and TBPEH)**

2010

Herausgeber:

BAM Bundesanstalt für Materialforschung und -prüfung

Unter den Eichen 87

12205 Berlin

Telefon: +49 30 8104-0

Telefax: +49 30 8112029

E-Mail: info@bam.de

Internet: www.bam.de

Copyright © 2010 by

BAM Bundesanstalt für Materialforschung und -prüfung

Layout: BAM-Arbeitsgruppe Z.64

ISSN 1613-4249

ISBN 978-3-9813550-6-2

Experimental investigation and CFD simulation of organic peroxide pool fires (TBPB and TBPEH)

Von der Fakultät für Ingenieurwissenschaften, Abteilung Maschinenbau und
Verfahrenstechnik der

Universität Duisburg-Essen

zur Erlangung des akademischen Grades

eines

Doktors der Ingenieurwissenschaften

Dr.-Ing.

genehmigte Dissertation

von

M. Tech. Kirti Bhushan Mishra

aus Cuttack, Indien

Gutachter: Univ.-Prof. Dr. rer. nat. Christof Schulz

Univ.-Prof. Dr. rer. nat. Axel Schönbacher

Vorsitzender: Univ.-Prof. Dr.-Ing. Johannes Wortberg

Tag der mündlichen Prüfung: 12. Mai 2010

Acknowledgements

This PhD thesis has been carried out in the context of a doctoral programme during my work as a research assistant in the working group on “Explosive Substances of Chemical Industries”, at the BAM Federal Institute for Materials Research and Testing.

I express my deep sense of gratitude to Prof. Dr. rer. nat. Axel Schönbacher, Department of Chemical Engineering I, University of Duisburg-Essen, campus Essen, for enabling this opportunity to work under his kind supervision. I am very thankful for his continuous technical guidance and scientific discussions. A very sincere thank and deep appreciation to Prof. Dr. rer. nat. Christof Schulz, Institute for Combustion and Gas Dynamics, Department of Mechanical Engineering, University of Duisburg-Essen for his expert suggestions and comments on different topics of interest.

I would like to thank especially Prof. Dr. rer. nat. Klaus-Dieter Wehrstedt, Head of the Division II.2 “Reactive Substances and Systems” at BAM. I am very grateful for his expert suggestions, numerous discussions on various topics and his purposeful way of working which always motivated and supported me.

I would also like to thank Dr. rer. nat. Heike Michael-Schulz, Head of the Working Group II.23 “Explosive Substances of Chemical Industries” at BAM for providing excellent support and co-operation for conducting the experiments.

Also, I wish to thank Dr.-Ing. Michael Rudolph and Dr. rer. nat. Marcus Malow from BAM II.2 and Dr.-Ing. Anja Hofmann and Dr. rer. nat. Simone Krüger from BAM VII.3 for the fruitful discussions and technical know hows, particularly for experimental work. My special thanks to all colleagues Dipl.-Ing. Gerhard Reinhard Zemke, Dipl.-Ing. Jochen Kebben, Dipl.-Ing. Kim Stattaus, Mr. Klaus-Dieter Nicolaus, Ms. Bianca Fourier, Dipl.-Ing. Kai-Uwe Ziener, Dipl.-Ing. Martin Beckmann Kluge and Dipl.-Ing. Reinhold Wendler of BAM for co-operation and great assistance in the implementation of experimental studies. Mr. Michael Bulin is thankfully acknowledged for the cluster administration of BAM II for carrying out simulations. I am very thankful to Dr. rer. nat. Iris Vela, Dipl.-Phys. Peter Sudhoff and Dr. rer. nat. Markus Gawlowski from the Institute of Chemical Engineering I, University of Duisburg-Essen, Essen campus, for the excellent cooperation, friendly support and assistance in computational work.

My special thanks goes to Dr. Frank Steinbach, Patent Attorney, Zimmermann and Partner, Berlin for shaping the IDEAS into nice form of various patents.

I am also very thankful to joshi ji and ashwini bhabhi for the arrangement of refreshing tea-breaks and the companies of purva and maololan during the lunch time.

Shri Narsingha Devay Namah

*Dedicated to
my dear parents (Shri Narayan Prasad Mishra and Shrimati
Priyambada Mishra) and my loving brothers (Shri Vibhuti Bhushan
Mishra, Shri Shashi Bhushan Mishra, Shri Ravi Bhushan Mishra and
Shri Chandra Bhushan Mishra) and their families and to all my beloved
ones the company of whom i missed a lot.....*

ABSTRACT

Time averaged mass burning rate ($\overline{\dot{m}}_f''$), flame length (\overline{H}), temperature (\overline{T}), irradiance (\overline{E}) and surface emissive power (\overline{SEP}) of TBPB (tert -butyl peroxybenzoate) and TBPEH (tert-butyl peroxy-2-ethylhexanoate) pool fires are measured for six pool diameters ($d = 0.059$ m, 0.107 m, 0.18 m, 0.5 m, 1 m and 3.4 m) at BAM in house and outside test facility.

The measured heats of combustion ($-\Delta h_c$) of TBPB and TBPEH are 30113 kJ/kg and 34455 kJ/kg and the specific heat capacities at constant pressure (c_p) are 1.8 kJ/(kg K) and 2.1 kJ/(kg K) respectively.

The measured $\overline{\dot{m}}_f''$ of TBPB and TBPEH pool fires are in the range of $0.37 \text{ kg}/(\text{m}^2 \text{ s}) \leq \overline{\dot{m}}_f'' \leq 0.83 \text{ kg}/(\text{m}^2 \text{ s})$ and show little dependence on the pool diameter d , and are four to sixty times higher (for $d = 1$ m) than that of hydrocarbon pool fires. It is shown that the mass burning rates of the investigated organic peroxides can be represented as an exponential function of the self-accelerating decomposition temperature (SADT). Low SADT implies that the organic peroxide pool fires burn at a much higher $\overline{\dot{m}}_f''$ than hydrocarbon pool fires.

Fuel Froude numbers (Fr_f) of TBPB and TBPEH are 5 to 100 times (depending on d) higher than for hydrocarbon pool fires. Due to higher Fr_f the \overline{H} of TBPB and TBPEH (measured with a S-VHS Videocamera) are found to be two times larger ($d = 1$ m) than corresponding pool fires of hydrocarbons. Heskestads flame length correlation predicts the \overline{H}/d ($d = 3.4$ m) of TBPB and TBPEH pool fires much better than Thomas and Fay correlations.

The measured time averaged flame temperatures \overline{T} ($d = 3.4$ m) for TBPB and TBPEH pool fires are in the range of $1400 \text{ K} \leq \overline{T} \leq 1500 \text{ K}$ and are 200 K to 300 K higher than for JP-4, kerosene and gasoline.

The irradiances of the TBPB and TBPEH pool fires measured by radiometers are \overline{E} ($\Delta y/d = 0.3$) = 45 kW/m² and $\overline{E} = 98 \text{ kW}/\text{m}^2$ which are two to ten times higher in comparison to the corresponding n-pentane, super gasoline and diesel pool fires. So the thermal safety distances for organic peroxide pool fires are larger by a factor four in comparison to the hydrocarbon pool fires.

An infrared thermography system is used for the determination of \overline{SEP} of TBPB and TBPEH pool fires. The values of surface emissive power for TBPB and TBPEH are \overline{SEP} ($d = 3.4$ m) = 196 kW/m² and $\overline{SEP} = 258 \text{ kW}/\text{m}^2$ and thus the \overline{SEP} are by a factor of approximately two higher than for hydrocarbon pool fires.

A self-sustained pulsating \overline{H}/d ('W'-Effect) is found in TBPB pool flames and is further analysed to explain the reason of occurrence on the basis of chemical structure of the fuel and discontinuous heat flux back from flame to the liquid pool.

CFD simulations of TBPB and TBPEH pool fires at $d = 0.18$ m, 0.5 m, 1 m, 3.4 m and 8 m are carried out using the Unsteady Reynolds Averaged Navier Stokes (URANS) equations. The three-dimensional geometries have been discretized with unstructured hybrid grids, with the number of cells in the range of 1 million. Depending on the grid resolution and the pool diameter time steps of $0.0001 \text{ s} \leq \Delta t \leq 0.01 \text{ s}$ for the CFD simulations are used. For solving the discretized equations a finite volume based implicit solver ANSYS CFX has been used. For modelling the combustion, stoichiometric combustion for both peroxides are assumed. The temperature dependence of the reaction rate has been determined by the Arrhenius approach. For modelling the combustion eddy dissipation concept (EDC) model has been used. For turbulence buoyancy modified k- ϵ and SAS (Scale Adaptive Simulation) turbulence models are used. For the thermal radiation and soot mass fraction discrete transfer radiation model and Magnusson soot model have been used.

A new method is suggested for the prediction of mass burning rate (\overline{m}_f'') by CFD simulation. Both peroxide pool fires show approximately constant mass burning rate independent of d whereas \overline{m}_f'' of TBPEH are under predicted at the beginning but show relatively good agreement with measurements for large pool diameters ($d = 1$ m). In case of TBPB the CFD simulation over predicts the mass burning rate \overline{m}_f'' of small TBPB pool fires and shows a continuous decrease with d . CFD predicts the flame length \overline{H} close to the measured data provided that the constants in Thomas equation are modified.

The CFD predicted time averaged surface emission flame temperatures of TBPB and TBPEH pool fires ($d = 3.4$ m, 1437 K and 1542 K) are in good agreement with the measured time averaged flame temperatures.

The CFD predicted \overline{SEF} for TBPB and TBPEH pool fires ($d = 3.4$ m, 217 kW/m² and 288 kW/m²) are also in agreement with the measured values. From the CFD predicted irradiance $\overline{E}_{\text{CFD}}$ it is possible to determine the thermal safety distances from large pool fires of hydrocarbons and organic peroxides.

Nomenclature

A_P	Pool surface	m^2
c_p	Specific heat capacity	$J/(kg\ K)$
D	Diffusion coefficient	m^2/s
d	Pool diameter	m
E	Irradiance	W/m^2
e	Specific total energy	J/kg
E_A	Activation energy	J/mol
f	Frequency of pulsation	$1/s$
f_{rad}	Radiative heat fraction	
g	Gravitational acceleration	m/s^2
Δh_v	Specific enthalpy of vaporisation	J/kg
$-\Delta h_c$	Specific enthalpy of combustion	J/kg
H	Flame length	m
k	Reaction rate constant	reaction dependent
K	Conductive heat transfer coefficient	$W/(m\ K)$
L	Latent heat	$J/(kg\ K)$
\dot{m}	Mass flow	kg/s
\dot{m}_f''	Mass burning rate	$kg/(m^2s)$
n	Molar quantity	mol
p	Pressure	N/m^2
\dot{Q}_c	Heat release rate due to combustion	W
\dot{Q}^*	Dimensionless number	
\dot{Q}_{rad}	Heat rate due to radiation	W
q	Heat quantity	J

R	Universal gas constant	J/(mol K)
r	Radial coordinate	m
$r_{1/e}$	Radial coordinate where the variable value is 1/e	m
r_{st}	Stoichiometric ratio	
SEP	Surface Emissive Power	W/m ²
T	Temperature	K
t	Time	s
u	Velocity of flame gases	m/s
U	Hydrodynamic velocity	m/s
V	Volume	m ³
v_a	Burning velocity	m/s
x	Axial distance above pool surface	m
y	Horizontal distance from pool centre	m
Δy	Distance between pool rim and receiver	m

Greek Letters

α	Convective heat transfer coefficient	W/(m ² K)
β	Exponent of temperature	
γ	Small fraction of flame zone thickness	
ε_F	Flame emissivity	
θ	Flame tilt and angular coordinate	°
κ	Absorption coefficient	1/m
λ	Wavelength	nm
μ	Dynamic viscosity	kg/(m s)
ρ	Density	kg/m ³
σ	Stefan-Boltzmann constant	W/(m ² K ⁴)
τ	Atmospheric transmissivity	
$\varphi_{F,R}$	View factor from flame to receiver	
χ	Mass fraction	

Indices

a	Ambient conditions, air
c	Combustion
cl	Clear flame zone
ent	Entrainment
f	Fuel
F	Flame
g	Gas
max	Maximum value
P	Product
rad	Radiation
v	Fuel vapour
w	Wind

Abbreviations

CFD	Computational Fluid Dynamics
DSC	Differential Scanning Calorimetry
DTBP	Di-tert-Butyl peroxide
EDC	Eddy Dissipation Concept
INP	Di-isononanoylperoxide
LES	Large Eddy Simulation
OSRAMO	Organised Structure Radiation Model
RANS	Reynolds Averaged Navier-Stokes
S	Gibbsian surface
SADT	Self Accelerating Decomposition Temperature
SAS	Scale Adaptive Simulation
SEP	Surface Emissive Power
TBPB	tert-Butyl peroxybenzoate
TBPEH	tert-Butyl peroxy-2-ethylhexanoate
TBHP	tert-Butyl hydroperoxide
URANS	Unsteady Reynolds Averaged Navier-Stokes

Miscellaneous

$\bar{(\quad)}$	Time averaged value
$\tilde{(\quad)}$	Favre averaged value
∇	Divergence
$\langle \rangle$	Surface averaged
$\langle \rangle$	Value averaged over cross section of the flame

Contents

1	Introduction	1
2	Theoretical Background	4
2.1	Introduction	4
2.2	Dynamics of pool fires	4
2.2.1	Mass burning rate	7
2.2.1.1	Theory of burning rate according to Hertzberg	11
2.2.1.2	Effect of lip height, thickness and pan material	12
2.2.2	Flame length	12
2.2.2.1	Flame length model according to Thomas	15
2.2.2.2	Flame length model according to Steward	15
2.2.2.3	Flame length model according to McCaffrey	16
2.2.2.4	Flame length model according to Moorhouse	17
2.2.2.5	Flame length model according to Heskestad	17
2.2.2.6	Flame length model according to Fay	18
2.2.2.7	Effect of unsteadiness	20
2.2.3	Flame temperature and flow velocity	20
2.2.4	Adiabatic flame temperature	24
2.2.5	Thermal radiation	24
2.2.5.1	Point source model	24
2.2.5.2	Conventional and modified solid flame radiation model	26
2.2.5.3	View factors	30
2.2.5.4	Atmospheric absorption	32
2.2.6	Organised Structures Radiation Models (OSRAMO II, OSRAMO III)	32
2.3	Organic peroxides	33
2.3.1	Self Accelerating Decomposition Temperature of organic peroxides	36
2.3.2	Fire and explosion hazards of organic peroxides	36
2.4	Modelling and simulation of pool fires	37
3	Experimental Investigations	39
3.1	Description of measuring instruments	39
3.1.1	Dynamic Differential Calorimetry (DDC)	39
3.1.2	Thermocouples	41
3.1.3	Thermographic camera	42
3.1.4	Radiometers	43
3.2	Experimental set-ups for small and large scale fire tests	44

3.2.1	Construction	44
3.2.2	Fuels	45
3.2.3	Mass burning rate	46
3.2.4	Flame length	46
3.2.5	Flame temperature	46
3.2.6	Surface emissive power	47
3.2.7	Irradiance	47
3.3	Description of packaged material fire test	49
3.3.1	Flame length	51
3.3.2	Temperature measurement	51
3.3.3	Irradiance measurement	52
4	CFD (Computational Fluid Dynamics) Simulation	53
4.1	Introduction	53
4.2	Modelling methodology	54
4.2.1	Geometry, mesh and boundary conditions	54
4.2.2	Transport models	55
4.2.2.1	Multi-component flow	55
4.2.2.2	Turbulence models	56
4.2.3	Thermodynamic properties	57
4.2.4	Combustion model	58
4.2.4.1	The eddy dissipation concept (EDC) model	58
4.2.5	Soot models	60
4.2.5.1	Soot formation	60
4.2.6	Radiation model	62
4.2.6.1	Discrete transfer model	62
4.3	Solution strategy	63
5	Results and Discussion	66
5.1	Mass burning rate	66
5.1.1	Mass burning rate as a function of pool diameter	66
5.1.2	Mass burning rate as a function of Self-Accelerating Decomposition Temperature (SADT)	68
5.1.3	CFD prediction	70
5.2	Visible flame length	73
5.2.1	Visible flame length as a function of pool diameter	75
5.2.2	Visible flame length as a function of fuel Froude number	76
5.2.3	Flame length prediction according to the models of Thomas and Fay	76
5.2.4	Flame length prediction according to Heskestad's model	78
5.2.5	CFD prediction	79
5.3	Turbulent organised structures	80
5.4	'W'-effect in a TBPB pool flame	82
5.5	Flame temperature	84
5.5.1	Instantaneous flame temperature field	84
5.5.2	CFD prediction of time averaged flame surface emission temperature profile	85

5.5.3	Time averaged flame temperature field	87
5.5.4	Time averaged mass fraction of combustion products	89
5.5.5	CFD prediction of the axial flame temperature profile	90
5.5.6	CFD prediction of the flame temperature in packaged fire test . . .	91
5.6	Flow velocity of flame gases	95
5.6.1	CFD simulation	96
5.7	Flame irradiance	101
5.7.1	CFD prediction of irradiance in a fire test of packaged fuel	105
5.8	Surface emissive power	105
5.8.1	Prediction of surface emissive power from thermograms and from CFD	105
5.8.2	Soot mass fraction	109
5.9	Validation of CFD simulation	110
6	Conclusions and Future Work	113
	References	115
	List of trade marks, patents and publications	125
	Curriculum Vitae	129

Chapter 1

Introduction

The demand of safe processing of hazardous substances in chemical industries is steadily increasing due to strict regulations laid down by the regulating authorities to prevent disasters. A such major accident happened in the early morning (0520 GMT) of 11th December 2005 when an overflow of unleaded petrol took place in Hertfordshire Oil Storage Terminal (HOSL) (also known as Buncefield Oil Depot) which finally converted into one of the worst ever industrial accident seen in Europe [1, 2]. It is reported that the



FIGURE 1.1: Buncefield Accident (London,UK, 2005)

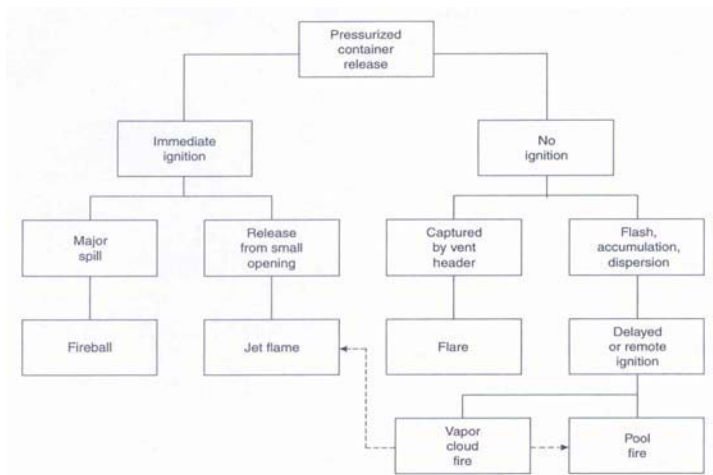


FIGURE 1.2: Event tree for release of flammable material [3]

vapour cloud covering an extensive area exploded due to an unknown source of ignition which is shown in Fig. 1.1. A continuous overflow of petrol led to large shape of pool and mixture of petrol and air simultaneously. The intensity of this disaster could be imagined by the fact that it took four days until the fire was completely extinguished. However the disaster left many unanswered questions behind. Despite of all safety precautions such accidents whether small or large, can occur due to ignorance, mistake by personnel or due to the failure of mechanical devices. An event tree of a series of consequences which could occur as a result of release of flammable material is shown in Fig. 1.2. The pressurised release of any flammable material may lead to a jet flame (immediate ignition) or a pool fire (delayed ignition). The right half of the Fig. 1.2 depicts the occurrence of a pool fire [1].

A wide variety of different hydrocarbon jet and pool fires have been studied by many authors in the past. There are some energetic materials e.g. organic peroxides which have been continuously produced and used by the chemical industries as an initiator for free radical polymerisation in polymer production. Because they are unstable compounds their safe storage and transportation is of great interest. They are normally available in standard packages, stored in large containers made of either metal or plastic. In Germany there are corresponding regulations for the storage in packages, which are based on mass burning rate of organic peroxides in packagings and also taking into account the emerging

thermal radiation protection and safety distances. So-called pool fires can arise if for example the packaging or container is damaged and thus liquid organic peroxide leaks. In the relevant literature both experimental and simulated data on pool fires of flammable liquids such as gasoline, kerosene and other petroleum products can be found. Pool fires of organic peroxides were previously investigated at BAM (Federal Institute for Materials Research and Testing, Berlin) for diameters in the range between 0.03 m and 3.4 m. Little is known about detailed flame characteristics of different organic peroxides so far. A recent PhD thesis from the BAM group investigated pool fires of di-tert butyl peroxide (DTBP). Pool fires of organic peroxides are of great importance from safety point of view in order to calculate effective methods of protection and safety distances.

The purpose of the present work is to experimentally and numerically investigate and to characterise the pool flames of two organic peroxides [tert-butyl peroxybenzoate (TBPB) and tert-butyl peroxy-2-ethylhexanoate (TBPEH)] in comparison to hydrocarbons. A fire from packaged material is compared to the equivalent shape of a pool fire and is numerically investigated. The fundamental flame characteristics, e.g. mass burning rates, flame lengths, flame temperatures and irradiances of six pool flames are measured for both of the peroxides. CFD simulations were performed for five pool diameters of both peroxides and the respective flame characteristics were simulated. A finite volume based implicit solver Ansys CFX-11 has been used for solving unsteady Reynolds Averaged Navier-Stokes (URANS) equations.

The knowledge gained from the pool fire characteristics of previously investigated organic peroxide i.e. DTBP showed that there are significant differences between pool fire characteristics of hydrocarbons and of organic peroxides. Therefore, as an addition in the existing knowledge two other organic peroxide (TBPB and TBPEH) pool fires are experimentally investigated and simulated with CFD.

Chapter 2

Theoretical Background

2.1 Introduction

Liquid fuel spill and pool fires represent potential hazards in many applications ranging from accidents at industrial plants, using combustible liquids, sometimes intended fire to properties with flammable fuels. A pool is characterised by a confined body of liquid fuel that typically has a depth greater than 1 cm. A pool can result due to a liquid fuel release that collects in a low spot, such as a trench, or can exist as a result of normal storage of fuels in tanks and containers. In the following sections the different characteristics of pool flames are discussed in detail. The development in the existing understanding is described in subsequent subsections.

2.2 Dynamics of pool fires

The structure of most pool fires may be split into a number of fairly well-defined zones [3, 4, 8, 9, 10, 11]. These zones are shown in Fig. 2.1 and the physical processes along with their technical importance is described below.

- The liquid fuel itself: In deep pools there may be a significant convective flow within the fuel which can affect the fuel vaporisation rate and hence influence the “external” characteristics e.g. size and visibility of the fire; the interaction between

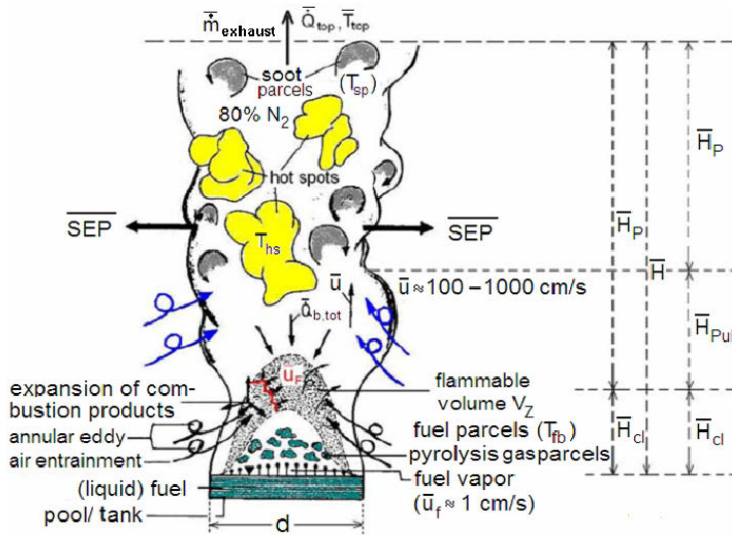


Fig. 2.1(a)

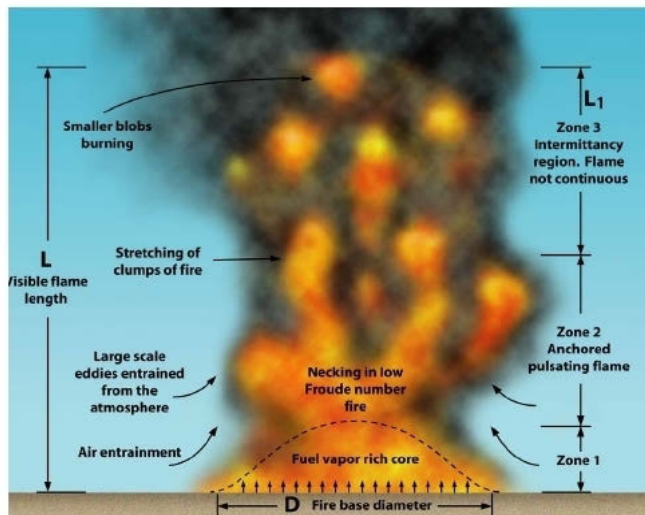


Fig. 2.1(b)

FIGURE 2.1: Existence of three zones in a turbulent buoyant diffusion flame defined by Schönbucher (Fig. 2.1 (a)) [11] and Raj (Fig. 2.1 (b)) [10]

the fuel and the vessel which surrounds it (if any) may also have a big impact on the burning behaviour.

- A zone of unburnt fuel vapour above the liquid fuel, which is usually close to a constant conical shape.
- A combustion region above this zone (also known as continuous flame regime), but here there is intermittency (also known as intermittent regime or pulsation zone) and obvious turbulence in the reactive flow.
- The non-reacting buoyant plume (plume zone or plume regime), which is generally fully turbulent in nature and is characterised by decreasing velocity and temperature with height and lateral position.

Each individual zone has been extensively analysed in the literature and numerous studies have described the different parameters controlling the behaviour of each zone and their interactions [13]. The resulting pool is then quantified via a number of measurable quantities. The main “measurable quantities” associated to a pool fire are:

- **Burning rate or mass loss rate (\dot{m}_f):** these quantities are closely related to the heat release rate. The mass loss rate is generally expressed in terms of kg/s. Historically, burning rate has been expressed in terms of a regression rate given in mm/min (i.e. the surface is lowered by a number of mm per minute as the fuel is consumed in the fire).
- **Heat release rate (\dot{Q}_c):** the total amount of heat energy released by the fire, generally expressed in kilowatts (kW) or megawatts (MW). For pool fires this is sometimes expressed in terms of heat release rate per unit area (i.e. kW/m²).
- **Flame length (H):** generally expressed in metres (m). The flame tip is often defined to be the point of 50% intermittency i.e. the length it maintains for more than 50% of time during the steady burning period [10]
- **Flame temperature (T):** actually a distribution of temperatures (instantaneous and time averaged), often given as mean centreline values, with radial variations [11].
- **Smoke production rate:** may be expressed in m³/s or kg/s.

- **Radiation** (E , SEP): described either as the irradiance or emissive power at a given point in space (kW/m^2). Sometimes also specified as the sum of all heat lost by radiation (kW) and often expressed as a percentage of the total heat release rate i.e. fraction of radiation f_{rad} [12].

A number of physical characteristics of the pool then control these measurable quantities. These physical characteristics vary from the very simple to the complex. A simple abbreviated list will include:

- Pool geometry (diameter, depth, substrate)
- Fuel composition
- Ventilation conditions (wind, forced or restricted ventilation, etc.)
- Surrounding geometry (open air, compartment height, proximity to walls etc.)
- Nature of the bounding materials (conductive or insulated) i.e. those used to construct the lip of liquid pool fire trays.

Physical characteristics associated with the pool fire have a direct impact on the different zones and this impact is generally defined by means of measurable quantities. It is important to note that concept of zones and description by measurable quantities are a practical way to describe a pool fire. They are useful to simplify a very complex problem but do not correspond to the fundamental physical processes that control the combustion and different transport processes. These will be discussed as follows.

2.2.1 Mass burning rate

Pool fire research is considered to have started with the work of Bilnov and Khudiakov [5] (Fig. 2.2) who performed a wide range of experiments on gasoline like liquids in pans ranging in size from a fraction of a centimetre upto nearly 30 meters in diameter. The correlation proposed shows that burning rates depend on the ratio of heat of combustion to the heat required to raise the fuel temperature to the boiling point and then vaporize it. It was concluded that burning of liquid fuel on surfaces and in pans can be correlated by using the simple theory of Hottel [6] for individual fuel components. His explanations

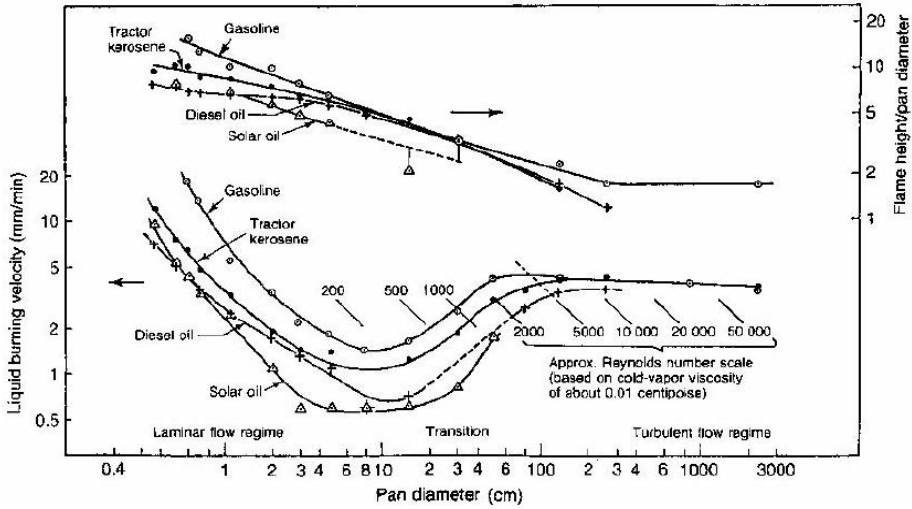


FIGURE 2.2: Burning rates and flame lengths of hydrocarbons [5, 7]

of how geometrical scales and different heat transfer modes affect fire behaviour lay the foundation for the two most important scientific concepts that have been developed for fire safety engineering during the last 30-40 years [6]. Early experiments with pools of liquid fuels showed that there are two basic burning regimes for pool fires: radiatively-dominated burning for pools with large diameters and convectively dominated burning for pools with small diameter. Nevertheless, diameters smaller than 0.2 m will always fall in the category of small pools. The burning rate per unit area (and hence most other characteristics) of a pool fire increases with tray diameter up to about 2-3 m, beyond which limit it becomes largely independent of diameter or may decrease slightly. This dependence is related to the burning regime which becomes increasingly dominated by radiation as soot levels rise up to a value where the fire is effectively optically thick. Several studies indicate a slight decrease in burning rate per unit area at very large pool diameters (~ 10 m), but there is not enough reliable data to accurately describe this for general cases [13]. To estimate the average mass loss rate, $\overline{\dot{m}}_f''$ (the " symbol indicates a value per unit area and the dot above the quantity indicates a rate) of a pool fire in the open air, the following equation may be used [13, 14]:

$$\overline{\dot{m}}_f'' = \overline{\dot{m}}_{\max}'' (1 - e^{-k\beta d}) \tag{2.1}$$

\overline{m}_{\max}'' is the mass loss rate per unit area for a very large pool, k is the extinction coefficient of the flame, β is the mean beam length corrector and d is the pool diameter. The average heat release rate (\overline{Q}_c) of a pool fire may be estimated from this if the heat of combustion ($-\Delta h_c$) of the fuel is known:

$$\overline{Q}_c = \overline{m}_f'' (-\Delta h_c) A_P \quad (2.2)$$

where $A_P = \frac{\pi}{4} d^2$ is the surface area of the pool. Tables of values of \overline{m}_{\max}'' , $k\beta$ and Δh_c for most common liquid fuels can be found in the literature [7, 13, 14]. It should be noted that the burning behaviour of alcohol pools is different from most other hydrocarbon fuels as the burning rate does not vary significantly with diameter, this is due to that fact that alcohols burn very cleanly, producing little soot and thus $\overline{m}_f'' \approx \overline{m}_{\max}''$. Fay [9] derives the equations for mass evaporation rate separately for adiabatic (there is negligible heat transfer between pool and substrate) and non-adiabatic (there is significant heat transfer from pool and substrate) pool fires.

Adiabatic pool fires

$$\overline{m}_f'' = (1 \times 10^{-3} \text{ kg/m}^2\text{s}) \times \frac{-\Delta h_c}{\Delta h_v} \quad (2.3)$$

Where $-\Delta h_c$ is the heat of combustion ≈ 45 MJ/kg for a typical hydrocarbon fuel. The evaporative heat transfer to the fuel surface is $\overline{m}_f'' \Delta h_v \approx 45$ kW/m². This heat of combustion utilised in raising the temperature of flame surface by means of convective (small pool diameters) and radiative heat transfer (large pool diameters) to the exposed objects.

Fay [9] considers convection as a major mode of heat transfer to the liquid rather than radiation as Hottel suggested. There are two reasons for this: 1. A hydrogen fire plume is not luminous enough to consider significant radiation transfer to the surface. 2. Also for large diameters, the surface emissive power *SEP* is inversely proportional to the diameter d so it is convective driven heat transfer (convective heat transfer coefficient $\propto \frac{1}{d}$).

On the basis of the above facts Fay derives convective heat flux (from flame to liquid

pool) for circular and rectangular pools as written below.

Circular pool:

$$\overline{\dot{m}}_f'' \Delta h_v = 1.30 \times 10^{-3} (1 \pm 0.19) \left(\rho_a \sqrt{gd} \left(\frac{-\Delta h_c}{1+f} \right) \right) \quad (2.4)$$

Rectangular pool:

$$\overline{\dot{m}}_f'' \Delta h_v = 1.75 \times 10^{-3} (1 \pm 0.34) \left(\rho_a \sqrt{gd} \left(\frac{-\Delta h_c}{1+f} \right) \right) \quad (2.5)$$

Non-adiabatic pool fires (Effect of the substrate)

It has been already observed experimentally that fuel pools on a substrate e.g. water always show an increased mass burning rate due to the external heat transfer from the substrate to the fuel. The total increased mass burning rate or mass evaporation [9] can be written more precisely as follows:

Total burning rate = Adiabatic mass burning rate + external mass burning rate due to enhanced evaporation due to heat transfer from the substrate

$$\overline{\dot{m}}_f''(t) = 1.30 \times 10^{-3} \left(\rho_a \sqrt{gd} \left(\frac{-\Delta h_c}{(1+f) \Delta h_v} \right) \right) + 1.10 \times 10^{-4} \left(\frac{\rho_1 V_1 c_p (T_a - T_1)}{\Delta h_v} \right) \quad (2.6)$$

where $\overline{\dot{m}}_f''(t)$ denotes the increase in mass burning rate as function of time due to spreading of fuel on water. Suffix 1 stands for the pool liquid properties. c_p is specific heat capacity of water. V_1 Fuel radial convective velocity (m/s). The variation of V_1 with time can be given as:

$$V_1(t) = \frac{dD(t)}{2dt} \quad (2.7)$$

Eq.(2.7) explains the variation of mass burning rate of a non-adiabatic pool fire which varies with the size of spilled pool and time.

The errors and uncertainties in the measurable quantities are a great concern for the reliable estimation of hazard from pool fires. The error in the measurement can be defined as the difference in the measured value and actual value whereas uncertainties are the spread in the data assigned in a justifiable manner [41]. Due to the several complexities in the measurements and uncontrolled field conditions in the large pool fire experiments, the errors and uncertainties are not extensively studied in the past. Therefore, only a qualitative estimation of uncertainties in different quantities are given

in the literature [13, 16]. Babraukas [13] gives a range uncertainty of $\pm 0.0018 \text{ kg}/(\text{m}^2 \text{ s})$ in the measurement of \bar{m}_{\max}'' ($0.2 \text{ m} \leq 20 \text{ m}$) for hydrocarbon fuels.

2.2.1.1 Theory of burning rate according to Hertzberg

Hertzberg [15] carries out the energy balance across the Gibbsian surface and derives the average burning rate equation. As shown in Fig. 2.3 any individual element of the surface area, of diameter dr , in the steady state coordinate frame at its individual fuel-feed rate $v_a(r, \theta)$. S_g in the gas and S_l in the liquid.

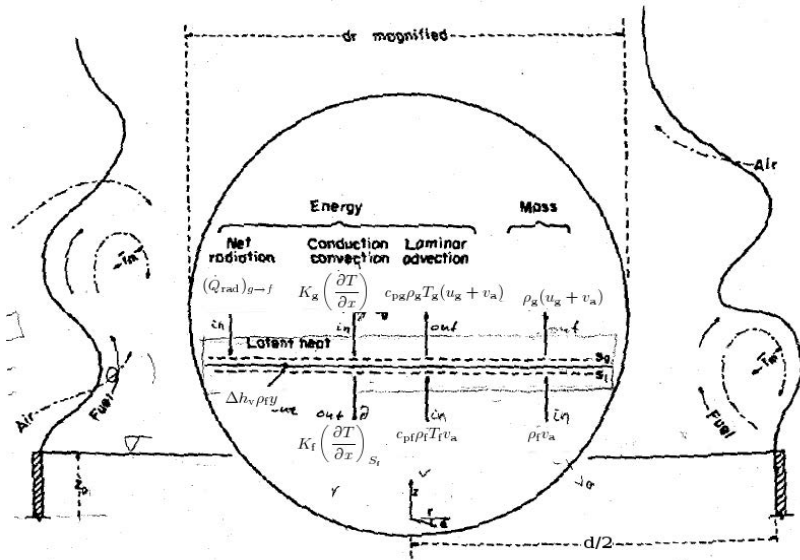


FIGURE 2.3: Energy and mass balance an element of surface area of a pool flame [12]

$$v_a(r, \theta) = \frac{K_g \left(\frac{\partial T}{\partial x} \right)_{S_g} - K_l \left(\frac{\partial T}{\partial x} \right)_{S_l} + (\dot{Q}_{\text{rad}})_{g \rightarrow f}}{\rho_l (c_{pv} - c_{pl}) T_s + \rho_l \Delta h_v} \quad (2.8)$$

The local burning rate of any surface element is directly proportional to the conductive, convective and radiative flux balance across the phase discontinuity. It is inversely proportional to the sum of the latent heat per unit volume of liquid plus the difference in thermal capacity across the phase boundary.

$$\bar{v}_a = \frac{1}{\pi r_0^2} \int_0^{2\pi} \int_0^{r_0} v_a r \, dr d\theta \quad (2.9)$$

An exact solution of eq. (2.9) would be obtained by averaging v_a over the entire pool surface.

2.2.1.2 Effect of lip height, thickness and pan material

The layer thickness of the pool has an effect if it is less than that required to reach steady state burning. Bounding materials (the material of the pan) also have great influence on burning rates due to conduction from the solid conductive pan material to the liquid pool but this is not valid for large diameters where the mode of heat transfer from flame to pool slowly changes from convection to radiation [7]. A significant lip height also leads to initiate turbulence closer to the pool edge and thereby raise convective heat transfer. It can also change the temperature distribution of the pan walls and hence change conduction terms in the total heat equation. It also tends to a larger, more emissive flame volume. The effect of cross wind on the flame characteristics is studied in much detail by many authors in the past [7, 9, 14, 16]. Some important findings are increased convective heat transfer and there on mixing which finally enhances the temperature of flame. It also decreases the radiative heat due to reduced flame volume and less well centred flame. A doubling of the burning rate of a hexane pool under a 4 m/s wind conditions was observed, with no further increase for greater velocities [4]. However, certain equations are given for different range of velocities and tilt angle of flame [13].

2.2.2 Flame length

The flame length is generally visible as the maximum length or time averaged visible length. The length trackable by the human eye is related to the area that emits light in the wavelength range of $380 \text{ nm} \leq \lambda \leq 750 \text{ nm}$. However, it is difficult to determine accurately the visible flame length because of temporal variation referred to as intermittency. A number of semi-empirical models have been developed by many researchers e.g. Thomas [16], Heskestad [14], McCaffrey [8], Moorhouse [7] and recently Fay [9]. The visible flames above a fire source contain the combustion reactions. Tamanini has

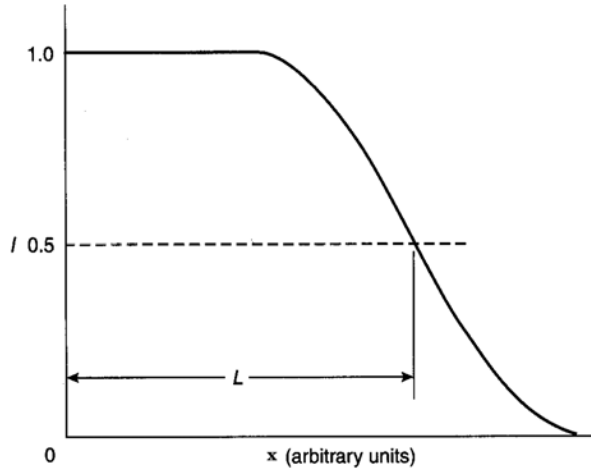


FIGURE 2.4: Definition of mean flame height by Zukoski [3]

investigated the manner in which combustion approaches completion with respect to height in diffusion flames. Typically, the luminosity of the lower part of the flame region appears fairly steady, while the upper part appears to be intermittent. In case of strongly sooting flame a variation in visible flame height can be caused by temporally variation in transmission properties of the soot cloud. Thus, reaction can be present but not visible. This effect seems to be typically ignored when determining flame lengths. Sometimes vortex structures, more or less pronounced, can be observed to form near the base of the flame and shed upward. Fig. 2.4 helps to define the flame height, \bar{H} . It shows schematically the variation of flame intermittency, I , versus distance above the fire source, x , where $I(x)$ is defined as the fraction of time that at least part of the flame lies above the elevation, x . The intermittency decreases from unity deep in the flame to smaller values in the intermittent flame region, eventually reaching zero. The mean flame height, \bar{H} , is the distance above the fire source where the intermittency has declined to 0.5. Measurements of the mean flame height according to the intermittency measurements are fairly consistent with (although tending to be slightly lower than) flame heights that are determined by the human eye. The mean flame length is an important quantity that marks the level where the combustion reactions are essentially completed and the inert plume can be considered to begin. Several expressions for mean flame height have been proposed. Fig. 2.5, taken from McCaffrey [8] shows normalised flame heights, $\frac{\bar{H}}{d}$ as a function of a dimensionless number, \dot{Q}^* (represented as $\dot{Q}^{*2/5}$),

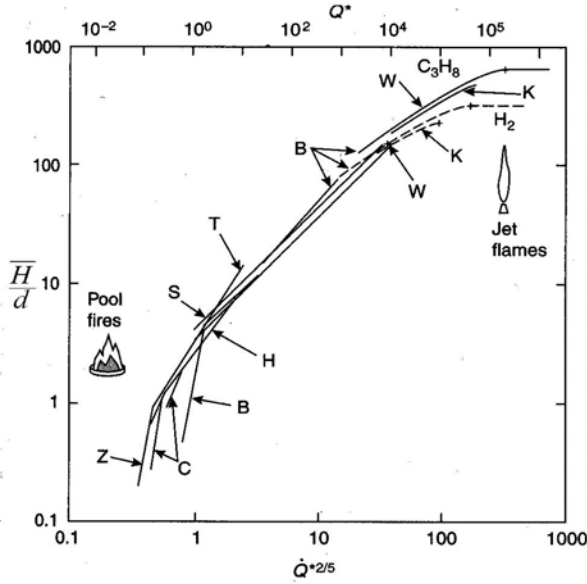


FIGURE 2.5: Flame length correlations for different hydrocarbon fuels compiled by McCaffrey [3]

from data correlations available in the literature. This dimensionless number \dot{Q}^* can be defined as

$$\dot{Q}^* = \frac{\bar{Q}_c}{\rho_a c_p T_a d^2 \sqrt{gd}} \tag{2.10}$$

where \bar{Q}_c is the total heat release rate (given in terms of the mass burning rate, \bar{m}_f as $\bar{m}_f(-\Delta h_c)$; ρ_a and T_a are ambient density and temperature respectively; c_p is the specific heat of air at constant pressure; g is the acceleration of gravity; d is the diameter of the fire source. Capital letters without subscripts in Fig. 2.5 correspond to various researchers as follows: B: Becker and Liang, C: Cox and Chitty, H: Heskestad, K: Kalghatgi, S: Steward, T: Thomas, W: Hawthorne et al., and Z: Zukoski. Capital letters with subscripts represent chemical formulae [3].

Quoting McCaffrey [3] with respect to Fig. 2.5: “On the left are pool-configured fires with flame heights of the same order of magnitude as the base dimension d . In the middle is the intermediate regime where all flames are similar and the $\dot{Q}^{*2/5}$ is seen as a 45° line in figure. Finally, in the upper right is the high Froude number, high-momentum jet flame regime where flame height ceases to vary with fuel flow rate and is several hundred times the size of the source diameter.”

2.2.2.1 Flame length model according to Thomas

Thomas [16] performed a range of experiments on wood crib fires and used the conservation of mass principle to formulate the height of the visible flame as a function of Froude number of the fuel Fr_f which is defined as follows

$$Fr_f = \frac{\overline{m}_f''}{\rho_a \sqrt{gd}} \quad (2.11)$$

According to Thomas [16] a general equation for flame length can be written as

$$\frac{\overline{H}}{d} = A \left(\frac{\overline{m}_f''}{\rho_a \sqrt{gd}} \right)^B \quad (2.12)$$

$$\frac{\overline{H}}{d} = A (Fr_f)^B \quad (2.13)$$

where A and B are constants that depend on the chemical properties of fuel being burnt. Thomas derived a value of A and B for wood crib fires as 42 and 0.61. Eq. (2.13) does not take into account the effects of cross wind. If the effect of cross wind is considered eq. (2.13) becomes

$$\frac{\overline{H}}{d} = 55 (Fr_f)^{0.67} (u^*)^{-0.21} \quad (2.14)$$

where u^* is the nondimensional wind velocity given by

$$u^* = \frac{u_w}{\left(\frac{g \overline{m}_f'' d}{\rho_v} \right)^{\frac{1}{3}}} \quad (2.15)$$

2.2.2.2 Flame length model according to Steward

By carrying out mass and momentum balance across the combustion zone Steward [17] derived an equation for the total visible length of a turbulent diffusion flame as follows:

$$\log_{10} \left(\frac{H}{y_0} \right) = 0.20 \log_{10} N + 1.21 \quad (2.16)$$

where N is the combustion number of fuel and defined as:

$$N = \frac{\bar{Q}_c^2 \left\{ r_{st} + \frac{\omega}{\rho_0} \right\}^2}{\rho_a^2 (-\Delta h_c)^2 g y_0^5 (1 - \omega)^5} \quad (2.17)$$

where

ω : Inverse volumetric expansion ratio due to combustion

ρ_0' : Dimensionless source density (lb/ft³)

r_{st} : Stoichiometric air to fuel ratio

ρ_a : Atmospheric density (lb/ft³)

y_0 : Source radius, respectively $\left(\frac{d}{2}\right)$ (ft)

The modified form of eq.(2.17) in SI units is given by Heskestad [18] and Fay [9] which are described in section 2.2.2.6.

2.2.2.3 Flame length model according to McCaffrey

McCaffrey [8] performed experiments on a 0.3 m x 0.3 m burner of natural gas. The flame was a fully developed turbulent buoyant diffusion flame. The centreline and radial flame temperature and the velocity were measured for a range of heat release rates of 10-50 kW. The data of measured temperature and velocity compiled for various heat release rates on one plot show a constant behaviour for three regimes if plotted against axial distance normalised by $\bar{Q}_c^{\frac{2}{5}}$. He divides the entire flame into three regimes based on x' which is a normalised axial distance above the fire source. The value of $x' \leq 0.08$ m kW^{-2/5} represents a continuous flame regime, $0.08 \leq x' \text{ (m kW}^{-2/5}) \leq 0.2$ is considered to be an intermittent regime and $x' \geq 0.2$ m kW^{-2/5} is the plume regime, based on heat release rate. Scaling is done in a way to allow comparison between different fuels at different heights. An assumption of x' is equal to 0.2 is done for predicting the visible flame length.

$$x' \approx \frac{x}{\bar{Q}_c^{\frac{2}{5}}} \approx 0.2 \text{ (m kW}^{-2/5}) \quad (2.18)$$

or the eq. 2.18 can be written as follows

$$\bar{H} \approx 0.2 \text{ (m kW}^{-2/5}) \bar{Q}_c^{\frac{2}{5}} \quad (2.19)$$

where \overline{H} is in m and \overline{Q}_c is the average heat release rate in kW.

2.2.2.4 Flame length model according to Moorhouse

Moorhouse [7] conducted several large scale tests of Liquefied Natural Gas pool fires. The crosswind and downwind motion picture data were analysed to determine the flame length. The correlation given by Moorhouse is as follows:

$$\frac{\overline{H}}{d} = 6.2 \left(\frac{\overline{m}_f''}{\rho_a \sqrt{gd}} \right)^{0.254} (u_{10}^*)^{-0.044} \quad (2.20)$$

where u_{10}^* is the nondimensional wind speed determined using eq. (2.15) with measured wind speeds at a height of 10 m.

2.2.2.5 Flame length model according to Heskestad

The correlation by Heskestad [18] represented in Fig. 2.5 covers the entire \dot{Q}^* range except the momentum regime (jet flames) and has the following form

$$\frac{\overline{H}}{d} = -1.02 + 15.6N^{\frac{1}{5}} \quad (2.21)$$

where N is the combustion number defined as

$$N = \left(\frac{c_p T_a}{g \rho_a^2 \left(\frac{-\Delta h_c}{r_{st}} \right)^3} \right)^{\frac{-2}{5}} \frac{\overline{Q}_c}{d^5} \quad (2.22)$$

The simplified form of eq. (2.21) can be written as

$$\frac{\overline{H}}{d} = -1.02 + A (\text{m kW}^{-2/5}) \frac{\overline{Q}_c^{2/5}}{d} \quad (2.23)$$

The coefficient, A ($\text{m kW}^{-2/5}$) varies over a rather narrow range, associated with the fact that $\frac{-\Delta h_c}{r_{st}}$, the heat released per unit mass of air entering the combustion reactions, does not vary appreciably among various fuels. For a large number of gaseous and liquid fuels, $\frac{-\Delta h_c}{r_{st}}$ remains within the range of 2900 kJ/kg, for which the associated range of

A under normal atmospheric conditions (293 K, 1 bar) is 0.240 to 0.226 (m kW^{-2/5}), with a typical value of $A = 0.235$ m kW^{-2/5}.

2.2.2.6 Flame length model according to Fay

Fay's model considers the pool fire phenomena as a combination of two zones, i.e. the combustion zone and the plume zone. This model also takes into account the grey-body thermal radiation (emission and absorption) by the soot particles both in the optically thick and the thin region. Following the basic conservation laws for both combustion and plume zone Fay derives a more precise relationship for \overline{H}/d . The sensible enthalpy flux E remains constant in the plume zone (as no fuel is available in the plume zone) but the mass and momentum flux, i.e. M and P continue to increase. By integrating the mass, momentum and enthalpy flux equations with suitable initial conditions and than substituting the ($x = \overline{H}_{cl}$) the full expression for length of clear flame or combustion zone can be written more precisely as follows

$$\frac{\overline{H}_{cl}}{d} = \left(\frac{9\pi^2}{32}\right)^{\frac{1}{3}} \left(\frac{1}{\phi_v^3 \eta_c \alpha_c^2}\right)^{\frac{1}{3}} \left(\frac{f_{st}^3 c_p T_a}{-\Delta h_c}\right)^{\frac{1}{3}} Fr_f^{\frac{2}{3}} \quad (2.24)$$

The ratio of the visible flame length to the diameter of pool is (Following the Steward criterion, i.e. visible length of the flame is a region where the equivalence ratio ϕ_v is 0.2)

$$\frac{\overline{H}}{d} = -\frac{x_0}{d} + \left(\frac{\pi^2 ((5)^4)^{\frac{1}{5}}}{4(3^5)}\right)^{\frac{1}{5}} \left(\frac{1}{\phi_v^3 \eta_p \alpha_p^2}\right)^{\frac{1}{5}} \left(\frac{f_{st}^3 c_p T_a}{-\Delta h_c}\right)^{\frac{1}{5}} Fr_f^{\frac{2}{5}} \quad (2.25)$$

where: M : Mass flux

P : Momentum flux

ϕ_v : Equivalence ratio

f_{st} : Mass ratio of products to fuel in a stoichiometric mixture

η : Dimensionless form factor

α : Mass ratio of product to fuel in a stoichiometric mixture

c_p : Specific heat capacity (kJ/(kg K))

T_a : Ambient temperature (K)

$-\Delta h_c$: Specific enthalpy of combustion (kJ/kg)

Fr_f : Fuel Froude number

g : Gravitational acceleration (m/s²)

x_0 : Distance below the pool surface where M and P are zero

Subscripts c and p stand for combustion and plume zone, respectively.

Fay also provides a simplified form of eq. (2.17) given by Steward as

$$N \equiv \frac{\pi}{4} \left(\frac{f_{st}^3 c_p T_a}{-\Delta h_c} \right) Fr_f^2 \quad (2.26)$$

A wide range of LNG pool fire data (effective diameters $d = 1.8$ m to 35 m, wind speed $u_w = 1.8$ to 14.4 m/s, flame lengths $\bar{H} = 3.3$ to 77 m, and flame tilt $\theta = 28^\circ$ to 66°) was compared by Fay and the simplified forms of eq. (2.24) and (2.25) have been developed.

Combustion zone:

$$\frac{\bar{H}_{cl}}{d} = (13.8 \pm 2.15) Fr_f^{\frac{2}{3}} \quad (2.27)$$

Visible length:

$$\frac{\bar{H}}{d} = 15.5 (1 \pm 0.095) Fr_f^{\frac{2}{5}} \quad (2.28)$$

All semi-empirical models available to date may be utilised for fuels for which they have been specifically developed. Hydrocarbon fuels seem to follow them relatively well. The accuracy of measurements is sometimes also questionable under different atmospheric conditions. The equations in their full form (including chemistry and turbulence) may appear different for different fuels specifically when the chemistry of fuel is considered. Nevertheless, they are still useful for a first approximation of the visible flame length.

Flame tilt The effect of cross wind on flame characteristics is studied in much detail by many authors in the past [3, 4, 7, 9, 14]. Some important findings are an increase in convective heat transfer and thereon mixing which finally enhances the temperature of the flame. It also decreases the radiative heat due to the small flame volume and the less well centred flame. Lois and Swithenbach [4] observe a doubling of the burning rate of a hexane pool in a 4 m/s wind, with no further increase for greater velocities. However, certain equations were given for different ranges of wind velocities and flame tilt angle [13]. Fays model for predicting flame tilt under the influence of cross wind is

$$\sin\theta = \frac{Fr_w}{Fr_w + 0.19} \quad (2.29)$$

where Fr_w is wind Froude number defined as $\frac{u_w}{\sqrt{gd}}$
 u_w = Velocity of wind in m/s
 θ = Angle of tilt in degree

2.2.2.7 Effect of unsteadiness

The measure of cyclic unsteadiness is the Strouhal number which is defined as the product of the length scale times the frequency divided by the velocity scale. In pool fires the length scale is d and the velocity is \sqrt{gd} . Thus, the Strouhal number is given by

$$Sr = f \sqrt{\frac{d}{g}} \quad . \quad (2.30)$$

The typical Strouhal number for jet flames is proportional to \sqrt{d} and is 0.48 [18]. Large pool fires also show distinct features due to turbulence which mainly governs the fire by fluctuations (the frequency of pulsation varies inverse root of diameter of pool, i.e. $f \propto \frac{1}{\sqrt{d}}$)[19].

2.2.3 Flame temperature and flow velocity

McCaffrey [8] carried out extensive measurements of temperature, velocity along the centreline of fully developed buoyant diffusion flame in a 0.3 m × 0.3 m natural gas porous burner [14]. In Fig. 2.6 and 2.7 the measurement of temperature difference between flame and ambient i.e. ΔT , measured with the thermocouples and velocity of gases (measured with the pressure probes) normalised by $\bar{Q}_c^{\frac{1}{5}}$ for four different heat release rates is shown against the normalised distance x' (see eq. (2.18)).

As can be seen the data of ΔT and $u/\bar{Q}_c^{\frac{1}{5}}$ show the similar trend for a specific region of x' irrespective of the heat release rates. So the entire fire can be divided into three regimes based on x' . The value of $x' \leq 0.08$ represents the continuous flame regime, $0.08 \leq x' \leq 0.2$ is considered to be the intermittent regime and $x' \geq 0.2$ is the plume regime, based on heat release rate. Scaling is done in a way to allow comparison between different fuels at different heights (Figs. 2.6 and 2.7). This scaling helped to classify the three different regimes in a large pool fire quantitatively as shown in Fig. 2.1.

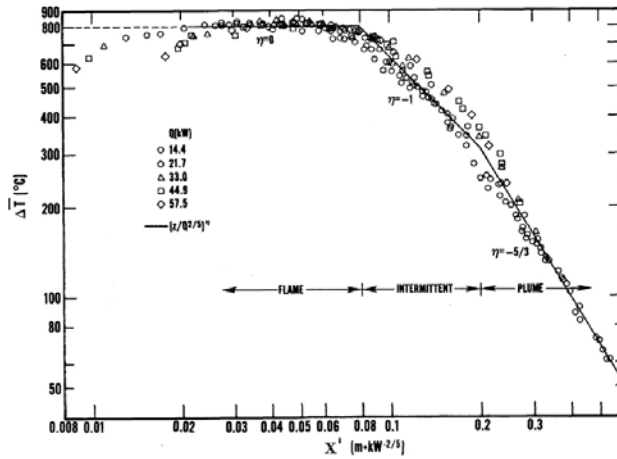


FIGURE 2.6: Centreline average temperature for different heat release rates [14]

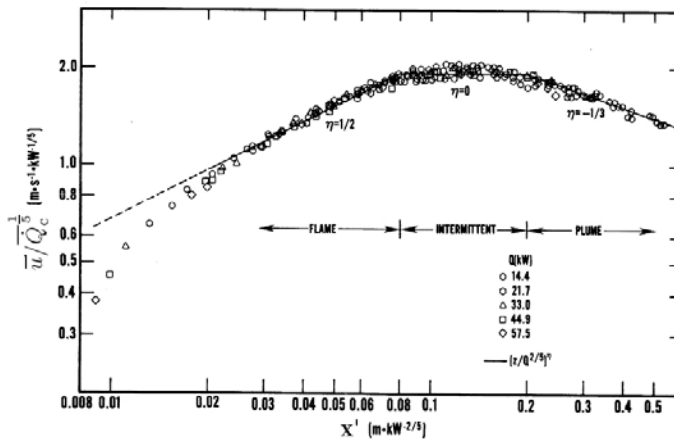


FIGURE 2.7: Centreline average velocity for different heat release rates [14]

A number of measurements were made to define the thermal and flow conditions in a 9 m x 18 m JP-4 pool fire by Schneider et al. [20] to simulate a transportation accident. Temperatures were measured (with thermocouples, $\pm 8^\circ\text{C}$) at twenty-eight locations throughout the continuous flame region. Velocities were measured (with bi-directional pressure probes, ± 7 m/s) at four vertical positions near the centreline of the pool. The measurements of gas velocity made in the lower continuous flame region (Fig. 2.8) in this study agree well with the data available from smaller fires. Velocity measurements (Fig. 2.9) at higher positions than those addressed here (in the upper continuous flame and the intermittent flame region) in fires of this size have not been published to date. These measurements should be attempted in future to study if the agreement with small fires continues in this region.

Temperatures measured in this study have been compared with the results of others. Comparisons are difficult because of the lack of information in many cases about the existing winds, and the known strong wind effects. In spite of these difficulties, a scheme has been attempted which mitigates, to some degree, the effects of mild wind conditions. The average temperatures conditioned for times of low wind have been compared with results of other workers taken during times of "quasi-steady" burning and reasonable agreement was found at low stations ($x' \sim 0.02 \text{ m kW}^{-2/5}$) [20].

In the plume zone mass and momentum flux continue to increase but the mass flow average value of temperature \bar{T} and velocity \bar{u} decline according to the relation below:

$$\frac{\bar{T}}{T_a} - 1 = \left(\frac{\pi^2 (5)^4}{4(3^5)} \right)^{\frac{1}{3}} \left(\frac{-\Delta h_c}{\sqrt{\eta_p} \alpha_p c_p T_a} \right)^{\frac{2}{3}} (Fr_f)^{\frac{2}{3}} \left(\frac{x+x_0}{d} \right)^{-\frac{5}{3}} \quad (2.31)$$

$$\frac{\bar{u}}{\sqrt{gd}} = \left(\frac{25\pi}{48} \right)^{\frac{1}{3}} \left(\frac{\eta_p (-\Delta h_c)}{\alpha_p^2 c_p T_a} \right)^{\frac{1}{3}} (Fr_f)^{\frac{1}{3}} \left(\frac{x+x_0}{d} \right)^{-\frac{1}{3}} \quad (2.32)$$

Eq. (2.31) and (2.32) are the results of mass, momentum and energy balance across the combustion and plume regime of a large pool fire [9]. The notations have been already defined in section 2.2.2.6. The important facts both equations carry along are the temperature and velocity both tend to decrease along the length of the flame with a power of $\frac{5}{3}$ and $\frac{1}{3}$ respectively.

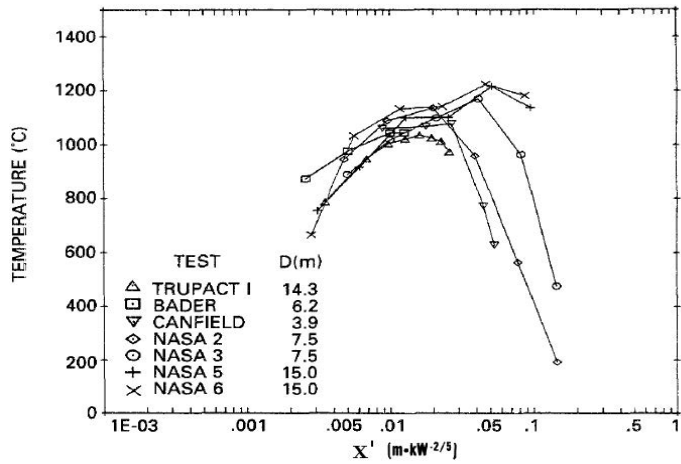


FIGURE 2.8: Centreline measured average temperature for different heat release rates [20]

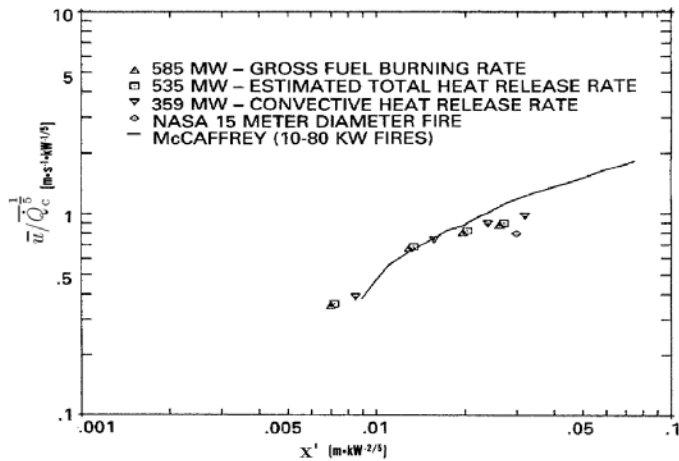


FIGURE 2.9: Centreline average velocity for different heat release rates [20]

2.2.4 Adiabatic flame temperature

For a closed, adiabatic system ($\delta Q = 0$), the first law of thermodynamics yields the total enthalpy $dh=0$. Furthermore, the overall mass is constant.

Therefore, the enthalpy of reactants (denoted as index r) and products (denoted as index p) have the same specific enthalpy.

$$\sum_i w_{ri} \Delta h_{ri}(T_a) + (-\Delta h_{ci}) = \sum_j w_{pj} c_{pj}(T_{ad} - T_a) \quad (2.33)$$

here, w_{ri} is the mass fraction of reactant i before combustion, Δh_{ri} is the enthalpy of each reactant at ambient temperature, $(-\Delta h_{ci})$ is the heat of combustion, in J/kg, w_{pj} is the mass fraction of products j with average heat capacity c_{pj} and the reference temperature is taken as ambient, T_a . By using eq. (2.33) T_{ad} of the stoichiometric TBPB and TBPEH pool flames can be determined [3, 14, 62]

2.2.5 Thermal radiation

One of the main reason for determining safety criteria is due to the damage caused by fires due to heat radiation [7].

2.2.5.1 Point source model

The point source thermal radiation model is based on the following assumptions: (1) the flame can be represented as a small source (point) of thermal energy; (2) the energy radiated from the flame is a specified fraction of energy released during combustion; and (3) the thermal radiation intensity varies proportionally with the inverse square of the distance from the source.

Expressed mathematically, the average irradiance \bar{E} at any distance from the source is given by the following equations:

$$\bar{E} = \frac{\bar{Q}_{rad}}{4\pi\Delta y^2} \quad (2.34)$$

and

$$\bar{Q}_{rad} = f_{rad} \bar{m}_f'' (-\Delta h_c) A_P \quad (2.35)$$

Here, $\overline{Q}_{\text{rad}}$: Average total energy radiated per unit time (W)

\overline{m}_f'' : Fuel mass burning rate ($\text{kg}/(\text{m}^2 \text{ s})$)

f_{rad} : Fraction of combustion energy radiated

Δy : Distance from source to the receiver (m)

While the above model is elegant because of its simplicity, two important limitations should be recognised. The first involves the modelling of radiative output and the second is the description of the intensity as a function of distance from the source.

The most important parameter in the point source model is the fraction of combustion energy radiated to the surrounding. This fraction f_{rad} can be estimated by several expressions e.g. OSRAMO [11] and by using measured radiometer data. There is extensive laboratory data which suggest that the radiation from buoyant diffusion flames remains proportional to the overall heat release rate provided the flame is fully turbulent and the flame geometry is properly scaled. It was shown in [7] that the radiative power linearly varies as a function of heat release rate for a propane diffusion flame. Similar laboratory data is available for gaseous ethane, methane, ethylene, butane and propylene diffusion flames, gasoline, hexane, benzene and liquefied natural gas, methanol, unsymmetrical dimethylhydrazine and hydrogen pool fires.

It is suggested that the radiative fraction for geometrically similar buoyant turbulent diffusion flames is constant due to an essentially invariant Kolmogorov microscale. This assumes that the flames are both optically thin and chemically similar and hence the radiative fraction is determined by the thermochemical properties of the fuel. Both these assumptions break down as one goes from a “moderate scale” laboratory experiment to a “large scale” field experiment as the atmospheric conditions i.e. cross wind affects the radiation upto a great extent. At present, however, there is insufficient composition data on larger fires to clearly delineate the dependence between moderate and large scale fires. The equated point source and a uniformly radiated cylindrical source model concluded that the fraction of combustion energy radiated may be expressed as follows [7]:

$$f_{\text{rad}} = \frac{\overline{SEP}}{\overline{m}_{\text{max}}''(-\Delta h_c)} \left(1 + 4\frac{\overline{H}}{d}\right) \quad (2.36)$$

Here \overline{SEP} is the average surface emissive power of the flame in kW/m^2 . Since the flame height is influenced by the flame diameter (with larger diameter flames have shorter

flame heights), it is concluded in [7] that the fraction of energy released by radiation should decrease for larger fires. However, in large scale hydrocarbon pool fires, smoke obscuration contributes to a reduction in measured flame emissive powers. Therefore, the effect of flame geometry on the radiative fraction may be of second order.

The second limitation to be observed in a point source model is that the model overestimates the intensity of thermal radiation at observer locations close to the fire. This is primarily because the near field radiation is greatly influenced by the flame size, shape, tilt and the relative orientation of the observer. The model, however, predicts far field thermal radiation intensities with reasonable accuracy.

In summary, a point source model provides a simple and elegant means of estimating thermal radiation intensity in the farfield where the effects of flame geometry are not significant. This can be used to determine thermal radiation hazards to personnel, where normally a conservative estimate of hazard is acceptable. Caution must be exercised in using the model to determine siting criteria, such as spacing between two storage tanks as the engulfment of multiple storage tanks in fire may produce a very different scenario of radiation hazard than that in case of single tank.

2.2.5.2 Conventional and modified solid flame radiation model

A more useful approach generally used in the literature to evaluate the thermal radiation field around a fire is based on recognising the fact that the radiation originates from the hot products of combustion. This approach is based on the fact that the entire volume of the flame emits thermal radiation in the luminous spectral range and partly in the less intensive non luminous infrared range. The rate of thermal radiation is significant only from the infrared spectral region. The measurements have confirmed that the irradiance of the burnt gas (non-luminous) plume above a fire accounts for less than 10% of the mean irradiance of the visible fire [7].

A simplified version of this model is called the "solid flame radiation model" and it is widely used for describing thermal radiation from large hydrocarbon fires. The solid flame model assumes the flame to be a cylinder with diameter equal to the base diameter of the fire and axial length equal to the length of visible fire plume. The flame is assumed to radiate isotropically in horizontal direction and inhomogeneously in axial direction.

The determination of the average surface emissive power \overline{SEP} of a flame is more difficult. The thermal radiation from a fire emanates from both gaseous species such as water vapour, carbon dioxide and carbon monoxide as well as from luminous soot particles. The gaseous species emit radiation in certain spectral bands whereas the soot radiation is continuous over the entire spectral range of flame. The theories of gas radiation and the models developed to describe the band emission from various gases are described in most text books on radiative heat transfer. Some simplified calculation procedures have been developed for obtaining the gas emissivities. A model proposed in [7] which considers fire as a two-species emitter whose total radiance is equal to the weighted sum of the radiation due to gas emissions and that due to luminous soot.

The surface emissive power (SEP) of a pool fire is given in the conventional solid flame radiation model:

$$\overline{SEP} = \overline{SEP}_b \bar{\epsilon}_F \quad (2.37)$$

Here,

\overline{SEP}_b : Black body average surface emissive power (kW/m²)

$\bar{\epsilon}_F$: Flame emissivity

with the surface emission temperature T_F of the fire is known (which is significantly less than the adiabatic flame temperature) the black body emissive power is given by:

$$\overline{SEP}_b = \sigma \left(\bar{T}_F^4 - T_a^4 \right) \quad (2.38)$$

where

\bar{T}_F : Average surface emission temperature of the flame (K)

T_a : Ambient temperature (K), and

σ : Stefan-Boltzman constant (kW/(m²K⁴))

In the conventional solid flame model $\bar{\epsilon}_F = 0.95$ (valid for optical thick flames) is assumed.

The emissivity accounts for the fact that the flame is a grey emitter, i.e. not an ideal black body radiator. Calculation of combined emissivity of the burnt gases (soot, water vapour and carbon dioxide) is extremely difficult even when the concentrations are uniform and the temperature is constant. The emissivity also depends on the path length through the fire. The combined emissivity is given by:

$$\epsilon = \epsilon_s + \epsilon_c + \epsilon_w - \Delta\epsilon_{c,w} \quad (2.39)$$

where,

ε_s : Spectrally averaged emissivity of soot,

$\varepsilon_c, \varepsilon_w$: Molecular band integrated emissivity of CO₂ and H₂O and,

$\Delta\varepsilon_{c,w}$: Correction factor for the CO₂-H₂O band overlap

It was shown that the soot emissivity can be determined by the following expression[7]:

$$\varepsilon_s = 1 - \frac{15}{\pi^4} \psi^3 \left\{ 1 + \frac{7}{C_2} T_F C L \right\} \quad (2.40)$$

Here,

C : Effective soot concentration parameter,

L : Path length (m)

C_2 : Planck's second constant, and

$\psi^{(3)}$: Penta gamma function

Many experimental data on soot emission from luminous flames of gaseous, polymer and wood fuels were reviewed and it was demonstrated that eq. (2.41) can be approximated by the following expression for a grey emitter:

$$\varepsilon_s = 1 - e^{-k_s L} \quad (2.41)$$

where

$$k_s = 3.6 \frac{C T_F}{C_2} \quad (2.42)$$

is the effective soot emission parameter.

There has been considerable discussion on whether luminous flames can be regarded as being spectrally gray. In general, the emissivity of a homogeneous mixture of path length x can be given by:

$$\varepsilon_m(x) = \frac{1}{\sigma T_F^4} \int_0^\infty SEP_b(\lambda) (1 - \exp(-k_{m\lambda} x)) d\lambda \quad (2.43)$$

If the mixture is spectrally gray, $k_m = k_{m\lambda}$ and the integral becomes

$$\varepsilon_m(x) = \varepsilon = 1 - \exp(-k_m x) \quad (2.44)$$

where k_m : Extinction coefficient (m⁻¹)

From a theoretical point of view, the assumption of a homogeneous gray mixture permits the calculation of radiative heat transfer in terms of the characteristics flame shape and the single dimensionless optical depth parameter $k_{m,x}$, where x is some characteristic length for a particular geometry. This assumption simplifies such calculations.

For large fires, the numerical value of flame emissivity approaches unity. Therefore, the *SEP* can be determined using the surface emission temperature T_F . However, the T_F for many liquid fuels are not available. In fact, measurements of radiative flux using narrow angle radiometers are often used to predict the *SEP* and the irradiances E for some liquid hydrocarbon fuels.

Most hydrocarbon fuel fires become optically thick when the diameter is about 3 m or larger. Under these conditions, the SEP_{max} that has been determined for gasoline fires is in the range of 110 to 130 kW/m². It was reported that the *SEP* of 130 kW/m² for 1.5 diameter fires and 20 kW/m² for 10 m diameter fires. The measured irradiance E appears to decrease for larger fires, indicating that the *SEP* is decreasing with increasing d [7].

It has been observed in large liquid hydrocarbon fuel fires with a carbon to hydrogen ratio greater than about 0.3, that a substantial part of the fire is obscured by a thick black smoke on the outer periphery. This smoke layer absorbs a significant part of the radiation and results in a very smaller irradiance to the surroundings. However, occasionally the smoke layer opens up exposing the hot flame and pulse of intensive radiation is emitted to the surroundings.

Although the thermal radiation from black relatively cold smoke is low, the hot spots appearing on the flame surface due to turbulent mixing have a higher *SEP*. Large eddies within the flame bring fuel to the outer edges of the fire plume and a more efficient combustion takes place on the flame surface. Based on a qualitative observation of the movie records of kerosene fires on land and gasoline fires on water, it appears that the luminous zones cover approximately 20% of the flame surface area, on a time averaged basis. These luminous spots have an emissive power of about 110-130 kW/m². However, it is not possible to calculate the radiation field surrounding a fire with intermittent luminous spots. It has been also observed that the emissive power of the black smoke is about 20 kW/m² and the temperature is about 800 K.

From a hazard prediction point of view, one can combine the thermal radiation from the black smoke with the radiation from luminous spots on an equivalent area basis to arrive at an \overline{SEP} for the fire. For example, if we assume that 80% of the surface area

is covered with black smoke and 20% with luminous spots, the \overline{SEP} is given by the following expression:

$$\overline{SEP} = 0.2[130] \text{ kW/m}^2 + 0.8[20] \text{ kW/m}^2 = 42 \text{ kW/m}^2 \quad (2.45)$$

Such an estimate is consistent with the wide angle radiometer measurements of JP-4, JP-5 and gasoline fires [7].

2.2.5.3 View factors

The view factor between a fire and a receiver element outside of the fire depends on the flame shape, the relative distance between the fire and the area of the receiving element, and the relative orientation of the element. In general, the view factor is defined by the following equation:

$$\varphi_{F,R} = \frac{1}{\pi \Delta A_R} \int_{A_F} \int_{A_R} \frac{\cos \beta_F \cos \beta_R}{\Delta y^2} dA_F dA_R \quad (2.46)$$

Here, β_F and β_R are respectively the angles made by the normals and dA_F on the fire and dA_R on the receiving element; where Δy is the distance between the fire element and the receiving element. The integration is carried out over the entire surface of the flame. In the point source model, the radiant intensity at any location is calculated

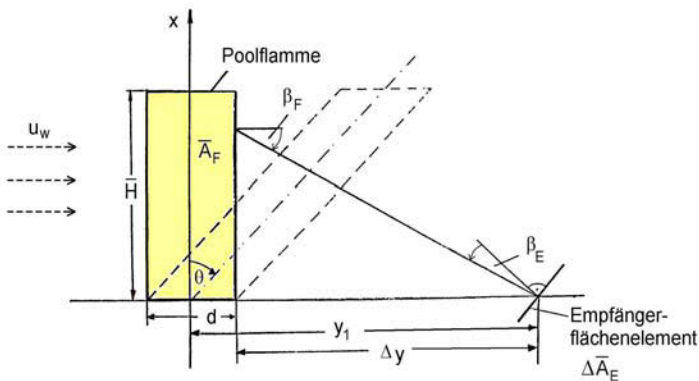


FIGURE 2.10: View factor between flame and receiver

using inverse square law. The finite size of the source can be taken into account by

determining the radius of an equivalent sphere or a hemisphere located at ground level. The view factor is given by the following equation:

$$\varphi_p \sim \frac{\left(\frac{d}{2}\right)^2}{\Delta y^2} \quad (2.47)$$

where $\frac{d}{2}$ is the radius of the source and Δy is the distance from the centre of the fire to observer location. As pointed out earlier, point source models are applicable at large distances from the fire.

In the solid flame model, the turbulent flame is approximated by a cylinder. Under wind free conditions, the cylinder is vertical. Under the influence of wind, the cylinder is assumed to be tilted. These two configurations of the solid flame model are shown in [7, 11]. The horizontal and vertical view factors (Fig. 2.10) for a vertical cylinder are as follows:

$$b = \frac{y_1}{(d/2)} = 1 + \frac{\Delta y}{(d/2)}$$

$$a = \frac{\bar{H}}{(d/2)}$$

$$A = (b + 1)^2 + a^2$$

$$B = (b - 1)^2 + a^2$$

$$\varphi_{R,F,h} = \frac{1}{\pi} \left(\tan^{-1} \sqrt{\frac{b+1}{b-1}} - \left(\frac{b^2 - 1 + a^2}{\sqrt{AB}} \right) \tan^{-1} \sqrt{\frac{(b-1)A}{(b+1)B}} \right) \quad (2.48)$$

$$\varphi_{R,F,v} = \frac{1}{\pi} \left(\frac{1}{b} \tan^{-1} \frac{a}{\sqrt{b^2 - 1}} + \frac{a(A - 2b)}{b\sqrt{AB}} \tan^{-1} \sqrt{\frac{(b-1)A}{(b+1)B}} - \frac{a}{b} \tan^{-1} \sqrt{\frac{(b-1)}{(b+1)}} \right) \quad (2.49)$$

The maximum view factor is the vectorial sum of horizontal and vertical view factors and is as follows:

$$\varphi_{F,R,max} = \sqrt{\varphi_{F,R,h}^2 + \varphi_{F,R,v}^2} \quad (2.50)$$

2.2.5.4 Atmospheric absorption

The radiation from the fire to surrounding objects will be partially attenuated by absorption and scattering along the path. The main species of the atmosphere that absorb thermal radiation are water vapour (H_2O) and carbon dioxide (CO_2).

The absorption by the water vapour and carbon dioxide in a certain length of the atmosphere of black body radiation from a source can also be calculated using the emissivity charts published by Hottel and Sarofim [7].

2.2.6 Organised Structures Radiation Models (OSRAMO II, OSRAMO III)

The Organised Structure Radiation Models (OSRAMO)[11, 94] take into account the specific SEP of hot spots (hs) and soot parcels (sp). It is assumed that the hot spots, soot parcels, effective reaction zone (re) and the fuel bales (fp) have homogeneous entity characterised by the lengths l_i ($i = \text{hs, sp, re, fp}$). These organised (dissipative) structures i can partially emit, absorb and transmit thermal radiation. It is further assumed that these structures i have different, but constant medium temperatures and effective absorption coefficient. It is also assumed that hot spots and soot parcels with flame diameter-dependent surface area ratios occur on the flames surface. In the models OSRAMO II, III this is the first time the highly complex three-dimensional thermal radiation phenomenon adequately taken into account.

The heat radiation model OSRAMO II regards the different thermal radiation of the coherent structures hot spot and soot parcel and their mean area fractions on the flame surface, depending on the fuel and the pool diameter. With this model it is possible to give a realistic description of the thermal radiation of large scale pool fires [11, 21, 85]. The thermal radiation from the reactive zones is by the hot spots and soot parcels absorbed and then partially re-emitted. The average specific SEP of the entire surface according to OSRAMO II consists of the SEP of the structural elements: Soot parcels and hot spots and can be written as

$$\overline{SEP}_{\text{OS}}^{\text{II}}(d) = \overline{SEP}_{\text{hs}} \bar{a}_{\text{hs}}(d) + \overline{SEP}_{\text{sp}} \bar{a}_{\text{sp}}(d) \quad (2.51)$$

where a stands for the area fractions of hot spot (hs) and soot parcels (sp).

In the stochastic radiation model OSRAMO III [85] from the empirically determined log-normal probability density functions for JP-4 pool fire and relating large, sooty, hydrocarbon pool fires, considering the temperatures and temperature ranges, as well as the areas of hot spots and soot parcels, the mean surface emissive power $\overline{SEP}_{\text{act}}^{\text{III}}(d, f)$ is calculated by:

$$\overline{SEP}_{\text{act}}^{\text{III}}(d, f) = \int_{\overline{SEP}} g_{\text{SEP}}(\overline{SEP}, d, f) \overline{SEP} \, d\overline{SEP}, \quad \text{for } d \geq 1 \text{ m} \quad (2.52)$$

With OSRAMO III the pdf of temperature (g_{T}) and SEP (g_{SEP}) regions of hot spots and soot parcels can be determined by using the probability density function of \overline{T} and \overline{SEP} [11, 21, 85].

2.3 Organic peroxides

Organic peroxides are extensively used as initiators of free-radical polymerisation in polymer production. Organic peroxides can have a variety of characteristics depending on their chemical structure and reactivity. The reactivity of the peroxides depends on the peroxide group configuration and on the type of substituents. Organic peroxides can be classified into different groups depending on their chemical structures (see Table 2.1) [24]. Organic peroxides combine a number of interesting features for the application in organic synthesis:

- High purity
- Good solubility in most organic systems, enabling homogeneous reaction conditions
- Well defined and temperature controlled reactivity
- High efficiency in radical formation
- Relatively low cost/performance ratio

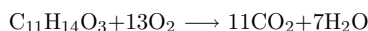
Peroxides are unstable compounds and therefore knowledge about their safe handling is of great interest [25, 26, 28, 29, 30]. A wide range of publications on several safety parameters determination based on thermal stability, the fast decomposition, mechanical sensitivity, flammability, sensitivity to contamination and also their physiological effects have been reported and outlined in the United Nations recommendations on the transport of dangerous goods under Class 5. In general, organic peroxides are not explosive

but their decomposition may lead to explosion, particularly if confined [26]. The safety distance calculations and assignment of an organic peroxide in a particular storage group is determined by their intensity of burning [26, 29].

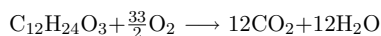
A number of large fire tests were carried out during the last decades in different organisations to develop uniform guidelines for such safety measures [7, 27]. Most of such tests reported in the literature are for packaged materials either solid or liquid. One such large scale test for two organic peroxides [tert-Butyl peroxybenzoate (TBPB) and tert-Butyl peroxy-2-ethylhexanoate (TBPEH)] was carried out in the Federal Institute for Materials Research and Testing (BAM) during 1979.

The chemical structures of some organic peroxides: DTBP (Dialkylperoxide), TBPB (peroxyester), TBPEH (peroxycarbonates), TBHP (Dialkylperoxide) and INP (Diisnonanoylperoxide) are shown in Fig. 2.11. An experimental and numerical approximation of this test in a form of a pool fire has been also carried out in this work. The stoichiometric combustion and the physical and chemical properties of TBPB and TBPEH are listed in Table 2.2 [29, 30, 31].

TBPB



TBPEH

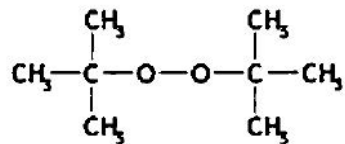


The temperature dependence of single step chemistry for combustion is modelled by an Arrhenius relationship (used to calculate source or sink term in the energy and species conservation equation) which states:

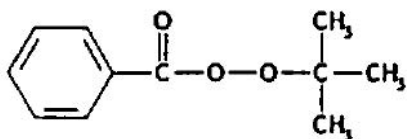
$$k = AT^\beta \exp\left(\frac{-E_A}{RT}\right) \quad (2.53)$$

Where k is the reaction rate constant; A is pre exponential factor; E_A is activation energy; β is reaction dependent parameter.

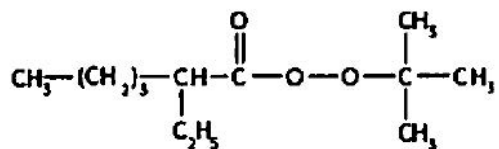
DTBP



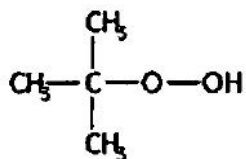
TBPB



TBPEH



TBHP



INP

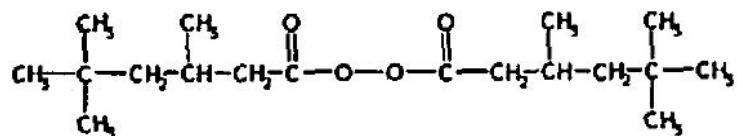


FIGURE 2.11: Chemical structures of DTBP, TBPB, TBPEH, TBHP and INP [31]

Parameter	TBPB	TBPEH
Molar mass (g/mol)	194.23	216.32
Activation energy (stoichiometric combustion) (kJ/mol)	151.59	124.90
Pre-exponential factor (1/s) (stoichiometric combustion)	2.23×10^{16}	1.54×10^{14}
Reaction dependent coefficient β	0	0
Specific enthalpy of formation (kJ/kg)	-1377	-1158
Heat of combustion (kJ/kg)	30113	34455
Refractive index	1.499	1.428
Dynamic viscosity (mPa s)	8	4
Density (kg/m ³)	1037	900

Table: 2.2: Properties of TBPB and TBPEH

2.3.1 Self Accelerating Decomposition Temperature of organic peroxides

The capability of organic peroxides to decompose may initiate violent chemical reactions leading to explosions. Therefore, the Self-Accelerating Decomposition Temperature (SADT) is an important characteristics to be defined for organic peroxides. The SADT is defined as the lowest temperature at which self accelerating decomposition may occur with a substance in the packaging as used in transport. The SADT is a measure of the combined effect of the ambient temperature, decomposition kinetics, package size and the heat transfer properties of the substance and its packaging [26]. The extrapolated onset temperature is defined as the point of intersection of the tangent drawn (on a heat flow versus temperature diagram) at the point of greatest slope on the leading edge of the peak with the extrapolated base line [95]. Malow and Wehrstedt [29] describe the use of Differential Scanning Calorimetry (DSC) for the measurement of SADT of different organic peroxides.

2.3.2 Fire and explosion hazards of organic peroxides

The organic peroxides contain a large amount of oxygen which directly supports the combustion and explosion processes, even though air is excluded. The unusual burning characteristics of Benzoyl peroxide have been demonstrated in tests which show that it

ignites under about one-fifth the amount of the heat required to ignite black powder, and that it burns with great rapidity [25].

Organic peroxide fires have much higher burning rates and will burn faster than usual flammable liquids or combustible solids. For instance, automatic sprinklers will not usually operate in time to extinguish a fire when some of the more reactive organic peroxides have started to burn. They will, however, serve to cool adjacent containers and prevent other combustibles from burning. Ditertiary butyl peroxide burns at a rate ten times that of an equal quantity of methanol in small test quantities [25]. As the burning of most organic peroxides is a rapidly accelerating phenomenon, small scale tests are not always a satisfactory indication of high mass burning rate of large quantities of these peroxides.

In general, liquid organic peroxides, combined with diluents in the form of a paste or liquid, burn at a slower rate than the concentrated peroxide and it is usually less sensitive to thermal shock or impact. The choice of the diluent is important in determining the hazard of such materials. The fire hazard is reduced only during the time when both the organic peroxide and diluent burn off simultaneously. It has been demonstrated that diluents which burn either more or less rapidly than the organic peroxide permit some of the hazardous chemical to be consumed alone and with great rapidity, sometimes approaching explosion. The more desirable mixtures of organic peroxides and solvents are likely to produce a type of burning in which the whole mass is burnt more slowly and can be easily extinguished. The use of volatile solvents which may entrain or creep up the sides of a container and evaporate should be avoided. This can result in the deposition of very sensitive concentrated peroxides.

Some of the organic peroxides will decompose slowly when exposed to a slow and gradual increase in temperature. On the other hand, these materials can decompose violently or even explode when subjected to a rapid and excessive increase in temperature. This behaviour is termed "thermal shock". Benzoyl peroxide is typical of this, as it is sufficiently unstable to be exploded by rapid heating in a confined space [25].

2.4 Modelling and simulation of pool fires

Pool fire modelling presents number of significant challenges to researchers due to simultaneous occurrence of complex physical phenomena e.g. turbulence and combustion.

A coupling is required between these two along with not losing too many realistic features e.g. soot formation, radiation blockage, etc. Such phenomena are modelled in the literature by using Navier-Stokes equations using a turbulence model (most often $k-\epsilon$) for closing the system of equations. A more advanced model i.e. Large Eddy Simulation (LES) is proposed by Ferziger et al. [32] where all small eddies are modelled by $k-\epsilon$ or other standard turbulence model but the large scales are solved explicitly on the computational grid. Direct Numerical Simulation (DNS) for small sized domains is considered to be the most expensive and time consuming tool for reactive flows. In DNS all the scales of motions are resolved to full accuracy and without using any models for closure. However, the use of DNS is limited to fundamental research and results obtained can be a source to modify existing RANS models [33, 34, 35]. Some LES codes were developed and validated for large fires by several research groups e.g. ISIS-3D and Fire Dynamics Simulator. Details can be found in [33, 34].

After reviewing 200 papers on the basis of multistep chemistry, more elaborate model than unity Lewis number ($Le = 1$) for molecular transport and unsteady strain rate in the reaction zone Hilbert et al. [34] conclude that there is still much to be done concerning identification of chemical pathways, accurate determination of rate constants and the development of reliable chemistry reduction techniques. They also emphasised the requirement of a proper balance between chemistry and transport models along with other realistic physical phenomena that occur simultaneously. Due to strong coupling between chemistry and diffusion of heat and species, reliable and simplified models for turbulent combustion have been developed. These models assume the chemical reaction to take place only in a single step and neglecting the effect of detailed chemical reactions in comparison to turbulent mixing. However, such approximation leads to poor results when pollutant emission and their stability is concerned. The applicability of a particular method depends mainly on the available computational resources and the details expected from the simulation. DNS calculations are often considered as 'numerical experiments' where unwanted physical effects can be excluded [34]. LES is somewhere in between RANS and DNS in terms of accuracy and cost. RANS is still the best choice for industrial applications where the mean flow quantities are primarily of concern. Hilbert et al. [34] consider RANS as an estimation of major trends of 'happening'.

Chapter 3

Experimental Investigations

3.1 Description of measuring instruments

The following measuring instruments were used to measure the physical, chemical and thermo-dynamical properties of the TBPB and TBPEH. The working principle and state of the art of each instruments are discussed in the respective sections.

3.1.1 Dynamic Differential Calorimetry (DDC)

Dynamic differential scanning calorimetry (DDC) is widely used to capture the physical and/or chemical properties changes caused by temperature variations. At the same time, the specific heat capacity at constant pressure c_p and its temperature dependence $c_p(T)$ is determined with an accuracy in the $\pm 1\%$ range [53]. The concept of Dynamic Differential Scanning Calorimetry is available as DSC (Differential scanning calorimetry) and DTA (Differential Thermal Analysis) methods. Fig. 3.1 presents the schematic of such a measuring device [36, 37, 38].

The principle of DSC is to identify the heat using a double measuring equipment. This is according to the DIN (German Institute for Standardisation) definition of the thermal analysis and temperature control. The following processes are possible by controlled programming of the temperature variation [37, 38]:

- time-linear heating/cooling
- isothermal measurements in the single-step mode

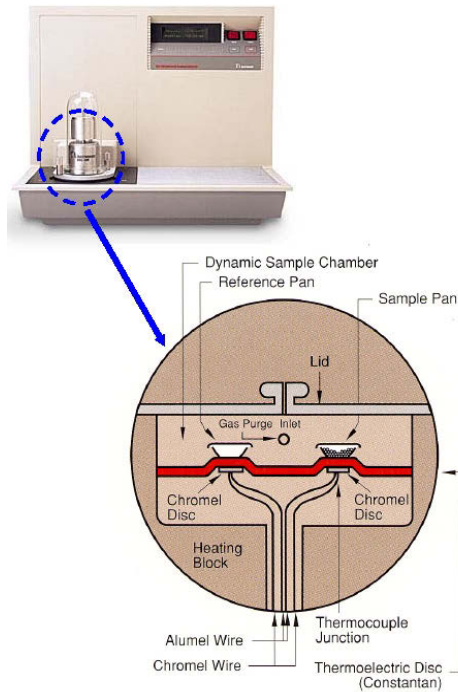


FIGURE 3.1: Schematic of a Differential Scanning Calorimeter (DSC) [36]

- isothermal measurements in the multi-step mode
- measurements with so-called modulate heating.

The DSC measures temperature difference between sample and reference with a common, highly insulated heat supply. The conversion or heat of reaction is determined by integration of peak areas considering the weight of the sample. For DSC measurements a sample size in the order of a few mg is sufficient. By DSC measurements the following quantities can be determined:

- Determination of the melting and crystallisation behaviour
- Determination of the glass transition temperature
- Determination of the specific heat capacity
- Determination of activation energy.

In this work, the DSC is used to determine the activation energy E_A of the thermal decomposition reaction of TBPB and TBPEH. The device "Pyris Diamond DSC from Perkin Elmer was used for the measurements.

The measurements were carried out at temperatures from 273 K to 523 K with heating rates of 0.2 K/min, 0.5 K/min, 1.0 K/min, 5.0 K/min, 10 K/min and 20 K/min.

3.1.2 Thermocouples

The working principle of a typical thermocouple is shown in Fig. 3.2 [43] where two wires composed of dissimilar metals are joined at both ends and one of the ends is heated, there is a continuous current which flows in the thermoelectric circuit. The open circuit voltage (the Seebeck voltage) is a function of the junction temperature and the two metals.

All dissimilar metals exhibit this effect. The most common combinations of two metals e.g. Ni-Cr or Pt-Rh. For small changes in temperature the Seebeck voltage e_{AB} is linearly proportional to temperature difference ΔT :

$$\Delta e_{AB} = \Gamma \Delta T \quad (3.1)$$

Where Γ , the Seebeck coefficient, is the constant of proportionality. The uncertainties

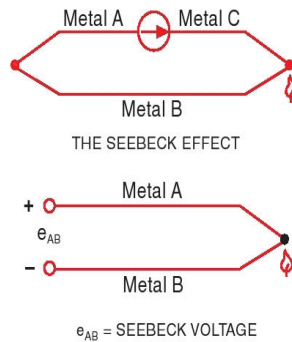


FIGURE 3.2: Schematic of a typical thermocouple

in thermocouple (K type) measured temperature in a large sooty pool fire are $\pm 8^\circ\text{C}$. Under non-uniform temperature conditions or the situation where the thermocouple can not see the flame (e.g. tilted flame under cross wind) the errors are high due to low atmospheric absorption of radiation.

3.1.3 Thermographic camera

Infrared thermography (Fig. 3.3) is the technique for producing an image of infrared light (Fig. 3.3) emitted by objects due to their thermal condition [44]. An infrared (IR) thermography system is used widely for optical measurement of temperature for a wide range of applications. The IR thermography system consists of an infrared sensor, a video camera and a computer with integrated software which converts measured irradiances in temperatures. During the test the sequence of infrared images were registered within the camera. Since the system first measures irradiance therefore, it is required to convert it into temperature by setting the emissivity, transmissivity, distance between the camera, the object ambient temperature, reflection and absorption of the flame.

The conservation of energy law states that [44]:

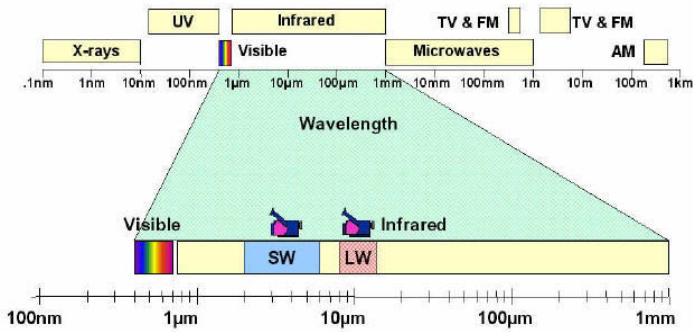


FIGURE 3.3: The electromagnetic spectrum [44]

$$\epsilon + \rho + \tau = 1 \quad (3.2)$$

ϵ , ρ and τ are emissivity, reflectivity and transmissivity respectively. For opaque targets, $\tau = 0$ and the equation reduces to:

$$\epsilon + \rho = 1 \quad (3.3)$$

According to eq. (3.3) a high emissivity means a low reflectivity. Calculations show the measurement uncertainty gets unacceptably high for target emissivities below about 0.5 [44].

The emissivity is a material property. The shape of an object affects its emissivity. Other factors affecting emissivity include: viewing angle, wavelength and temperature. The wavelength dependence of emissivity means that different IR cameras can get different values for the same object.

The major source of error in thermographic measurement comes from the wrong setting of objects emissivity as mentioned before. The other components which may introduce error are the atmospheric temperature, the background noise level and the object temperature. In general the object temperature should be 50°C higher than the background temperature [41, 42]. The situations where the noise i.e. pressure signals are much more stronger than the signals of radiation of the object may have a significant contribution towards error in measurements.

3.1.4 Radiometers

The measurements of heat flux (irradiance) at different distances from the fire are carried out by using the radiometers manufactured by Meditherm Corporation, USA. The heat flux from the fire is absorbed by the surface of the sensor (Fig. 3.4) which is covered by a purged window. The opening angle of the window can be adjusted from 7° to 150° depending on application. A number of water and purge tubes are connected to the flange for cooling and cleaning of sensors. The working principle is based on the concept

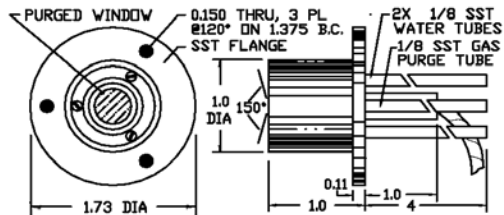


FIGURE 3.4: Schematic of a typical radiometer [96]

that the flow of heat flux between a source (sensor) and sink (reference) is proportional to the temperature difference between source and sink. The transducers at source and sink are equipped with thermocouples or thermopiles to form an electric circuit. The induced emf (electro motive force) in the circuit is directly proportional to the heat transfer rate.

The uncertainty in the radiometer measurement is $\pm 3\%$ (upto 95 % confidence level) for a range of heat flux of 2-40000 kW/m² [96].

3.2 Experimental set-ups for small and large scale fire tests

3.2.1 Construction

The fire tests were conducted in a laboratory bunker of the Federal Institute for Materials Research and Testing (BAM) and at the BAM Technical Safety Test Site. The size and the materials of the pans are given in Table 3.1. The experiments from pool diameter of 0.059 m to 0.18 m were carried out in the laboratory and from 0.5 m to 3.4 m in diameter in the outside technical safety test facility.

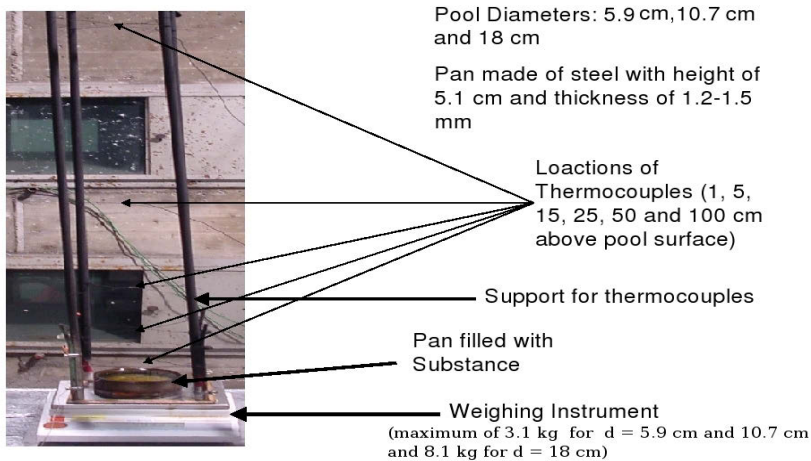


FIGURE 3.5: Small scale test set up

The arrangement of small scale tests is shown in Fig. 3.5 where the fuel pan was placed on top of a weighing instrument. The thermocouples were located at increased axial distance above the liquid pool surface. The video camera, thermographic camera and radiometers were located at a defined location (depending on the intensity of the flame) from the flame. The same arrangement was followed for the large scale test as well which can be seen in Fig. 3.6.

Pan Material	Pool Diameter (m)	Pan Height (m)	Pan Wall (m)
Steel	0.059	0.051	0.0015
Steel	0.107	0.51	0.0012
Steel	0.18	0.51	0.0012
Steel	0.5	0.08	0.003
Steel	1.0	0.08	0.003
Steel	3.4	0.08	0.003

Table 3.1: Size and material of pans



FIGURE 3.6: Large scale test set up

3.2.2 Fuels

Two organic peroxides i.e. TBPB and TBPEH (technically pure, Degussa, Arkema and United Initiators, Germany) were selected for this study. The motivation behind the selection of these two particular substances was to compare the pool fire characteristics with the large scale packaged material fire test (described in section 3.6) carried out with the same substances in 1979.

3.2.3 Mass burning rate

For the determination of the mass burning rate an electronic precision scale and load cell were used for each of the experiments in the laboratory and at the test site. The electronic precision balance Sartorius 1203C MP3 was used in combination with a DA converter Sartorius 7087 and a compensation recorder PM 8222. The writer speed and sensitivity of the scale were adjusted to the respective experimental conditions. A load cell (measuring up to 50 kg) from HWM Ltd. and a load cell (measuring range up to 500 kg) from Burfter Ltd. were used for the measurements of mass burning rates in the field tests. The central 3-point location load cell was installed and linked to a computer. Consequently, the decrease of amount of fuel during the burning time in the connected to computer records. This enabled the mass burning rate (kg/s) to be gradually seen. The mass burning rates (kg/(m² s)) have been found by the reference to the surface area of the burning pool.

3.2.4 Flame length

Flame lengths were measured by using the movie sequence recorded by a video and a thermographic camera. The instantaneous images of the flame obtained during the main burning period were then converted into time averaged value of the flame length.

3.2.5 Flame temperature

The flame temperatures were measured with the thermocouples in the laboratory experiments and with the infra-red thermography system. The thermocouples (type K, Ni-CrNi, $d = 1$ mm, type S, Pt-PtRh, $d = 0.5$ mm, Thermocoax sheath thermocouples) measured values of temperature were directly stored in computer. There were several thermocouples (depending on the size of the flame) positioned at the centre of the flame at the top and around the base of the flame.

The IR thermography system ThermaCAMTM Researcher from FLIR Systems Ltd. was used for the measurement of flame surface emission temperatures. The system has a capacity of maximum image resolution of 240 x 256 pixels in colour. The thermal sensitivity of the device lies in the range of $\Delta T = 0.08$ K at 30°C at standard 50 Hz and the accuracy is $\pm 2\%$ of measured value. Maximum 50 digital images saved within 1

s. The detectable Wavelength ranges from $7.5 \mu\text{m}$ to $13 \mu\text{m}$. The distance from fire to camera was varied according to the diameter of pool e.g. it was 62 m for $d = 3.4$ m. The emissivity was set to 0.9. The error in the temperature measurement increases with the decrease in emissivity ($T \propto \frac{1}{\varepsilon_F^{0.25}}$). The value of emissivity (0.9) seems to be reasonable for turbulence and radiation dominated pool fires as also described for optically thick hydrocarbon pool fires in [14, 27, 41, 98]. Nakos [98] carried out uncertainty analysis by considering both convective and radiative heat transfer in large hydrocarbon pool fires and concluded that the $\varepsilon_F = 0.85$ and $\bar{T} = 1300$ K under low wind conditions whereas an emissivity $\varepsilon_F = 0.4$ and $\bar{T} = 1700$ K under cross wind (10 m/s) conditions. Since the cross wind speed (see Table 3.2) in the present measurements were negligible therefore the uncertainty due to the unknown emissivity expected to be much lower.

3.2.6 Surface emissive power

The device ThermaCAMTM delivers surface temperatures of the investigated objects, as described in section 3.2.5. These temperatures can be converted to Surface Emissive Power (*SEP*) by using the the Stefan-Boltzmann law (eq. (2.38)). The selection of the emission level ε_F was based on the facts reported in [45]. The consequence of the uncertainties in the measurement of flame temperature due to the unknown emissivity will result in e.g. a lower value (when ε_F is higher) of *SEP*.

3.2.7 Irradiance

For irradiance measurements ellipsoidal radiometers (Meditherm Ltd., USA) and infrared sensors (Sensors-Inc Ltd., USA) were used. Three ellipsoidal radiometer were located near the flame and six IR sensors were located away from the flame (Table 3.2). Fig. 3.4 presents the schematic of used ellipsoidal radiometer. The head of the radiometer is constructed in the form of an ellipsoidal cavity, with the radiometer aperture in one of the focal points of the ellipsoids is located. The maximum possible opening angle is 150° . The radiometer has a fixed order during the measurements. The maximum performance of the use of first three radiometer is in the range of 200 kW/m^2 , 100 kW/m^2 and 50 kW/m^2 . The receiving wavelength range of ellipsoidal radiometer is between $0.2 \mu\text{m}$ and $7 \mu\text{m}$. During the experiments, the ellipsoidal radiometers are cooled and purged continuously using N_2 and water.



FIGURE 3.7: Location of the radiometers

Due to the performance limit (up to 2 kW/m^2), the IR sensors are placed at large distances from the flame. The operating principle is almost identical with that of ellipsoidal radiometers (see section 3.1.4), but because of the distance there was no cooling or lavage needed during the measurements. The sensor absorptance range was $0.6 \mu\text{m}$ to $15 \mu\text{m}$. During the measurements to minimise possible external influences, the sensors and ellipsoidal radiometer were kept in a metal enclosure.

Six wide opening radiometers (R_1 to R_6) have been placed at varied distances ($\Delta y = 1 \text{ m}$ to 125 m) from the rim of the pool (Fig. 3.7). The location and angles were selected in such a way that the maximum part of the luminous flame could be seen by the optical lens of the sensors.

Fuel	Pool diameter d (m)	Outside temperature (K)	Cross wind (m/s)	Relative humidity (%)
TBPB	0.5	290	1–2	63
	1.0	290	1–2	63
	3.4	290	0–0.5	60
TBPEH	0.5	290	1–2	63
	1.0	288	1–2	68
	3.4	288	0–0.5	67

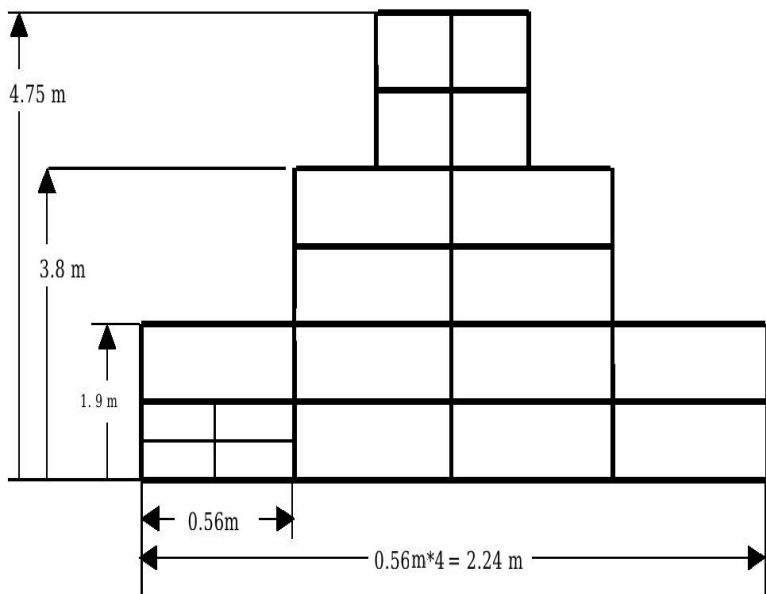
Table 3.2: Test conditions in pool fire experiments

3.3 Description of packaged material fire test

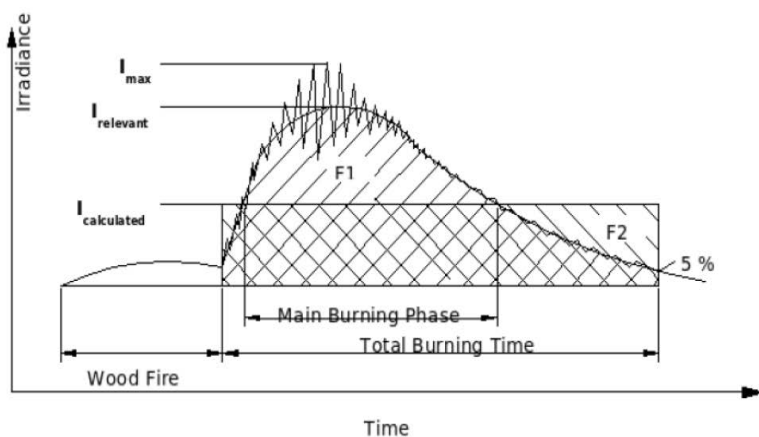
A number of large tests were carried out during past few decades in different organisations to develop uniform guidelines for safety measures for transportation and storage of hazardous substances [26, 46]. Most of such tests reported in the literature are mainly for packaged materials either solid or liquid. Two large scale tests with 5000 kg of two different organic peroxides were carried out at the BAM outside test facility in 1979. The substance chosen were tert-butyl-peroxybenzoate (TBPB) (CAS- 614-45-9) and tert-butyl per-2-ethylhexanoate (TBPEH) (CAS- 3006-82-4). A schematic of the test arrangement of different packages from front is shown in Fig. 3.8(a). Each packet consist of one inner receptacles of polyethylene and outer protective coating of cardboard and contain 25 kg in case of TBPB and 25 and 20 kg in packets for TBPEH. A number of steel tubes (thermocouples inside) were passed through the fire in order to measure temperature; these tubes were supported by two concrete walls on northern and eastern sides respectively. The construction was in accordance of class F90 of DIN4102 (German Institute for Standardisation). The packets were placed on a collecting trough of 4 m x 4 m with a rim of 0.35 m height and capacity of 5.6 m³. One important feature in their temperature measurement is the placement of thermocouples not only above the stack but also within some selected packagings [47].

Repetition of such huge tests are really very expensive and therefore a need was felt to get some prior estimation of the desired variables by means of computer simulation. However such simulations for an exact physical scenario is the next problem as the small interface between outer packaging material and the fuel has to be modelled which really makes the problem more cumbersome. But as far as the main burning phase (Fig. 3.8(b)) is concerned such fire can be represented as an equivalent pool provided that the interest lies in the time averaged behaviour and the small fluctuations could be neglected. A such approximation is presented as a second part of the work in this thesis. Furthermore, it is also tried to bring out the essentials features related to flame structure of such large organic peroxide flames without loosing much of the real physics.

The following sections summarises the test report in [28, 47] which will be helpful for validating the results obtained from simulation of an equivalent pool fire.



(a)



(b)

FIGURE 3.8: (a) Arrangement of a packaged material fire test; (b) Irradiance vs. time plot of a large packaged fire test [47]

3.3.1 Flame length

It was quite difficult to predict correctly the visible height of flame due to enormous amount of soot which covered most upper of the flame. Wind un-influenced maximum flame height for TBPB was about 20 m but 30° tilt in the direction of wind made the flame height to be 25 m (Fig. 3.9). The same visible flame height of the flame has also been reported for TBPEH. The following conclusions were drawn from the test:



FIGURE 3.9: Images of TBPB and TBPEH packaged fires (5000 kg each) [47]

1. Both peroxides do not exhibit an explosion risk if the materials are packed in weak packings provided there is no additional confinement is present.
2. Both showed high burning rate along with intense heat radiation during main fire phase.
3. The effect of surrounding temperature and substrate influenced the flame characteristics significantly.

3.3.2 Temperature measurement

Flame temperatures were recorded with twelve thermocouples (Ni-Cr) at different locations of the fire. However, it was also indicated that these measured values of temperature could not be finally treated as absolute values due to relatively low response time and different modes of heat losses to and from cooled steel column near the flame

axis on which thermocouples were fixed. Nevertheless, the maximum flame temperature measured by thermocouples were reported around 850-950°C for TBPB whereas for TBPEH it was 827-920°C. The description about uncertainties in measurements were not reported.

3.3.3 Irradiance measurement

Irradiance in different directions and distances were measured by BAM constructed and calibrated radiometers and compared with theoretical values also. A satisfactory conclusion was drawn for this comparison. The reported maximum irradiance values were not taken into account for the safety distance calculations as these values only stood for few seconds. Instead, a relevant irradiance was defined as a value between maximum irradiance and evaluated from irradiance/time record by a straightening and equalising treatment of the curve recorded during the main burning phase. Such measured value of relevant irradiance at 60 m from south was 0.64 kW/m² for TBPB fire which was 65% of the maximum irradiance and 2.78 times as much as the average irradiance.

Chapter 4

CFD (Computational Fluid Dynamics) Simulation

4.1 Introduction

Computational Fluid Dynamics (CFD) is a tool comprising of solutions of governing equations for fluid flow, heat transfer and other process associated with it. The discretized governing equations are solved over an area of interest with the known physically possible boundary conditions [48, 50, 51].

Combustion is a phenomena described by chemical reactions and fluid dynamics. Depending on the availability of oxidiser, it can be further classified into premixed and non-premixed combustion. A pool fire is an example of non-premixed combustion. With the increase in source size turbulence starts playing a dominant role in the overall behaviour of the flame. This is the reason why a large pool fire is often called as a buoyant turbulent diffusion flame where radiation acts as a major mode of heat transfer from source to the surrounding.

A mathematical model of the problem consisting of above mentioned physics can be represented in form of steady or unsteady reactive Navier-Stokes equations. Some assumptions are necessary to be made in order to solve these equations as the complexity of the problem does not allow to solve them accurately. In this chapter a description of the procedure adopted for modelling of pool fires is presented. Each part of the modelling process is described in detail in the preceding sections.

4.2 Modelling methodology

A flow chart of a model comprising basic governing equations followed by appropriate boundary conditions and subsequent solution process adopted in Ansys CFX-11.0 is shown in Fig. 4.1. The same method is followed for the simulation in this work.

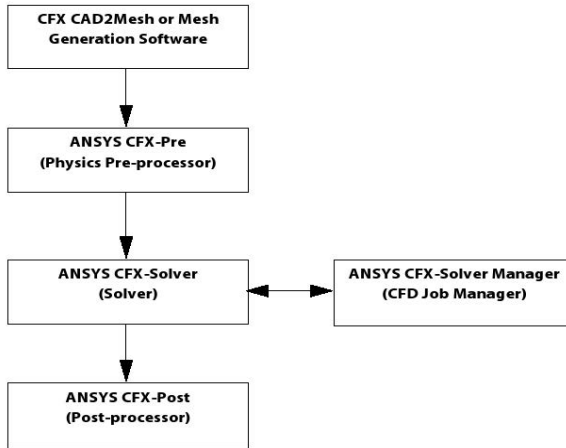


FIGURE 4.1: Flow chart of simulation process in CFX-11.0 [48]

4.2.1 Geometry, mesh and boundary conditions

The pool and the flow domain (Fig. 4.2) are modelled as axisymmetric with a diameter of 3.4 m and 8.5 m and heights of 0.08 m (rim) and 7.65 m. The pool wall (pan wall) is 0.0028 m thick. The minimum cell distance from wall to pool is 0.053 m. The scaled mesh was used for the other pool diameters. The details of mesh and boundary conditions are listed in Table 4.1 and shown in Fig. 4.2.

Alltogether more than 1 million control volumes are used for the solution of transport equations described below. Simulations have also been carried out for four other pool diameters ($d = 0.18$ m, 0.5 m, 1 m and 8 m). The size of the meshes varied according to the size of the pool. Since the mesh-dependent studies are important for the numerical solution to be independent on mesh size so it was made sure that the meshes in all cases were in accordance with the mesh independent studies of buoyant plumes in [49].

Part	Number of Elements	Boundary Boundary
Pool	3441	Inlet (mass flow rate)
Pool wall	1440	No slip, Adiabatic
Bottom wall	5580	No slip, Adiabatic
Out	19882	Opening Pressure

Table 4.1: Mesh and boundary conditions

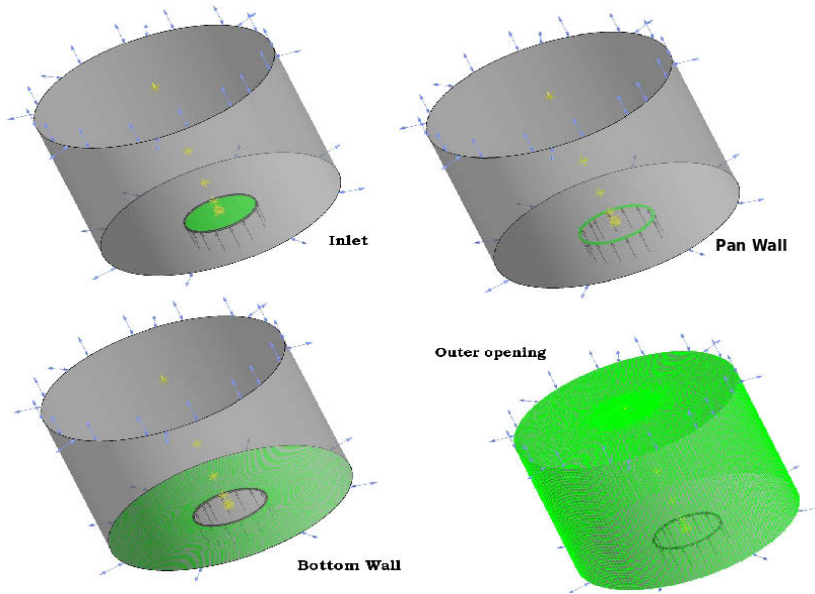


FIGURE 4.2: Mesh and boundary conditions used in simulation

4.2.2 Transport models

4.2.2.1 Multi-component flow

Multicomponent flow assumes that the various components of a fluid are mixed at the molecular level, that they share the same mean velocity, pressure and temperature fields,

and that mass transfer takes place by convection and diffusion [48]. The transport equations for mass, momentum and scalars (energy and species) for a multicomponent flow can be written in tensorial notation as follows:

Mass Conservation:

$$\frac{\partial \rho}{\partial t} + \frac{\partial(\rho U_j)}{\partial x_j} = 0 \quad (4.1)$$

Momentum Conservation:

$$\frac{\partial(\rho U_i)}{\partial t} + \frac{\partial(\rho U_j U_i)}{\partial x_j} = -\frac{\partial p}{\partial x_i} + \frac{\partial \tau_{ij}}{\partial x_j} + \rho g_i \quad (i = 1, 2, 3, \dots) \quad (4.2)$$

Scalar Conservation:

$$\frac{\partial(\rho \phi)}{\partial t} + \frac{\partial(\rho U_j \phi)}{\partial x_j} = \frac{\partial}{\partial x_j} \left(\Gamma \frac{\partial \phi}{\partial x_j} \right) + q_\phi \quad (4.3)$$

Where ρ denotes mixture density; U is the component of hydrodynamic velocity; p is the pressure and τ_{ij} is the viscous stress tensor components and g_i is the i^{th} component of the external force; ϕ stands for scalar variable i.e. species concentration and temperature; Γ is diffusivity of scalar ϕ ; q_ϕ is the source or sink of scalar ϕ .

In addition to above set of equations perfect gas law reads:

$$p = \rho \frac{R}{M} T \quad (4.4)$$

Where p , T and M are defined as pressure, temperature and molar mass. R is perfect gas constant = 8.314 kJ/(kg K) [50, 51] .

4.2.2.2 Turbulence models

Turbulence consists of fluctuations in the flow field in time and space due to which non-linearity in the conservation equations appear. Since it is beyond the scope of present computational power to solve all the scales of flow to the full accuracy therefore they need to be modelled. It has been seen that the turbulence in the pool fires controls the mixing and combustion thereon in its entirety. Therefore, it is essential to make sure that the knowledge of turbulence in pool fires from measurements are good enough to introduce

certain parameters in the empirical relations of the turbulence model. In pool fires, the time scales for turbulence i.e. the flow are much larger than the time scales of combustion i.e. chemical reactions so the pool fires are normally seen as large Damköhler number (Da) problems. The most common turbulence model used in different applications is $k-\epsilon$. In this work also for carrying out CFD simulations the $k-\epsilon$ turbulence models have been used until the flame has reached fully developed condition. SAS (Scale-Adaptive Simulation) turbulence model is also incorporated later on when the flame reached its steady state condition. According to [52] SAS is an improved Unsteady Reynolds Averaged equations (URANS) formulation, which allows the resolution of the turbulent spectrum in unstable flow conditions. The SAS concept is based on the introduction of the von Karman length-scale into the turbulence scale equation. The information provided by the von Karman length-scale allows SAS models to dynamically adjust to resolved structures in a Unsteady RANS simulation, which results in a LES like behaviour in unsteady regions of the flowfield [48]. At the same time, the model provides standard RANS capabilities in stable flow regions [52]. The detailed description on mathematical formulation could be found in [48].

4.2.3 Thermodynamic properties

The specific heat capacity (c_p) (KJ/mol) are defined by the following expressions:
 TBPB:

$$\frac{c_p}{R} = -49.61 + 4.42T - 0.001545T^2 - 5.15 \times 10^{-7}T^3 + 4.635 \times 10^{-10}T^4 \quad (4.5)$$

TBPEH:

$$\frac{c_p}{R} = -35.654 + 1.197T - 0.0004T^2 - 2 \times 10^{-7}T^3 + 1 \times 10^{-10}T^4 \quad (4.6)$$

The above expressions are based on the numerically evaluated data from ARTIST Software (Dortmund Databank Software DDBST, Oldenburg) [53] which calculates the relative transport and thermodynamic properties for the hydrocarbons for which experimental data are not available. The variation of c_p is shown in Fig. 4.3. It is assumed here that all the species have the same value of specific heat capacity which is not really true in flames. If one considers simple H_2 -air flame, the c_p for H_2 and O_2 vary as an

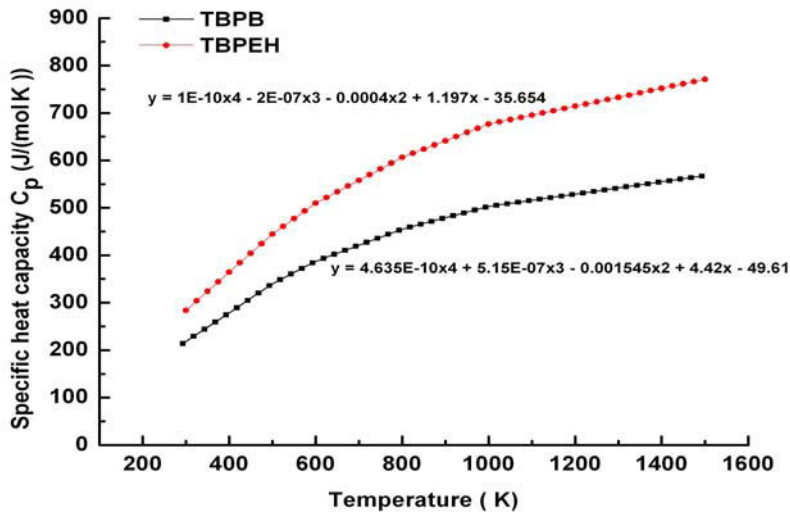


FIGURE 4.3: Computed specific heat capacity vs. temperature of TBPB and TBPEH

order of magnitude. However depending on accuracy expected from simulation leads to a compromising situation and this simplification has often been used for theoretical developments [35].

4.2.4 Combustion model

There are a number of combustion models (based on the elaboration of chemistry) are available in CFX for non-premixed combustion. Due to the unavailability of detailed chemical reaction model for organic peroxides the single step chemistry coupled with eddy dissipation model has been used in the present CFD simulations.

4.2.4.1 The eddy dissipation concept (EDC) model

In turbulent flows, this mixing time is dominated by the eddy properties and, therefore, the rate is proportional to a mixing time defined by the turbulent kinetic energy, k , and dissipation, ϵ .

$$\text{rate} \sim \frac{k}{\epsilon} \quad (4.7)$$

In many cases the reaction rates are fast compared to reactant mixing rates and can be considered as mixing controlled combustion. In the eddy dissipation concept model [102], the rate of progress of elementary reaction k , is determined by the smallest of the two following expressions:

- Reactants limiter

$$R_k = A \frac{\epsilon}{k} \min_j \frac{[I]}{\nu_{kJ}} \quad (4.8)$$

where $[I]$ is the molar concentration of component I and I only includes the reactant-components.

- Products Limiter

$$R_k = AB \frac{\epsilon}{k} \left(\frac{\sum_P [I] W_I}{\sum_P \nu_{kJ}'' W_I} \right) \quad (4.9)$$

where P loops over all product components in the elementary reaction k . The products limiter is disabled when the model coefficient B is set to a negative value. For both single step and multi-step reaction schemes the value of B set to -1 [48].

- Maximum Flame Temperature Limiter

The maximum temperature for limiting the chemical reaction in eddy dissipation model is done by either of the equation.

$$R_{k,\text{MFT}} = A \frac{\epsilon}{k} C_{\text{MFT}} \quad (4.10)$$

where

$$C_{\text{MFT}} = \max\{(T_{\text{max}} - T), 0\} \frac{\rho c_p}{-\Delta h_c} \quad (4.11)$$

C_{MFT} is virtual concentration. c_p is the specific heat capacity of the multi-component mixture at constant pressure and $-\Delta h_c$ is the heat of combustion per unit mole [48].

4.2.5 Soot models

In this work the formation of soot has been modelled by Magnussen soot model [56]. It assumes that soot is formed from a gaseous fuel in two stages, where the first stage represents formation of radical nuclei, and the second stage represents soot particle formation from these nuclei. Transport equations are solved for the specific concentration of radical nuclei, X_N [mol/kg], and for the soot mass fraction, \tilde{Y}_S [kg/kg]:

$$\frac{\partial(\bar{\rho}\tilde{X}_N)}{\partial t} + \frac{\partial(\bar{\rho}\tilde{u}_j\tilde{X}_N)}{\partial x_j} = \left(\bar{\mu} + \frac{\mu_t}{Pr_t}\right) \frac{\partial(\tilde{X}_N)}{\partial x_j} + \tilde{S}_{\text{nuclei, f}} + \tilde{S}_{\text{nuclei, c}} \quad (4.12)$$

$$\frac{\partial(\bar{\rho}\tilde{Y}_S)}{\partial t} + \frac{\partial(\bar{\rho}\tilde{u}_j\tilde{Y}_S)}{\partial x_j} = \left(\bar{\mu} + \frac{\mu_t}{Pr_t}\right) \frac{\partial(\tilde{Y}_S)}{\partial x_j} + \tilde{S}_{\text{soot, f}} + \tilde{S}_{\text{soot, c}} \quad (4.13)$$

The subscript t denotes the value for turbulent flow. Pr : Prandtl number defined as $\frac{\mu c_p}{K}$. S: Source term.

4.2.5.1 Soot formation

Formation of nuclei and soot particles is computed by following the empirical models of Tesner et al. [57] as follows:

$$C_N = \rho N_A \quad \text{part/m}^3 \quad (4.14)$$

$$C_S = \rho \frac{Y_S}{m_p} \quad \text{part/m}^3 \quad (4.15)$$

Where $A = 6.022 \times 10^{23}$ [part/mol] is number Avogadros and:

$$m_p = \rho_{\text{soot}} \frac{\pi d_{\text{soot}}^3}{6} \quad (4.16)$$

is the mass of a soot particle; ρ_{soot} and d_{soot} are the density and the mean diameter of the soot particles respectively. With the above definitions, the source terms for nuclei $\tilde{S}_{\text{nuclei, f}}$ and soot formation $\tilde{S}_{\text{soot, f}}$ can be modeled as [56]:

$$\tilde{S}_{\text{nuclei, f}} = n_0 + (f - g)C_N - g_0 C_N C_S \quad (4.17)$$

$$\tilde{S}_{\text{nuclei}, f} = m_p(a - bC_S)C_N \quad (4.18)$$

In the nuclei equation, the spontaneous formation of radical nuclei from the fuel, n_0 , is modeled using the Arrhenius approach,

$$n_0 = a_0 f_C \rho Y_{\text{fuel}} \exp\left(-\frac{T_{A,0}}{T}\right) \quad (4.19)$$

where f_C is the mass fraction of carbon in the fuel material; f is a linear branching coefficient; g is a linear termination coefficient; ρ is density of flow and g_0 is a coefficient of linear termination or radical nuclei on soot particles. In the soot equation, a and b are constants. Due to the lack of experimental data on the detailed soot properties of the pool fires of organic peroxide, the default values recommended by the CFX have been used as an approximation. The default values used by the Ansys CFX for all of the soot model parameters are given in the following Table 4.2:

Parameter	Default Value by [Part]
ρ_{soot}	2000 [kg/m ³]
d_{soot}	1.785 x 10 ⁻⁸ [m]
a_0	1.35 x 10 ³⁷ [part/kg/s]
f_c	Fuel dependent (methane 12/16, acetylene 24/26)
$T_{A,0}$	90000 [K]
$f - g$	100 [1/s]
g_0	1.0 x 10 ⁻¹⁵ [m ³ /s/part]
a	1.0 x 10 ⁵ [1/s]
b	8.0 x 10 ⁻¹⁴ [m ³ /s/part]

Table 4.2: Properties of soot [48]

The mean rates of combustion of nuclei, $\tilde{S}_{\text{nuclei}, c}$, and soot particles, $\tilde{S}_{\text{soot}, c}$ are calculated from the fuel consumption reaction rate, \tilde{S}_{fuel} in [kg/m³/s], as:

$$\tilde{S}_{\text{nuclei}, c} = \tilde{S}_{\text{fuel}} \frac{\tilde{X}_N}{\tilde{Y}_{\text{fuel}}} \quad (4.20)$$

$$\tilde{S}_{\text{soot, c}} = \tilde{S}_{\text{fuel}} \frac{\tilde{Y}_S}{\tilde{Y}_{\text{fuel}}} \quad (4.21)$$

4.2.6 Radiation model

The radiation transport equation has to be solved for obtaining the source term S in the energy equation. The spectral radiative transfer equation (RTE) can be written as [59]:

$$\frac{dI_\nu(\mathbf{r}, \mathbf{s})}{ds} = \left(-(\kappa_{a\nu} + \kappa_{s\nu})I_\nu(\mathbf{r}, \mathbf{s}) + \kappa_{a\nu}I_b(\nu, T) + \frac{\kappa_{s\nu}}{4\pi} \int_{4\pi} dI_\nu(\mathbf{r}, \mathbf{s}')\Phi(\mathbf{s} \bullet \mathbf{s}')d\Omega' + S \right) \quad (4.22)$$

where

ν : Frequency; \mathbf{r} : Position vector; \mathbf{s} : Direction vector; s : Path length; κ_a : Absorption coefficient; κ_s : Scattering coefficient; I_b : Blackbody emission intensity; I_ν : Spectral radiation intensity which depends on position (r) and direction (s); T : Local absolute temperature; Ω : Solid angle; Φ : In-scattering phase function; S : Radiation intensity source term.

For diffusely emitting and reflecting opaque boundaries it can be written that

$$I_\nu(r_w, s) = \epsilon_\nu(r_w)I_b(\nu, T) + \frac{\rho_w(\mathbf{r}_w)}{\pi} \int_{n \bullet \mathbf{s}' < 0} I_\nu(\mathbf{r}_w, \mathbf{s}') |\mathbf{n} \bullet \mathbf{s}'| d\Omega' \quad (4.23)$$

where ϵ_ν : spectral emissivity [48, 59].

The discrete transfer radiation model is used in the CFD simulation in this work is described as follows.

4.2.6.1 Discrete transfer model

The implementation of the discrete transfer radiation model in ANSYS CFX assumes that the scattering is isotropic; therefore, eq. (4.22) can be further simplified as:

$$\frac{dI_\nu(r, s)}{ds} = -(\kappa_{a\nu} + \kappa_{s\nu})I_\nu(r, s) + \kappa_a I_b(\nu, T) + \frac{\kappa_{s\nu}}{4\pi} \int_{4\pi} I_\nu(\mathbf{r}, \mathbf{s}') d\Omega' + S \quad (4.24)$$

Assuming that the system is reasonably homogeneous, so that:

$$I_\nu(r) \sim I_\nu(r + dr)q_\nu^R(r) \sim q_\nu^R(r + dr) \quad (4.25)$$

the approach is then to solve for the intensity, I_ν , along rays leaving from the boundaries using the equation of transfer:

$$I_\nu(r, s) = I_{\nu 0}\exp(-(\kappa_{a\nu} + \kappa_{s\nu})s) + I_{b\nu}(1 - \exp(-\kappa_a s)) + \kappa_{s\nu}\bar{I}_\nu \quad (4.26)$$

where:

$I_{\nu 0}$: Radiation intensity leaving the boundary; I_ν : Mean radiation intensity.

The spectral incident radiation G can be obtained by integrating I over solid angle at discrete points. The radiative heat flux q_r can be determined by using the homogeneity assumption to extend the solution to the entire domain. Since the objective of thermal radiation modelling is to obtain the total volumetric absorption and emission, additional calculations are still needed. For the grey spectral model, the calculation is done once for a unique radiation intensity field. When coherent radiation field is assumed the solution obtained at a given frequency is independent of at all other frequencies [48, 59].

4.3 Solution strategy

For solving the hydrodynamic equations ANSYS CFX uses a coupled solver i.e pressure and velocity terms are solved simultaneously. When simulating steady state problems, the time-step acts as an acceleration parameter which guides the solution to a defined path until convergence has reached. In case of transient simulations the coefficient loop iterations are required to bring down all the variables below the target criterion of convergence [48]. The time step size (Δt) of 0.01 to 0.0001 second is used depending on the pool diameter and fineness of the grid. Five coefficient loop iteration for each time step is set with 8 CPUs of 2 GB of memory each for a target criterion of 10^{-4} for all variables. Time dependent transport equations are solved by using second order backward Euler method with an implicit finite volume method.

The flow chart shown in Fig. 4.4 illustrates the general field solution process used by the ANSYS CFX-Solver.

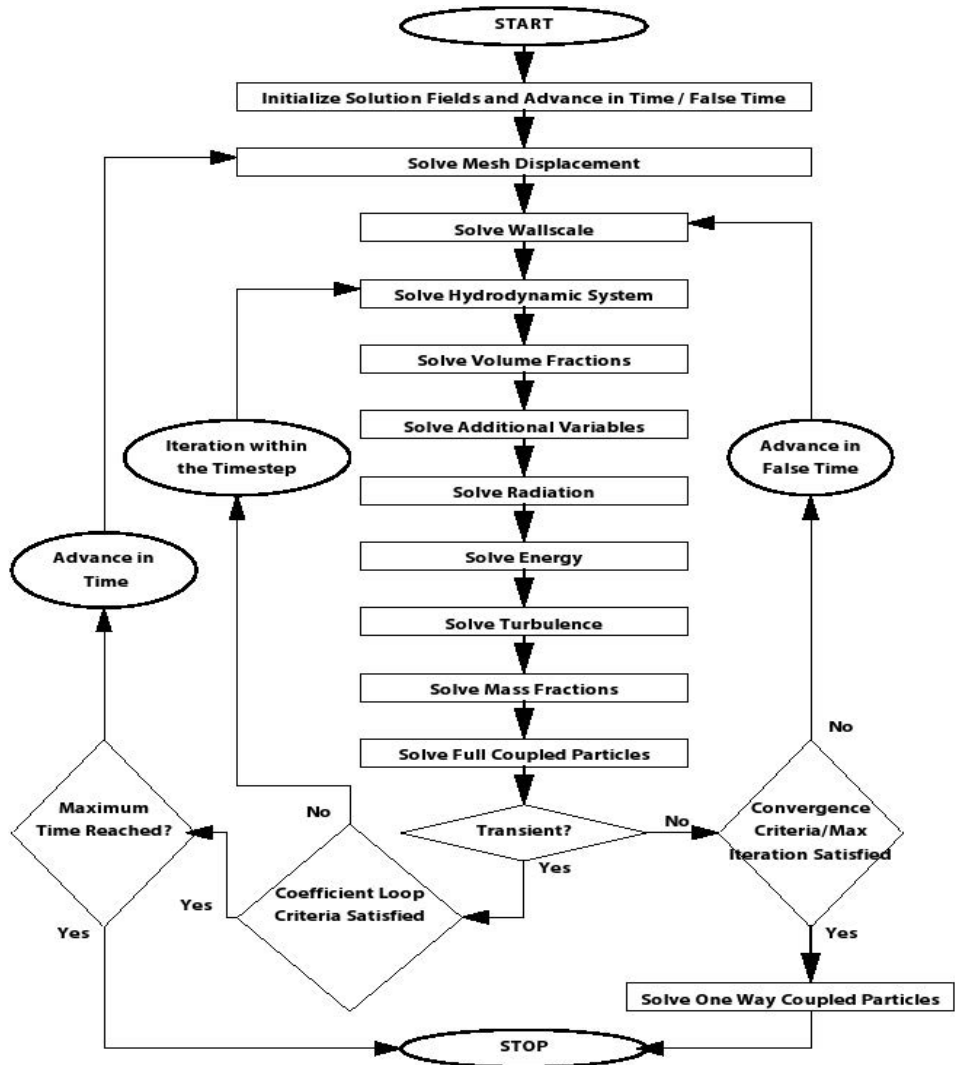


FIGURE 4.4: Flow chart of solution process in CFX [48]

The solver proceeds in each timestep as follows:

1. Coefficient generation: It linearises the non-linear equations and generates the solution matrix.
2. Equation solution: The linear equations are then solved by using an algebraic multi-grid method.

The obtained solution matrix can be then visualised by a post-processor.

Chapter 5

Results and Discussion

5.1 Mass burning rate

5.1.1 Mass burning rate as a function of pool diameter

The dependence of measured mass burning rates \bar{m}_f'' versus the pool diameter d of organic peroxides and kerosene is shown in Fig. 5.1. It is already established that \bar{m}_f'' of hydrocarbon pool flames is a function of d until it reaches the turbulent regime however some deviation from the above known fact is shown in [60] where the \bar{m}_f'' of diesel and gasoline were found to be increased for $1 \text{ m} \leq d \leq 6 \text{ m}$. As shown in Fig. 5.1 the \bar{m}_f'' of kerosene becomes independent of d at or after 0.3 m whereas organic peroxide pool flames show this independence right from the smallest d .

This can be seen for all peroxides (DTBP[62], TBPB, TBPEH and INP[61]) in Fig. 5.1 which undoubtedly are fully developed turbulent flames and are independent of size of the source d . The mass burning rate (for $d \leq 3.4 \text{ m}$) of a large diameter pool of organic peroxide can be written in the following way

$$\bar{m}_{\text{max}}'' \approx \bar{m}_f'' \quad (5.1)$$

which means that a finite diameter pool flame of organic peroxide burns with the same rate like a very large diameter pool flame. It also signifies the importance of the properties of the fuel on the fluid dynamical behaviour of the flame. In case of pool fires

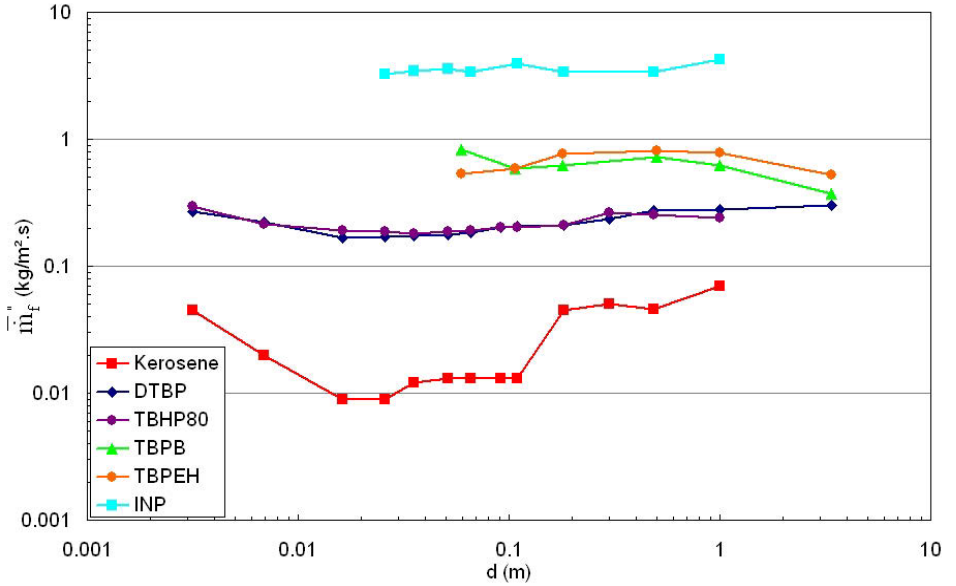


FIGURE 5.1: Measured \bar{m}''_f vs. d of kerosene and organic peroxide pool flames [89]

of organic peroxides the fuel properties deliver the turbulence and therefore size of the source i.e. pool diameter has negligible influence on the burning rate [63].

As can be seen in Fig. 5.1 the organic peroxide pool fires burn almost about 4-60 times faster (for $d = 1$ m) than a corresponding flame of kerosene. The three different regimes laminar, transition and turbulent as described for hydrocarbons [5, 6] are not observed for all the investigated organic peroxides (see also [61, 62]). This fact is correct for the values in Fig. 5.1 which were obtained for mass loss of 60% of the total fuel mass. For smaller d the mass burning rate for 60% mass loss was not measurable because the flames were extinguished due the lack of heat conduction through the pan walls however the mass burning rates were very high before these flames extinguished [61]. The transition regime can not be observed for organic peroxides because the higher mass burning rate is radiation dominated. For further discussion see section 5.1.2.

The values of \bar{m}''_{\max} of hydrocarbons and organic peroxides are listed in Table 5.1

Fuel	JP-5	LNG	LPG	Gasoline	Kerosene	Kerosene ^a	DTBP ^a	TBPB ^a	TBPEH ^a
Measured $\overline{\dot{m}}''_{\max}$ (kg/(m ² s))	0.054	0.078	0.099	0.085	0.039	0.068	0.300	0.370	0.530

Table 5.1: Measured $\overline{\dot{m}}''_{\max}$ of hydrocarbons and organic peroxides^aMeasured at BAM.

The uncertainties associated with the measurement of $\overline{\dot{m}}''_f$ for large pool fires i.e. $d \geq 1$ m are mainly influenced by the properties of the fuel e.g. boiling point, enthalpy of vaporisation and the field conditions e.g. ambient temperature and wind velocity. The strength of cross wind affects the fluctuations in fire up to a great extent. These fluctuations in fire directly contribute to the uncertainties in the measurement. In present measurements, the effect of cross wind in $d = 3.4$ m tests were negligible (see Table 3.2) therefore errors and uncertainties caused by cross wind can be neglected and higher accuracy can be assured. The range of uncertainty (based on present measurement and in [61]) in the measurement of $\overline{\dot{m}}''_f$ for $d = 1$ m for TBPB pool fire is $\pm 13\%$.

5.1.2 Mass burning rate as a function of Self-Accelerating Decomposition Temperature (SADT)

The discussion in section 5.1.1 does not provide enough facts to explain the behaviour of organic peroxide pool fires. Therefore some characteristic data of these organic peroxides are summarised in Table 5.2. These listed data show that the organic peroxides with the lowest active oxygen content, the lowest heat of decomposition shows the highest mass burning rate. On basis of the data only one conclusion is plausible. The mass burning rate of the investigated peroxides depends on their nature to decompose at different temperatures. The ordering depends on the SADT, on the extrapolated onset temperature as determined by DSC and consequently on the half-life temperature.

The amount of energy from decomposition which is additionally released (before, during or after vaporisation depending on the peroxide) is obviously not so important as the SADT and the extrapolated onset temperature. This leads to the conclusion that for organic peroxides as low as the SADT as higher as the mass burning rate (Fig. 5.2) [90]. As can be seen in Fig. 5.2 that the mass burning rate of organic peroxides linearly

increases with the decrease in decomposition temperature. An expression for \bar{m}''_{\max} in terms of decomposition temperature can be established as written below:

$$\bar{m}''_{\max} = 68679 \left(\frac{\text{kg}}{\text{m}^2\text{s}} \right) \exp \left(-0.0348 \left(\frac{T_{\text{SADT}}}{1[\text{K}]} \right) \right) \quad (5.2)$$

Eq. (5.2) could be further utilised for estimating the \bar{m}''_{\max} of different organic peroxides.

Parameter	INP	TBPEH	TBPB	DTBP
Formula	C ₁₈ H ₃₄ O ₄	C ₁₂ H ₂₄ O ₃	C ₁₁ H ₁₄ O ₃	C ₈ H ₁₈ O ₂
Molar mass (g/mol)	314.5	216.32	194.2	146.2
Active oxygen (%)	5.09	7.40	8.24	10.94
Enthalpy of combustion ($-\Delta h_c$)(kJ/kg)	30100	34455	30113	36600
Enthalpy of decomposition ($-\Delta h_{\text{dec}}$)(kJ/kg)	954	1158	1377	1365
Enthalpy of vaporisation (Δh_v) (kJ/kg)	-	226	268	212
Boiling point (K)	-	527	556	384
T_{SADT} (K)	293	308	338	358
Extrapolated onset temperature (K)	358	-	387	396
1 min half life temperature (K)	393	403	438	463
\bar{m}''_f ($d = 1$ m)	4.22	0.78	0.62	0.29
$\bar{m}''_f = 10^{-3} \left(-\frac{\Delta h_c}{\Delta h_v} \right)$, $d = 1$ m	-	0.15	0.11	0.17

Table: 5.2: Properties of different organic peroxides

The enthalpy of vaporisation of the investigated peroxides are lower than the respective enthalpy of decomposition, if the fire is stable. Consequently the heat flux back from the flame to the liquid surface leads to a violent vaporisation and higher mass burning rate.

It is also shown in Table 5.2 that the commonly used equation to estimate the maximum mass burning rate of hydrocarbon pool fires i.e. eq. (2.3) is not suitable for organic peroxides. All organic peroxides have comparable enthalpy of combustion and enthalpy of vaporisation but their measured mass burning rate are much higher than calculated by eq. (2.3).

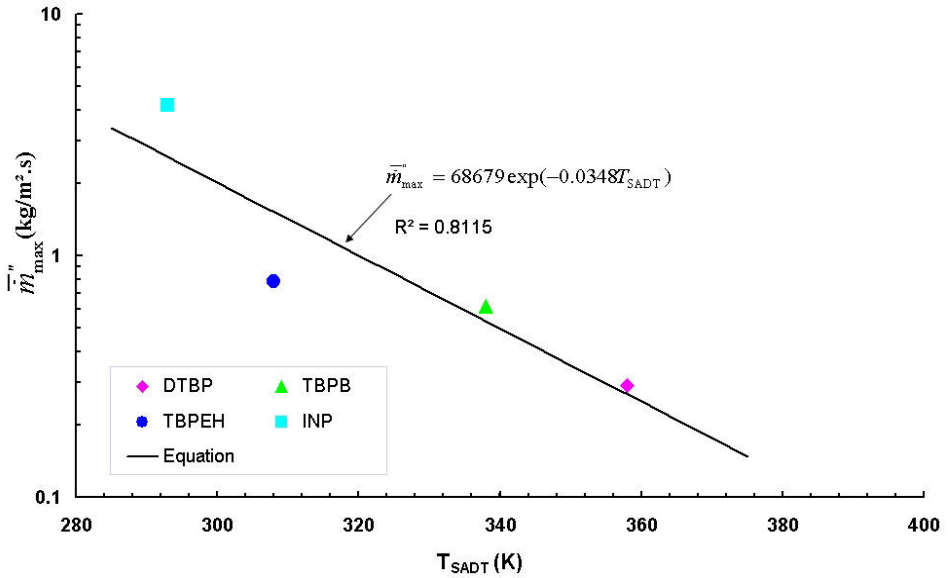


FIGURE 5.2: \bar{m}''_{\max} vs. T_{SADT} of organic peroxides

5.1.3 CFD prediction

The prediction of flame temperature, velocity, irradiance and surface emissive power were carried out in the past by using CFD simulation with various sub models for turbulence and chemistry. Almost all numerical work carried out so far concentrated on the dynamics of fire plume and CFD modelling of the burning rate of the fuel was not done yet. Since it requires the modelling of the evaporation and the model complexity in a multiphase problem extends furthermore when natural convection also involved with it so most of the simulation only considers the gas phase combustion in pool fires and ignores the evaporation phase. Here also the gas phase combustion simulation has been carried out and the way to predict the burning rate following the mass balance across the combustion zone is presented [64]. A schematic of a typical pool fire can be seen in Fig. 5.3 where two zones are shown in vertical direction.

The clear flame zone (combustion zone) shown as yellow colour is defined between sections f-f and g-g (Fig. 5.3). The following mass balance equation can be derived from a one dimensional stationary continuity equation around liquid surface f-f.

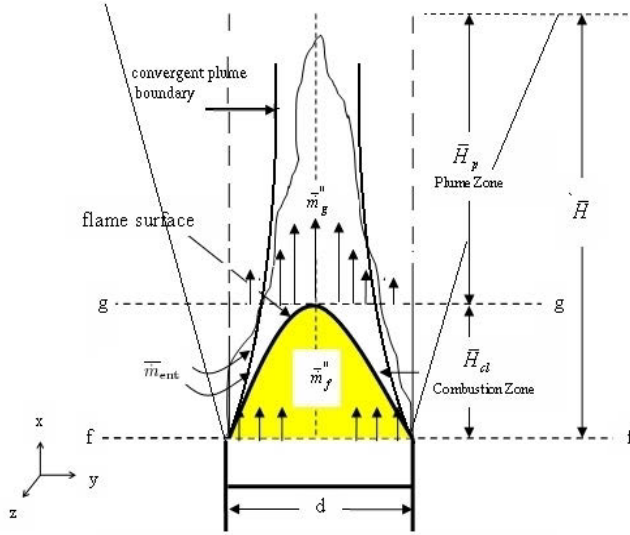


FIGURE 5.3: Mass balance across combustion zone in a pool fire

$$\bar{m}_f'' = \bar{m}_v'' + \rho_v v_b \quad (5.3)$$

where $\bar{m}_v'' = \rho_v u_v$: mass flow rate of fuel vapour ($\text{kg}/(\text{m}^2\text{s})$).

Since in a typical pool fire the fuel vapour velocities thereby fuel Froude number vary only over less than an order of magnitude unlike jet flames where it spans over five orders of magnitude. Therefore Fay [9] assumes that the air entrainment flow rate is given by the following relation:

$$\bar{m}_{\text{ent}} \propto \rho_a d \bar{H}_{\text{cl}} \sqrt{g \bar{H}_{\text{cl}}} \quad (5.4)$$

following the above eq. (5.4) proposed by Fay's entrainment model it can be written that

$$\bar{m}_{\text{ent}} = \rho_a d \bar{H}_{\text{cl}} \sqrt{2g \bar{H}_{\text{cl}}} \quad (5.5)$$

Now with the help of this eq. (5.5) the \bar{H}_{cl} can be calculated for a large pool diameter i.e. $d = 1$ m where the burning rate becomes independent of the pool diameter. From

eq. (5.4) and eq. (5.5) Fay [9] deduced that

$$\overline{H}_{cl} \propto d^{\frac{2}{3}} \quad (5.6)$$

The length of combustion zone \overline{H}_{cl} for other diameter pools can be calculated with the help of eq. (5.6).

By carrying out mass balance around the section g-g it can be shown that

$$\overline{m}_g'' \left(\frac{\pi d^2}{4} \right) = \overline{m}_{ent} + \overline{m}_f'' \left(\frac{\pi d^2}{4} \right) \quad (5.7)$$

Here, it is further assumed that the mass of air entrained \overline{m}_{ent} is much smaller than \overline{m}_f'' , so

$$\overline{m}_g'' \left(\frac{\pi d^2}{4} \right) = \overline{m}_f'' \left(\frac{\pi d^2}{4} \right) \quad . \quad (5.8)$$

In eq. (5.8) follows that the mass flow rate of hot gases \overline{m}_g'' with the definition $\overline{m}_g'' = \langle \overline{\rho}_g \overline{u}_g \rangle$ is

$$\overline{m}_g'' = \overline{m}_f'' \quad . \quad (5.9)$$

The variables $\overline{\rho}_g$, \overline{u}_g in \overline{m}_g'' can be computed with the help of 3-D reactive Navier-Stokes equations above the combustion zone H_{cl} . From eq.(5.9) it follows that the mass flow \overline{m}_g'' is equal to the fuel mass burning rate for a finite diameter pool [64].

For the prediction of the burning rate of fuel from simulation one needs to know the length of combustion zone where all the fuel and oxidiser have been fully consumed and what is left is only hot combustion products. The CFD predicted \overline{m}_f'' for TBPB and TBPEH pool fires ($d = 0.18$ m, 0.5 m and 1 m) is shown in Fig. 5.4 together with measurements. These predictions were made when the flame has reached fully developed steady burning conditions. From the safety point of view (safety and protection distances) the agreement between the CFD predicted mass burning rates for TBPEH pool fires are relatively good for $d = 1$ m. Contrary to this the CFD predicted mass burning rates for TBPB pool fires agree well with experimental values for smaller d . The deviation for $d = 1$ m should be concluded on the basis of the discussion given in sections 5.2 and 5.4.

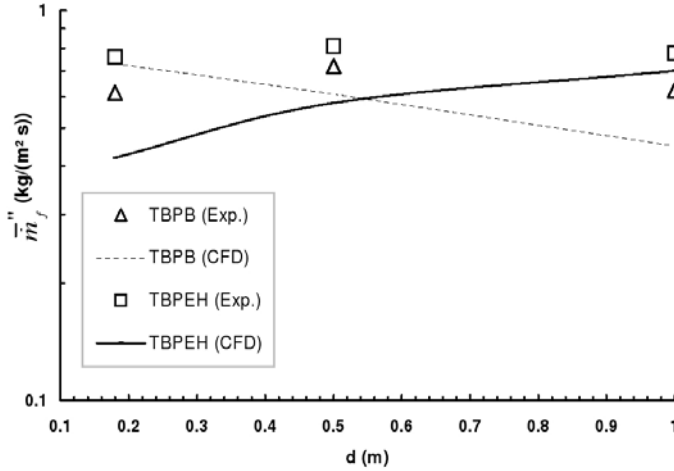


FIGURE 5.4: Measured and CFD predicted $\overline{\dot{m}}_f''$ of TBPB and TBPEH pool fires

5.2 Visible flame length

As can be seen in Fig. 5.1 small TBPB and TBPEH pool flames burn almost 100 times faster than a corresponding kerosene flames. The visible length of smoky organic peroxide flames were determined by observation of the highest luminous part on the basis of thermographic and videographic images. Due to the much higher mass burning rates the flame extends its visibility to a larger length. When comparing with kerosene flames one finds that the relative visible flame lengths are about 3–5 times larger (Fig. 5.5). Additionally, the TBPB flame has distinct features of pulsation leading to a lower value of $\frac{\overline{H}}{d}$ than in case of the TBPEH flame. This self-controlled pulsation of TBPB pool flame is discussed in section 5.4.

The visible flame length of large pool fire ($d = 3.4$ m) of TBPB and TBPEH are shown in Fig. 5.6. The determination of time averaged relative flame length $\frac{\overline{H}}{d}$ was done by following the Zukoski's intermittency criterion [65]. The length was selected above which the flame maintains its height for more than 50% of the time during main burning phase. If compare with large hydrocarbon pool fire the $\frac{\overline{H}}{d}$ of organic peroxides are 4 to 4.5 times larger than a corresponding flame of Diesel ($\frac{\overline{H}}{d} \sim 2$) [60].

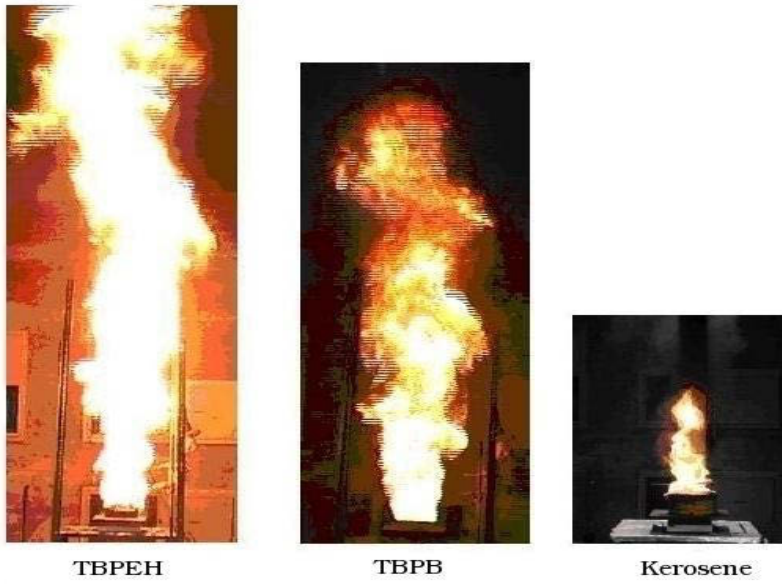


FIGURE 5.5: Visible instantaneous photographic images of TBPEH ($\frac{\bar{H}}{d} = 16.7$), TBPB ($\frac{\bar{H}}{d} = 8.9$) kerosene ($\frac{\bar{H}}{d} = 3.3$) pool fires ($d = 0.18$ m)

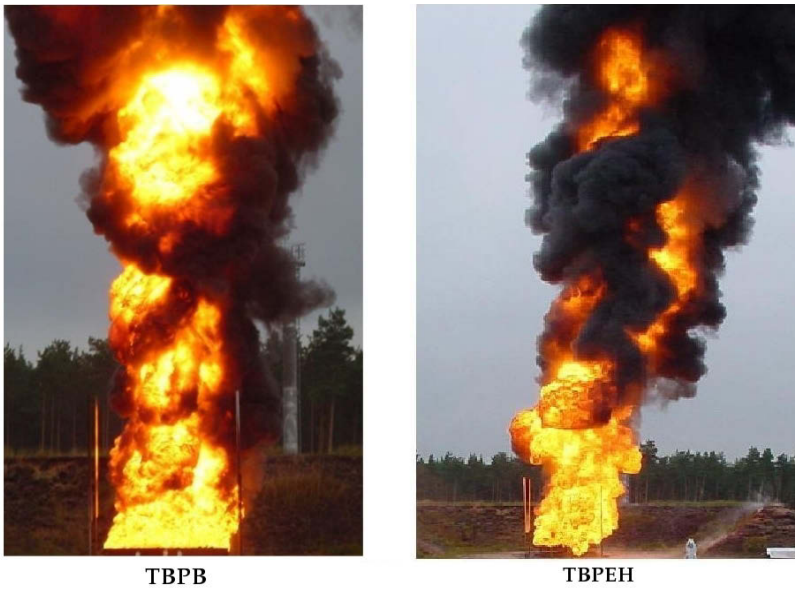


FIGURE 5.6: Visible instantaneous photographic images of TBPB ($\frac{\bar{H}}{d} = 9$) and TBPEH ($\frac{\bar{H}}{d} = 8$) pool fires ($d = 3.4$ m)

5.2.1 Visible flame length as a function of pool diameter

Fig. 5.7 presents the dependence of time averaged relative flame lengths of TBPB, TBPEH and kerosene on pool diameter. The measured flame lengths for $d = 0.5$ m and

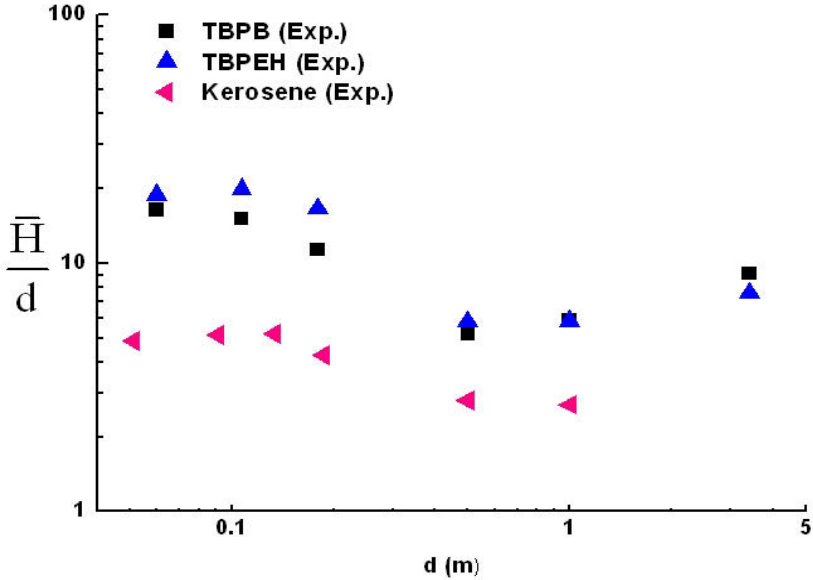


FIGURE 5.7: Relative flame lengths of kerosene, TBPB and TBPEH pool fires as a function of d

1 m are corrected (by trigonometric relationship between vertical and tilted flame) for the cross wind effects whereas for $d = 3.4$ m the cross wind effects were negligible so no corrections were applied (see Table 3.2). Time averaged relative flame lengths of a number of hydrocarbon pool fires have been measured and reported in [5, 7, 8, 9, 11, 14, 16, 17] where the $\frac{\bar{H}}{d}$ found to be decreased with pool diameter and for large pool diameter it was shown that $\frac{\bar{H}}{d} \sim 2$. In Fig. 5.7 the same can be seen for kerosene whereas TBPB and TBPEH show little increase in $\frac{\bar{H}}{d}$ for $d \geq 1$ m. However, this generalisation is only valid for $d \leq 3.4$ m. If comparing with kerosene ($d = 1$ m) the $\frac{\bar{H}}{d}$ of organic peroxides pool fires are two times larger [60, 62].

5.2.2 Visible flame length as a function of fuel Froude number

In Fig. 5.8 the time averaged relative visible flame lengths for three pool diameters of kerosene, TBPB and TBPEH are plotted against fuel Froude numbers. The Fr_f of organic peroxides are 100 times higher than for kerosene. That means that the peroxide flames behaviour is similar to a low momentum jet diffusion flame and hydrocarbon flames are buoyancy driven (depending on d). The mass flow average velocity with which the peroxide vapours leave the liquid pool surface is (~ 1 m/s) whereas conventional hydrocarbon pool vapour velocities lie within 0.02-0.1 m/s [9, 11]. This also justifies the proximity of organic peroxide pool flames to low momentum jet flames [66].

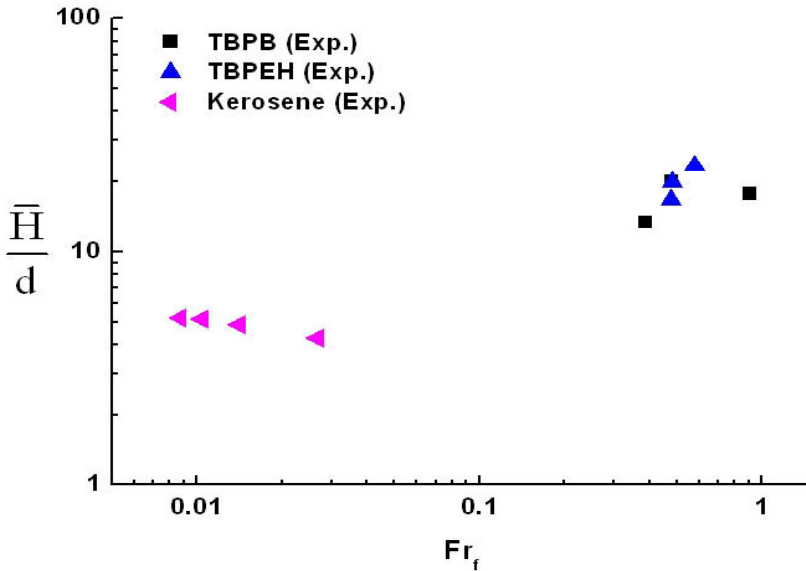


FIGURE 5.8: Relative flame lengths of kerosene, TBPB and TBPEH as a function of Fr_f

5.2.3 Flame length prediction according to the models of Thomas and Fay

It was also shown in many past investigations [7, 9] that the length of a turbulent buoyant flame is a function of fuel Froude number (see also eqs. (2.12) and (2.28)). In Fig. 5.9 it can be seen that organic peroxides follow neither the equation derived by Thomas nor

by Fay (eqs. (2.12) and (2.28)) rather it shows a decrease in $\frac{\bar{H}}{d}$ as the $Fr_f^{\frac{2}{5}}$ increases. To describe this new behaviour of these two peroxide flames further experiments must be carried out and a new model should be developed. The following correlations eqs.

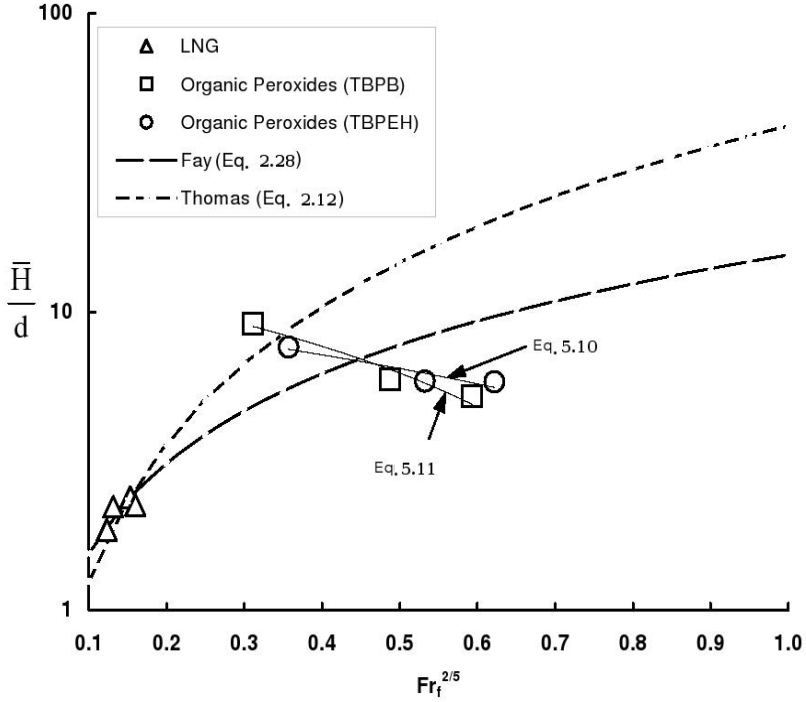


FIGURE 5.9: Relative flame lengths of hydrocarbons and organic peroxides as a function of Fr_f

(5.10) and (5.11) state that the elevation of virtual origin (the d at which $\frac{\bar{H}}{d} \leq 1$) [67] for TBPB and TBPEH are 1.43 cm ($Fr_f = 0.85$) and 1.52 cm ($Fr_f = 1.14$) respectively.

$$\left(\frac{\bar{H}}{d}\right)_{\text{TBPB}} = 13.382 - 14.305 (Fr_f)^{\frac{2}{5}} \quad (5.10)$$

$$\left(\frac{\bar{H}}{d}\right)_{\text{TBPEH}} = 10.05 - 7.195 (Fr_f)^{\frac{2}{5}} \quad (5.11)$$

A situation of mass fire (a situation where the diameter of the pool comes in the range of km [67]) for organic peroxides could occur at these small diameters whereas hydrocarbons

show such behaviour at very large diameters (Fig. 5.9) [63].

5.2.4 Flame length prediction according to Heskestad's model

A number of semi-empirical models have been developed and tested for predicting the height of large turbulent fire plume of a variety of hydrocarbons. An equation developed by Heskestad [67] considers the chemical and thermodynamic properties of fuel into account and follows the idea of McCaffrey [8] and Steward [17].

In order to calculate the combustion number N (eq. (2.22)) the following data are used: $-\Delta h_c = 30113$ kJ/kg for TBPB and 34455 kJ/kg for TBPEH; $r_{st} = 13$ for TBPB and 16.5 for TBPEH; $\rho_a = 1.2$ kg/m³; $g = 9.8$ m/s²; $c_p = 1$ kJ/(kg K); $T_a = 283$ K.

In Fig. 5.10 a satisfactory agreement can be seen between the measured and predicted (with eq. (2.21)) values of $\frac{\bar{H}}{d}$ for the two organic peroxides with $d = 3.4$ m. The $\frac{\bar{H}}{d}$ of

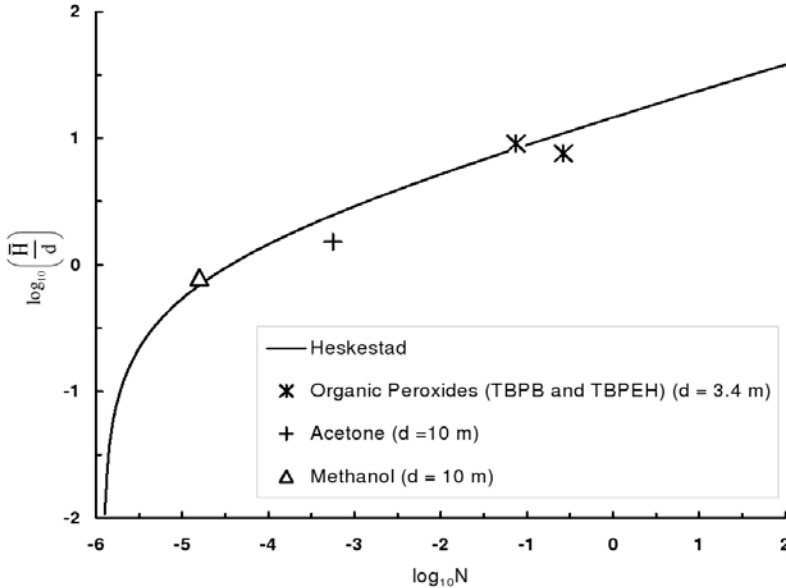


FIGURE 5.10: Relative flame lengths of hydrocarbons and organic peroxides as a function of N

ketones and alcohols (acetone and methanol) can also be seen in Fig. 5.10 which are almost 6 to 9 times smaller than the organic peroxide pool flames. The mass burning rate of methanol also does not vary appreciably with pool diameter [13, 93] and therefore

was chosen here as reference fuel for the comparison with organic peroxides.

The soot formation extends the complexities more in the correct measurement of the visible flame length of a large pool fire. These soot particles appear and disappear with the fluctuation in the fire. Since the fluctuations in the pool fires become smaller with the increase in diameter (see also section 2.2.2.7) therefore, the time resolution (25 frames per second) of the present videographic camera was good enough to capture the small fluctuations in the flame. The obscuration of the flame behind the black soot has been seen in the videographic images. These hide and seek between flame and soot introduce many unknown errors and uncertainties in the measurements. Due to this only a qualitative estimation of uncertainty can be given. Such an estimated uncertainty in the measurement of $\frac{\bar{H}}{d}$ (between present measurements and in [61]) for TBPB ($d = 1$ m) is $\pm 9\%$.

5.2.5 CFD prediction

Prediction of flame length by means of CFD simulation can be done by using the CFD predicted mass burning rates as discussed in the section 5.1.3. The semi-empirical models developed for many hydrocarbon fuel pool fires indicate that there is a dependence of flame length on fuel mass burning rate. By using eq. (2.12) with experimentally determined constants A and B listed in Table 5.3 the $\frac{\bar{H}}{d}$ were calculated for TBPB and TBPEH pool flames.

Fuel	A	B
TBPB	21	0.61
TBPEH	38	0.61

Table 5.3.: Experimentally determined constants A and B used in eq. (2.12)

Thomas performed experiments on the wood crib fires and reported the value of A and B as 42 and 0.61 respectively. Without changing the exponent i.e. B in eq. (2.12) estimates the $\frac{\bar{H}}{d}$ of TBPB quite satisfactorily (Fig. 5.11) whereas the prediction of TBPEH needs further adjustment of B. More experimental data will help to develop precise values of

A and B and finally a general relationship according to eq. (2.13) for organic peroxides could be realized.

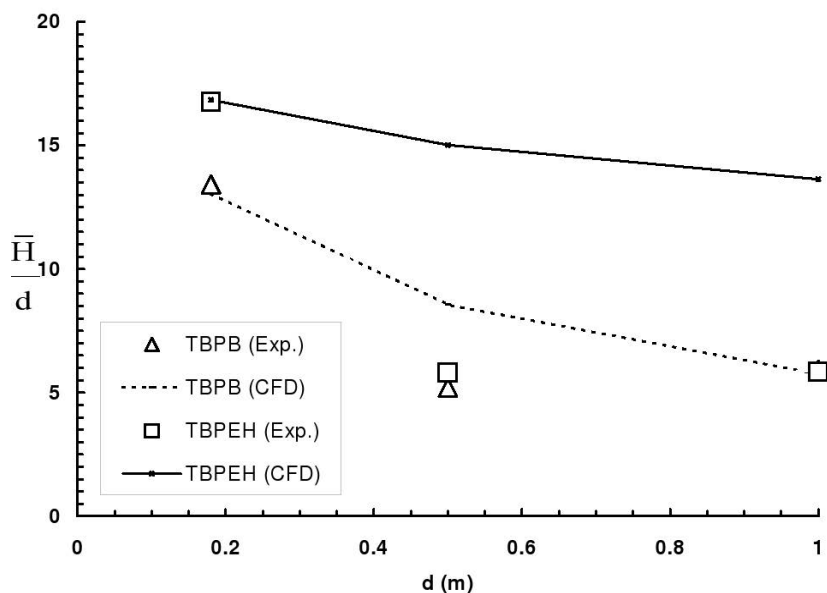


FIGURE 5.11: Measured and CFD predicted relative flame lengths

5.3 Turbulent organised structures

An instantaneous thermogram contains data of temperatures in a matrix of 240 x 256. By carrying out some scaling one can get an analytical detailed view of temperature distribution near to the pool surface. Here, a square section of 0.4 m x 0.4 m just above the pool of $d = 0.18$ m is selected with the assumption that it can represent the combustion zone. A square matrix of 32 x 32 an instantaneous image above pool contains data in 0.4 m x 0.4 m. A contour plot of kerosene, TBPB and TBPEH during steady burning (when it reaches at the first time) period is shown in Fig. 5.12, Fig. 5.13 and Fig. 5.14. For temperature interpretation see section 5.5.

TBPB shows a structure of fully developed turbulent diffusion flame whereas kerosene shows more organised structure along with transition to turbulence due to a strong influence of buoyancy. A random distribution of turbulence intensity due to higher rate of decomposition, lower enthalpy of vaporisation, lower boiling point and lower SADT

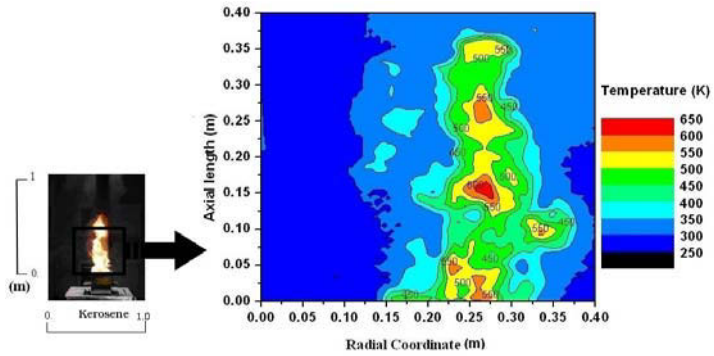


FIGURE 5.12: Typical instantaneous thermogram showing flame temperature within the clear flame zone for kerosene ($d = 0.18$ m)

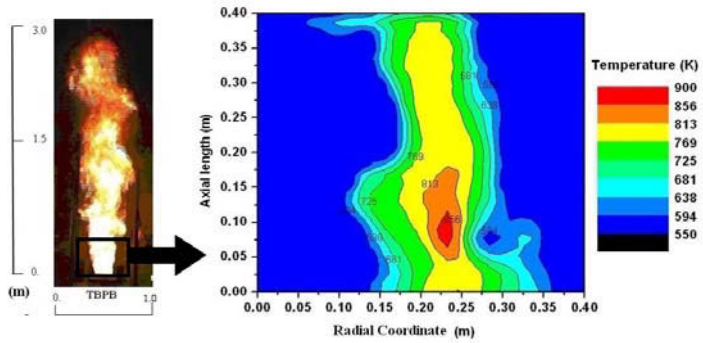


FIGURE 5.13: Typical instantaneous thermogram showing flame temperature within the clear flame zone for TBPB ($d = 0.18$ m)

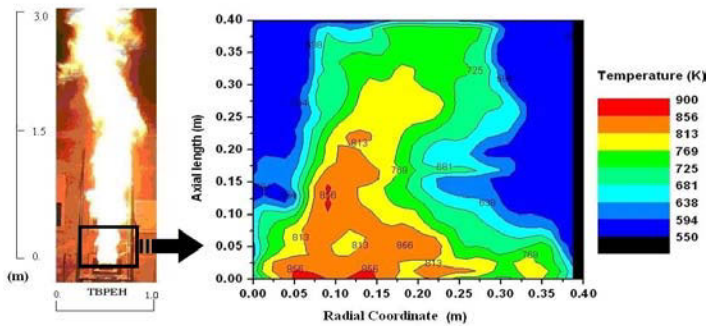


FIGURE 5.14: Typical instantaneous thermogram showing flame temperature within the clear flame zone for TBPEH ($d = 0.18$ m)

for TBPEH influences the organised structure more than in case of TBPB flame (see Table 5.2). This leads also to the larger visible length of the TBPEH flame [68, 69]

5.4 'W'-effect in a TBPB pool flame

A pulsation of TBPB flame with different time intervals has been observed. On the other hand TBPEH shows burning with diameter depending frequency. Such a pulsation in pool flames was not observed for all fuels so far, including other organic peroxides investigated here. In small-scale tests e.g. $d = 5.9$ cm a small flame (~ 12 cm) is observed about 10 s after ignition. As shown in Fig. 5.15 some seconds later the flame

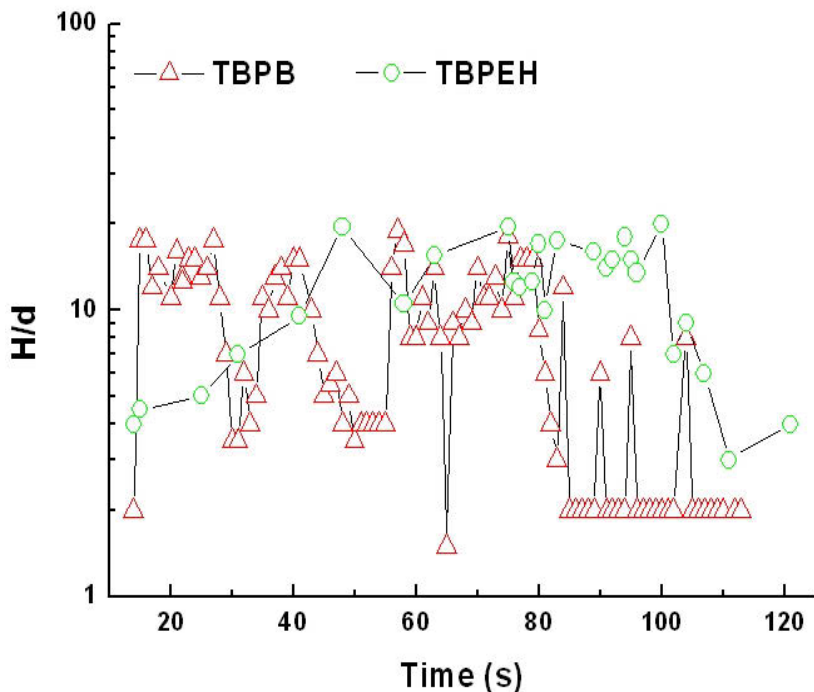


FIGURE 5.15: Instantaneous relative flame lengths vs. time of TBPB and TBPEH pool flame ($d = 0.059$ m)

increases up to a height of about 1.2 m. This process repeats itself with different time intervals over the entire burning time. An explanation for this effect can be given on the basis of the observed effect: At the beginning the total heat transfer processes from

the flame to the fuel is used for heating up the liquid fuel up to the temperature where the vaporisation starts in combination with the decomposition of the peroxide in the heated amount of fuel. It is not clear yet whether the decomposition starts immediately before or at the same time or shortly after the vaporisation and furthermore whether the decomposition starts in the liquid or in the gaseous phase. The flame height decreases some seconds later to a small height as in the beginning. Then this process starts again. The oscillation of pool flames have been studied by many authors in the last few decades [19]. The correlation between Strouhal number (Str) and fuel Froude number (Fr_f) indicates that the frequency f of oscillation varies according to the relationship $f \propto (Fr_f)^{-1/2}$ for hydrocarbon pool flames [70, 71]. It has been shown that $Str \sim 0.5$ is the most common approximation for hydrocarbon pool flames of various heat release rates [19]. Since the fuel Froude number of peroxide flame is 64 times of kerosene flame so if applicable the similar expression ($f \propto (Fr_f)^{-1/2}$) for TBPB ($d = 0.059$ m) also; it appears that the frequency of pulsation is almost 8 times smaller (so does the Strouhal number) than a corresponding flame of kerosene. The low frequency pulsation of TBPB pool flame is assigned as 'W' effect. The 'W' signifies the variation of relative flame length with time during the main burning period (Figs. 5.15 and 5.16). A similar pulsation can be observed if the fuel flow is controlled by means of a mechanical device e.g. a valve (pulse combustion in the process industries). A number of possible applications of the 'W' -effect including other organic peroxides are listed in [70, 71, 88, 89, 92, 101, 103, 104, 105, 106, 107].

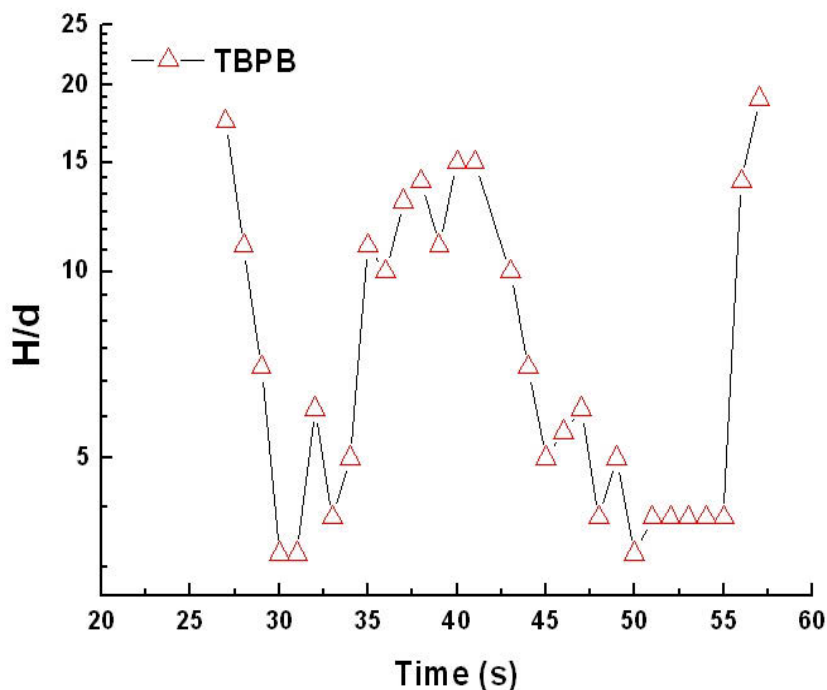


FIGURE 5.16: 'W' Effect in TBPB pool flame ($d = 0.059$ m) [70, 71, 103, 104, 105]

5.5 Flame temperature

5.5.1 Instantaneous flame temperature field

The instantaneous surface emission flame temperatures of pool fires ($d = 0.18$ m) measured by thermographic camera are shown in Fig. 5.17. The obtained thermograms (100 images during the main burning time) were analysed and the highest measured flame surface temperatures of the TBPB and TBPEH flames were determined. One important point to note is that the surface emission flame temperature of TBPB flame (~ 1400 K) is higher than of (~ 1200 K) TBPEH flame. The reason of lower surface emission temperature of TBPEH is the large amount of soot with a higher emissivity which continuously emit radiative energy to the surroundings therefore a lower flame temperature was recorded.

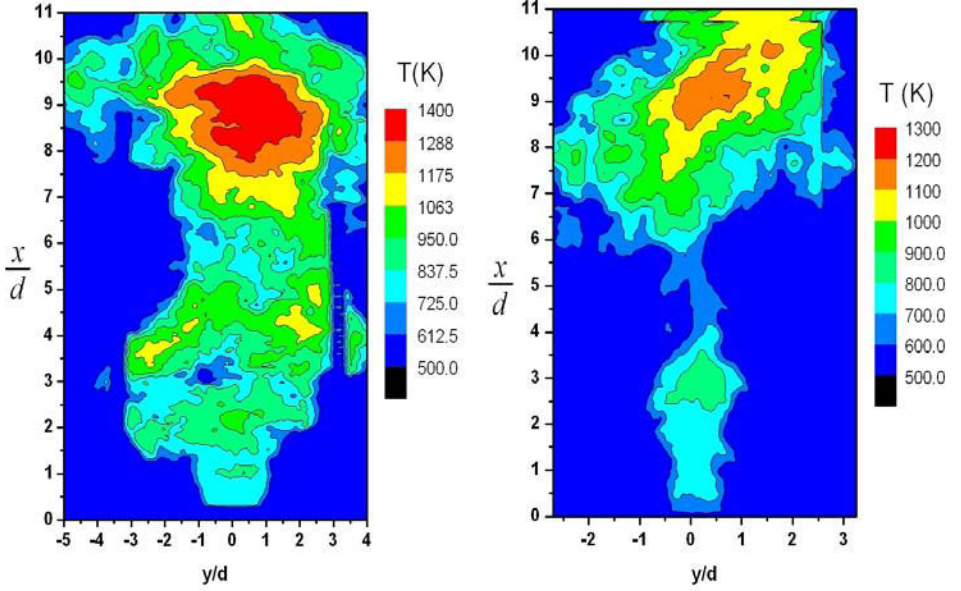


FIGURE 5.17: Instantaneous thermograms of TBPB (left) and TBPEH (right) pool fires ($d = 0.18$ m). "High Temperature" regions are in fact regions with high soot concentration. Numerical values must be interpreted with great care.

5.5.2 CFD prediction of time averaged flame surface emission temperature profile

In Fig. 5.18 the CFD predicted development of a TBPB flame with time can be seen. The flame lengths and areas of high flame temperature are increasing with time. A comparison between measured and CFD predicted time averaged radial temperature profiles at three axial locations are shown in Fig. 5.19. The time averaging is done by taking an average (eq. (5.12)) of a number ($N_T = 5$) of instantaneous thermographic images of flame during steady burning period.

$$\bar{T}_{i,j} = \frac{\sum_{i,j=1}^N T_{i,j}(t)}{N_T} \quad (5.12)$$

Since TBPB flame is pulsating steadily, a time is considered when the flame maintained steady burning. An integrated isotherm (of 65 different sections of instantaneous isotherms along the radius of the pool) is used for CFD predictions [72].

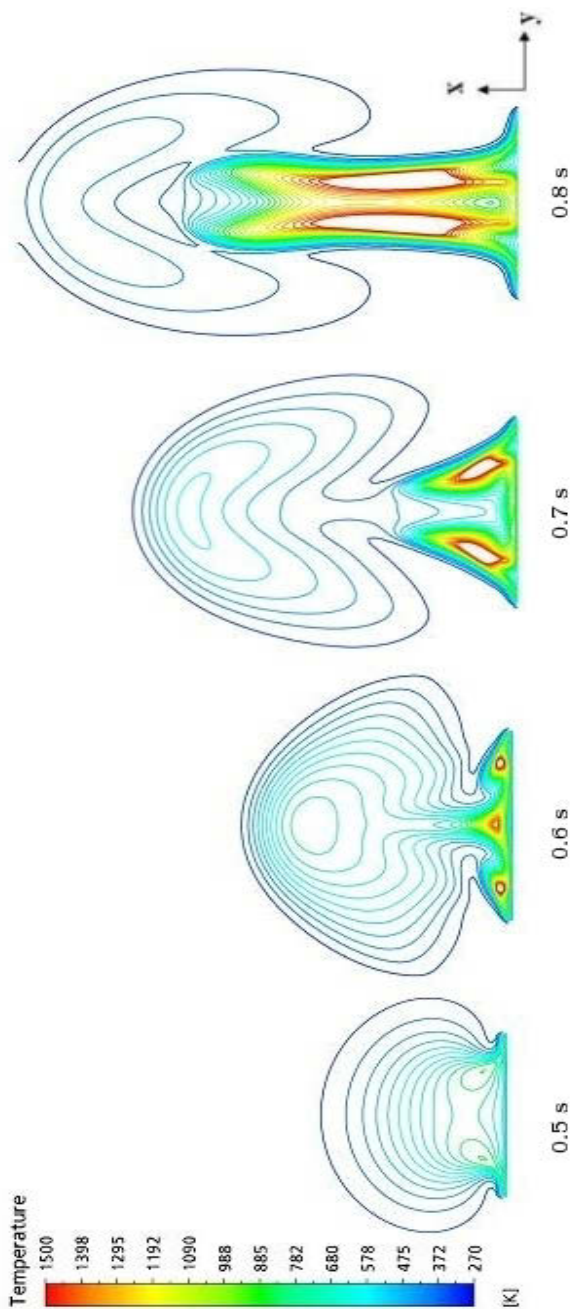


FIGURE 5.18: Flame development of TBPB in packaged fire test predicted by CFD ($d = 8$ m)

Thermocouple measured time averaged temperatures at the centre of the flame were found to be always 50–150 K lower than thermographic measurements whereas CFD predicted \bar{T} are quite good in agreement near to the pool surface and qualitatively comparable at the increased axial distances from the pool surface. A quantitative comparison is not possible due to the assumption of single step chemistry and the limitations of combustion model (eddy dissipation) for such peroxides are still unknown [66, 74].

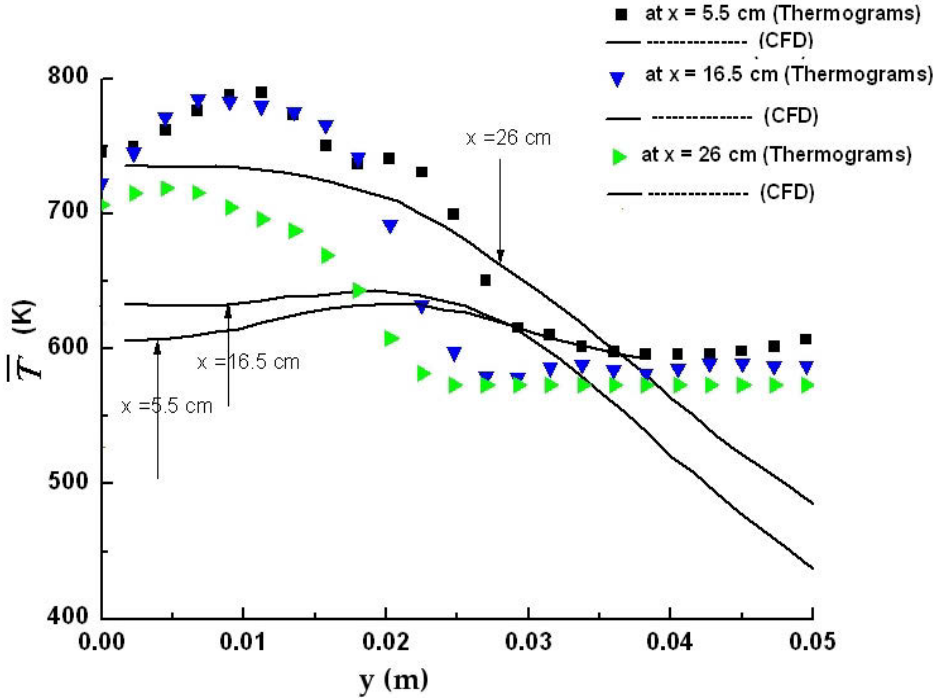


FIGURE 5.19: Measured and CFD predicted emission temperature \bar{T} profiles of TBPB pool fire ($d = 0.18$ m)

5.5.3 Time averaged flame temperature field

An averaging of thermographic images at different instant of time during the fully developed fire duration (eq. (5.12)) has been done in order to measure the distribution of time averaged flame temperatures at various spatial locations (Fig. 5.20) [60]. Due to continuous mixing and burning the \bar{T} and visible widths of hot areas of TBPEH flame (yellow area in Fig. 5.20) are higher and larger than the TBPB flame [63].

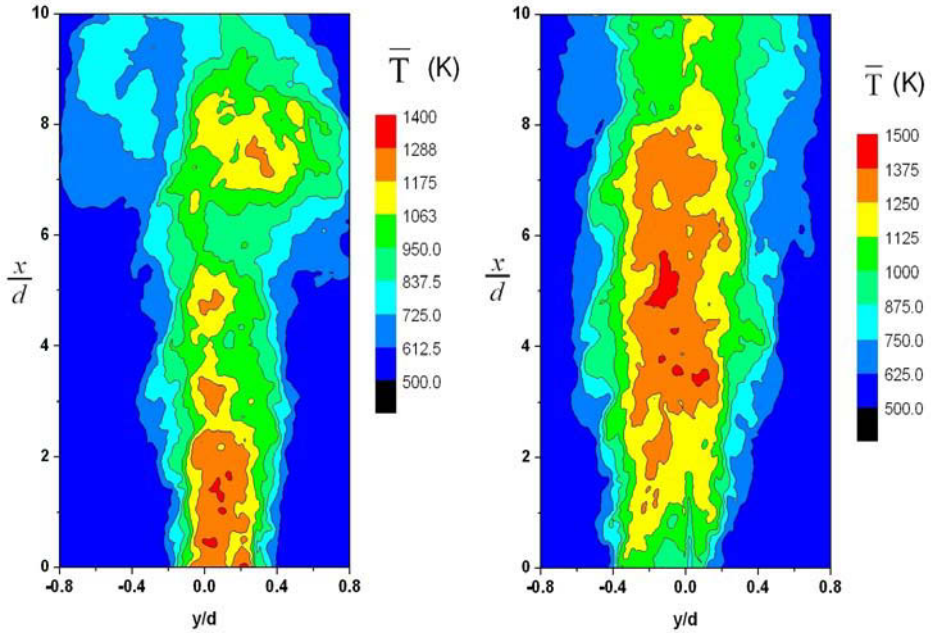


FIGURE 5.20: Time averaged thermograms $\bar{T}(x, y)$ of TBPB (left) and TBPEH (right) pool fires ($d = 3.4$ m)

In the Table 5.4 the time averaged flame surface emission temperature of various fuels and organic peroxides are given. $T_{\max} \geq 1700$ K ($d = 3.4$ m) was measured by the thermograms for both of the organic peroxides.

The major source of error in the measured \bar{T} is the uncertainty of flame emissivity ε_F in thermographic camera. Due to the lack of availability of experimental values of ε_F for organic peroxides, an assumed value of 0.9 was used for the temperature measurements. As far as the large pool fires of hydrocarbons are considered they are optically thick and therefore emissivity approaches to 1 [3, 4, 7, 14]. It has been shown that the emissivities of different large hydrocarbons pool fires ($d \geq 3$ m) range between 0.9 and 0.95 [60]. However, the value of ε_F can vary between 0.4 to 1 ($d < 1$ m). If consider this range the uncertainty in the present measurement ($\varepsilon_F = 0.8$ to 0.9, $d \geq 3$ m) can be in the range 40 K.

Fuel	Pool diameter (m)	Flame emission temperature (K)	Remark
LNG	8.5 to 15	1500	Measured with thermocouples
Gasoline	1 to 10	1240	Negligible temperature w.r.t. small diameter
JP-4	5.8	1200	Smoke obscured flame
Kerosene	30 to 80	1600	Measured with thermocouples
DTBP ^a	1 to 3.4	1480 to 1580	Measured with Thermographic camera
Kerosene ^a	1	1240	Measured with Thermographic camera
TBPB ^a	3.4	1400	Measured with Thermographic camera
TBPEH ^a	3.4	1500	Measured with Thermographic camera

Table 5.4: Time averaged flame emission temperature of hydrocarbons [81] and organic peroxides [62, 77]

^aMeasured at BAM.

5.5.4 Time averaged mass fraction of combustion products

For the large Damköhler number flows the non-premixed flame can be seen as an assembly of many small laminar premixed flames where the reaction takes place only within a thin sheet called as flamelet [50, 51, 54]. Therefore, the time averaged mass fraction of combustion products $\bar{\chi}_P$ of a laminar or turbulent diffusion flame can be written in the following linear form in eq. (5.13) (thermal and mass diffusivities of all species are assumed to be equal)[9].

$$\bar{\chi}_P = \frac{\bar{T} - T_a}{T_{ad} - T_a} \quad (5.13)$$

$\bar{\chi}_P$ gives information about the distribution of product formation (completeness of combustion). The adiabatic flame temperatures (in eq.(5.13)) for TBPB ($T_{ad} = 2295$ K) and TBPEH ($T_{ad} = 2285$ K) are determined with the enthalpy balance method as described in section 2.2.4 [74, 75]. The $\bar{\chi}_P$ of TBPEH flame approaches to a value of 0.6 (Fig. 5.20, Fig. 5.21). The reasons for the differences in the distribution of $\bar{\chi}_P$ referring to the temperature are described in section 5.5.3.

[66, 71, 76].

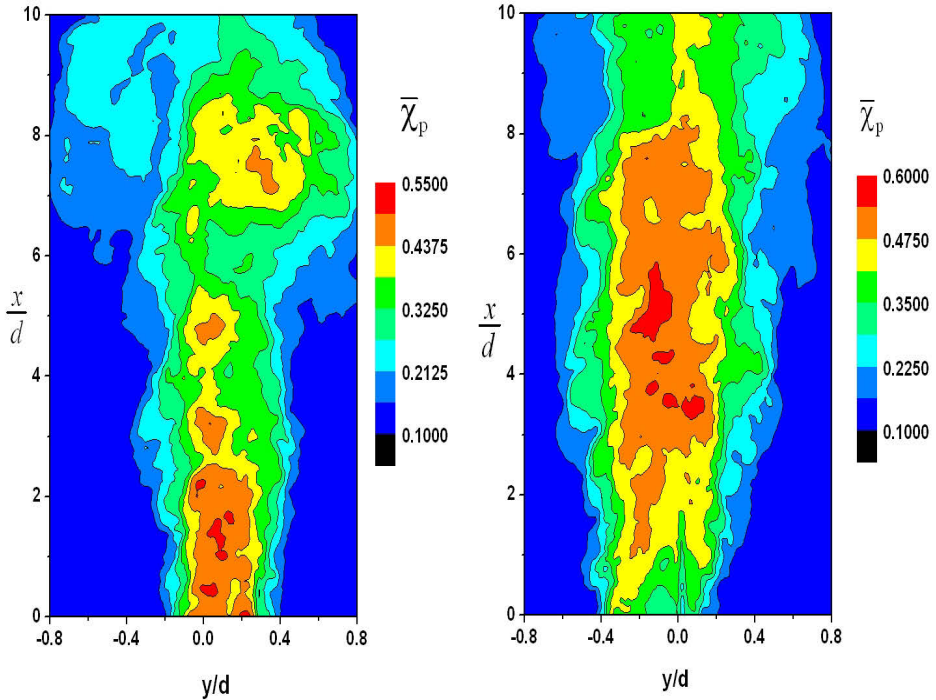


FIGURE 5.21: Time averaged $\bar{\chi}_p$ of TBPB and TBPEH pool fires ($d= 3.4$ m)

Considering the fact of uncertainties in the temperature measurements this derivation of $\bar{\chi}_p$ should only be interpreted as a qualitative estimation.

5.5.5 CFD prediction of the axial flame temperature profile

Additionally to the CFD predicted time averaged flame surface emission temperatures also the time averaged axial flame temperature profiles were determined using CFD. CFD predicted radial temperature profiles are not presented here because no experimental data are available.

The measurement of flame centreline temperature and flow velocity with the help of thermocouples and pressure probes at different axial locations of a fully developed turbulent diffusion flame has been carried out in the past for wide variety of hydrocarbon fuels [20]. An observation of three well defined zones i.e. flame, intermittent and plume were found on the basis of a scaling factor x' (see section 2.2.2.3). In Fig. 5.22 the

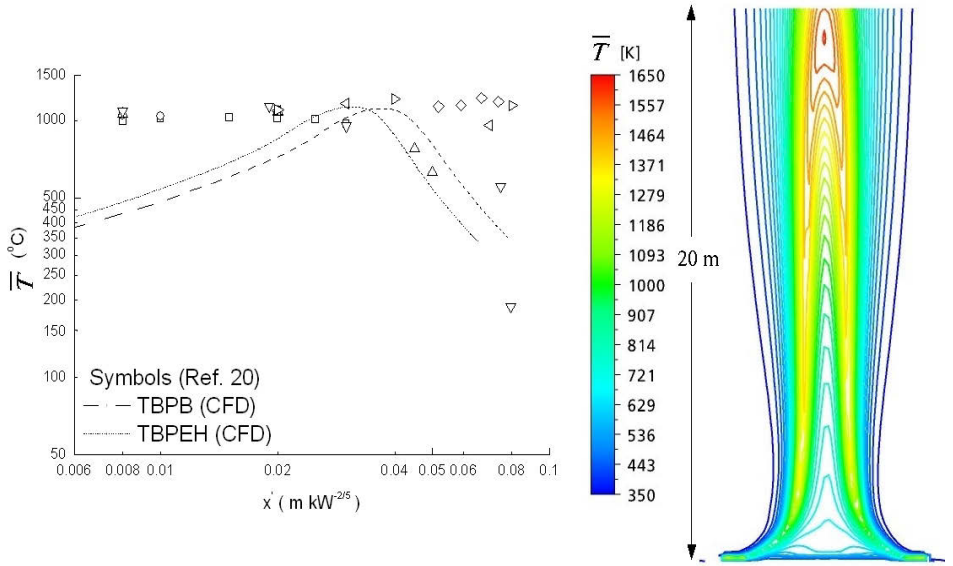


FIGURE 5.22: Measured and CFD predicted time averaged flame centreline temperature vs. x' (left) and CFD predicted isotherm of temperature of TBPEH flame (right)[20]

simulation results are compared with measured time averaged flame temperatures \bar{T} . Simulation underpredicts the \bar{T} near to the base of flame due to the stoichiometric combustion assumed (Fig. 5.22). It was also shown in [63, 77] that the location of chemical reaction zone for organic peroxide pool flames are not only just above the liquid pool rather it extends up to more than half of the total visible length of the flame. The expected length of flame zone has not been found with the present simulation. The isotherms of time averaged flame temperature \bar{T} predicted by simulation are shown on the right side of Fig. 5.22.

5.5.6 CFD prediction of the flame temperature in packaged fire test

In section 3.3 the descriptions of old large fire test were given. An equivalent pool of $d = 8$ m was used to approximate the packaged fire tests. After comparing with existing data on temperature of diffusion flames the uncorrected thermocouple measured data in the trough of the old large fire test (arrangement shown in Fig. 3.10(a)) were compared with the simulation. The initial phase of a wood crib fire time is approximately 5-6

minutes. During this time the temperature steadily increases until the maximum value is reached. In order to define this burning time in the CFD simulation it is assumed

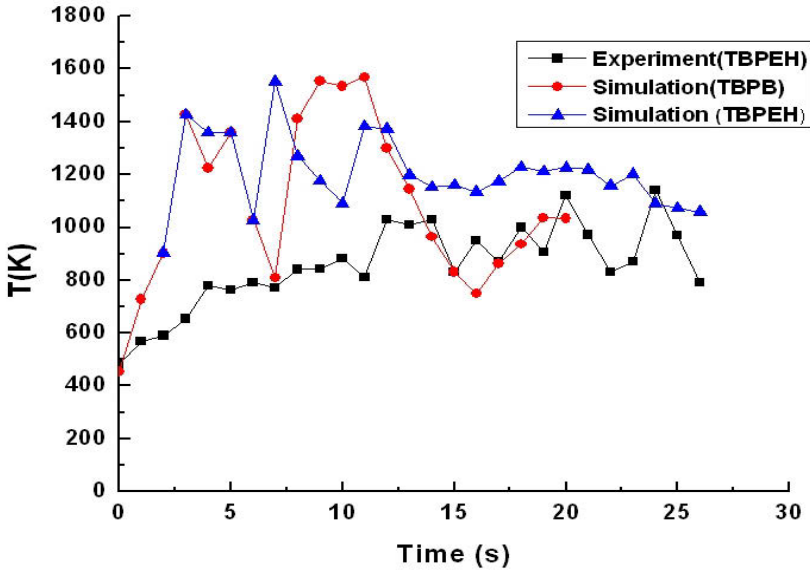
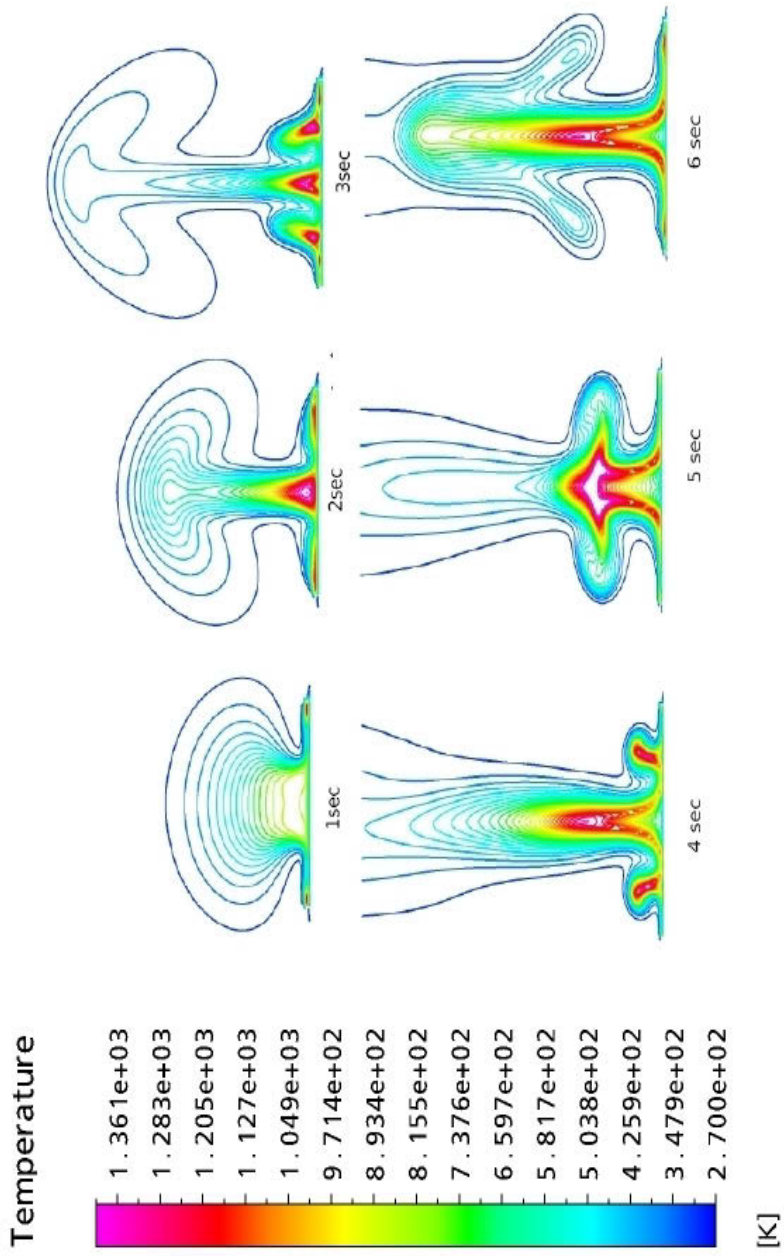


FIGURE 5.23: Measured and CFD predicted instantaneous temperature T in large packaged fire of TBPEH ($d=8$ m)

here that the initial 20 seconds of the simulation (when the flame reaches steady burning condition) are enough to let the temperature rise like in the experiment. For a real fire this time was between 8-10 minutes. The measured and CFD predicted temperature for both peroxides is shown in Fig. 5.23. CFD predicted temperatures for TBPB are higher during the initial few seconds and reaches values > 1500 K. TBPEH flame reaches steady burning conditions ($t > 10$ s) with very small fluctuations. As was indicated in section 3.3.2 that the maximum temperature measured for both peroxide fires were about 1173-1223 K which is in good agreement with the CFD predicted value for TBPEH fires (1200-1300 K).

In Figs. 5.24 and 5.25 a time dependent flame development of TBPB and TBPEH are shown. TBPEH shows very different structures to TBPB. The predicted development of the isotherms for TBPB are comparable with the small pool fire simulation at $d = 0.18$ m (section 5.5.2). At the same time it also exhibits the larger width than TBPB which was also experimentally observed.

FIGURE 5.24: Flame development of TBPB in packaged fire test, predicted by CFD ($d = 8$ m)

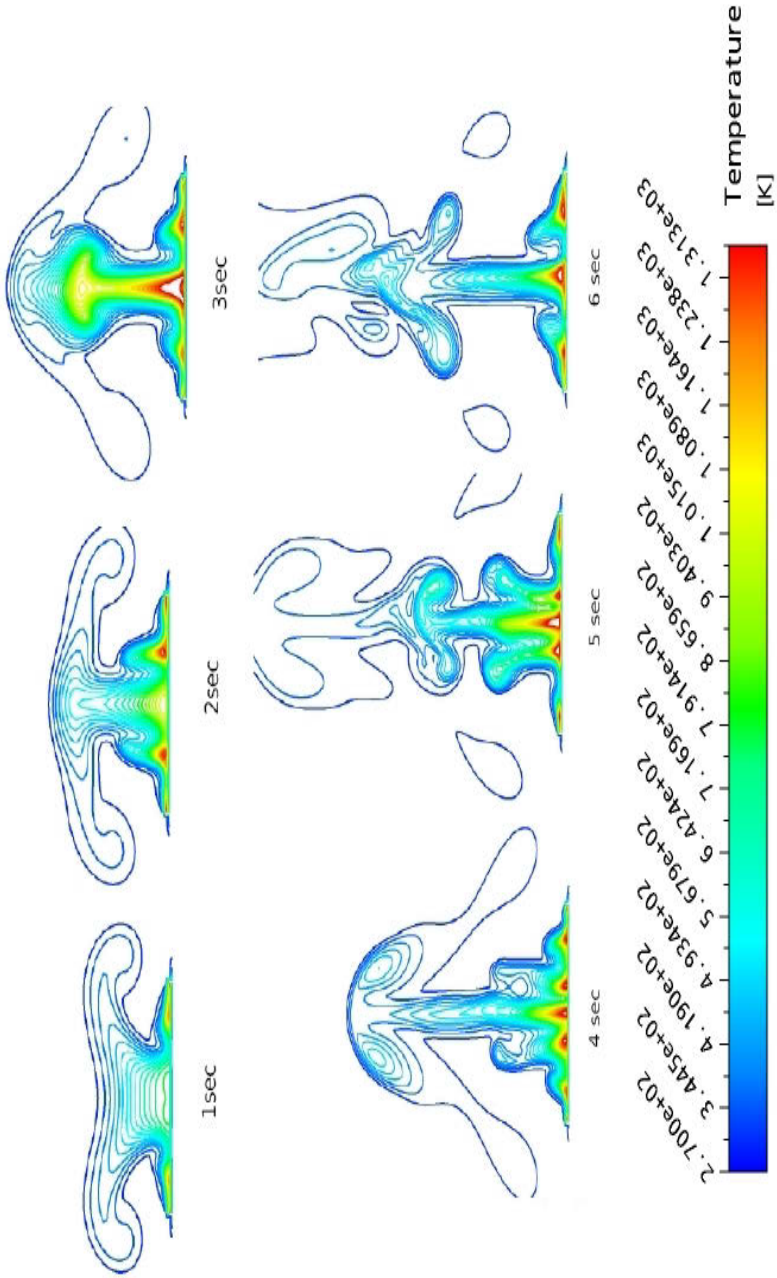


FIGURE 5.25: Flame development of TBPEH in packaged fire test predicted by CFD ($d = 8$ m)

5.6 Flow velocity of flame gases

Velocity of hot gases inside a large pool fire were measured by bi-directional pressure probes and PIV (Particle Image Velocimetry) methods [20, 78]. Since the mass burning rate remains constant at larger diameters so the flow velocity increases in fully developed pool fires can reach to a maximum value i.e. the pool size does not affect the velocity of flow [14]. In this study a method is presented to estimate the flow velocity of gases by observing the movement of large and small eddies in thermograms with known time interval Δt . The estimation is not exact due to limited spatial and time resolving capacity of a thermographic image which contains the information of temperature T e.g. of a large flame ($d = 3.4$ m, $H = 30$ m) in 240×110 pixel elements (Fig. 5.26) and integrates signal from the depth of the flame.

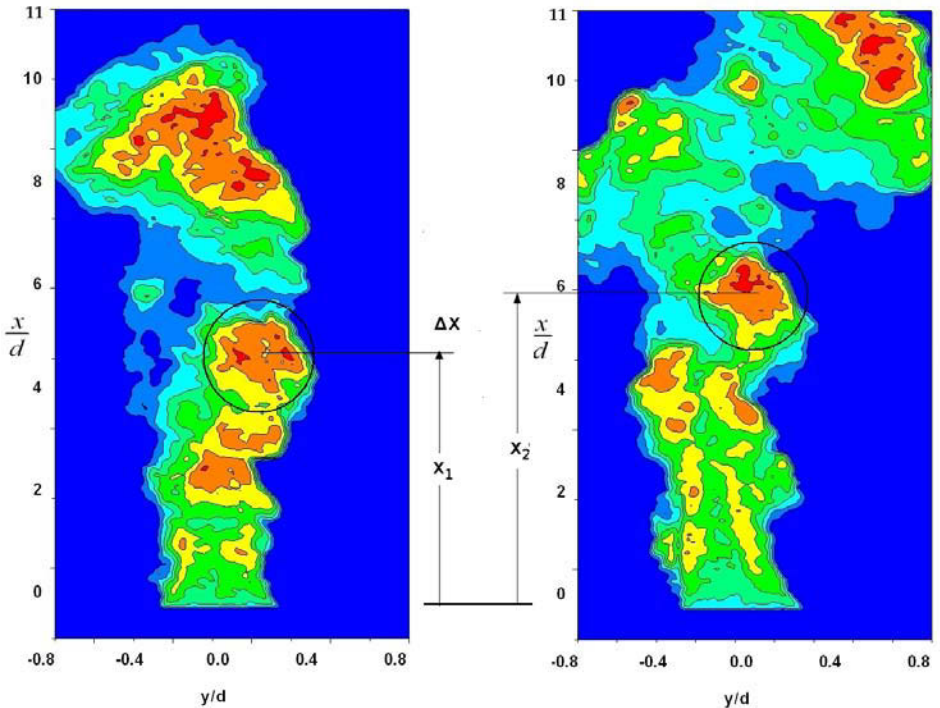


FIGURE 5.26: A pair of instantaneous thermograms taken with a time delay of $\Delta t = 0.019$ s showing the displacement Δx of the centre of small vortices in a TBFB flame

The displacement Δx of a centre of a large eddy (approximately area of constant temperature) in axial direction in a time interval $\Delta t = 0.019$ s is shown in Fig. 5.25. Since the measurements were done under negligible cross wind conditions so no corrections for cross wind effects are necessary (see section 3.2).

$$u = \frac{x_2 - x_1}{t_2 - t_1} = \frac{\Delta x}{\Delta t} \quad (5.14)$$

The initial two data points of TBPB and TBPEH are shown in left of Fig. 5.26 where the influence of large and small scale eddies can be seen between measured and CFD predicted values. When considers the smallest eddy in present thermogram i.e. data points for TBPB and TBPEH it (eq. (5.14)) agrees much better than the larger ones. Since a thermogram contains only 2-D informations the flow velocity predicted completely ignores the component normal to the image. That might be one of the reasons why the velocities determined by thermograms are higher. Probably the spatial and time resolution are not sufficiently high therefore the flow velocities determined from eq. (5.14) are too high [79]. Because of the slow repetition rate of the measurement it is not easy to follow individual structures as seen from Fig. 5.26. Most structures can not be identified anymore in the second image.

5.6.1 CFD simulation

By using CFD predicted axial flame temperature and axial flow velocities the modified centreline Froude number was calculated as described in [49]. According to [49] for different heat release rates the centre line Froude number $Fr \approx 2$ is found for inviscid flows. From the large scale fires of packaged TBPB and TBPEH a \dot{Q}^* are calculated from eq. (2.8). As can be seen from Fig. 5.27 also a modified centre line Froude number of 2 follows for the two peroxide flames as for hydrocarbon flames. This is a quality criterion for the simulation results in this study. The x^* and Fr in Fig. 5.27 are calculated with eqs. (5.15) and (5.16).

$$x^* = \dot{Q}^{\frac{2}{5}} d \quad (5.15)$$

$$Fr = \frac{u^2}{\frac{(T - T_a)}{T_a} g x} \quad (5.16)$$

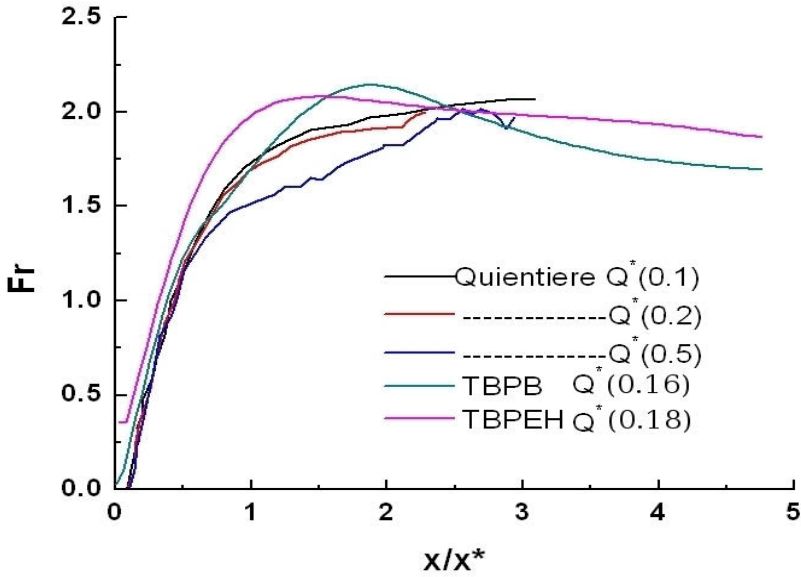


FIGURE 5.27: Fr vs. non dimensional axial coordinate along the flame

The velocity of flame gases (u) predicted by simulation is good in agreement with the existing experimental data for hydrocarbon flames in the literature (Fig. 5.28) [49]. Because the experimental determined gas velocities of the organic peroxide flames are too high (see chapter 5.6) also the CFD predicted flow velocities for peroxide flames should be in much better agreement with those shown in Fig. 5.28 on basis of better resolution of the thermograms.

The CFD predicted radial velocity profiles at different axial distances in a fully developed flame along the length of flame can be seen in Figs. 5.29 and 5.30.

The velocity field is good in agreement with the previously reported results [49] shown in Figs. 5.31, 5.32, 5.33. To get a better understanding of the velocity field a comparison of the velocities measured by McCaffrey [49] in three different locations of all the three zones has been done. In Fig. 5.31, 5.32 and 5.33 are included the CFD predicted velocity profiles of TBPB and TBPEH-flames.

On abscissa the radial distance is normalised by r_1^* . Since the plume zone does not show appreciable difference in velocity distribution due to buoyant forces so the abscissa r/x_1 was chosen as described in [80]. This normalisation is purely based on the empirical

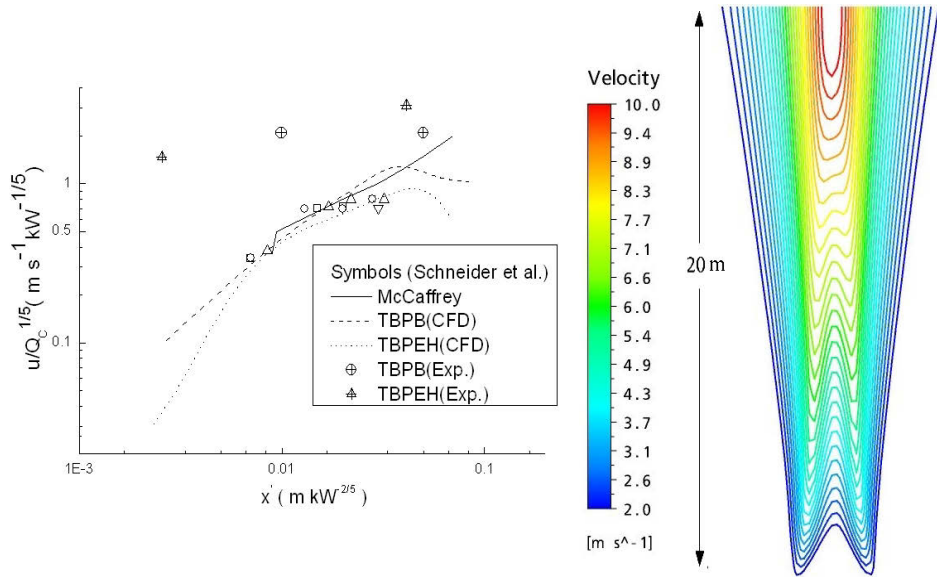


FIGURE 5.28: Time averaged measured and CFD predicted flame centreline velocity u vs. x' (left) and contour plot of velocity field of TBPEH flame (right)

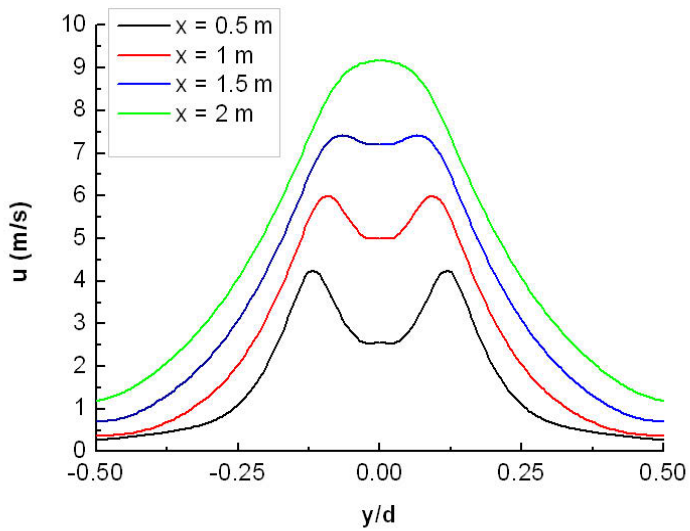


FIGURE 5.29: CFD predicted radial velocity profiles at different axial distances in a fully developed TBPB pool fire ($d = 1 \text{ m}$)

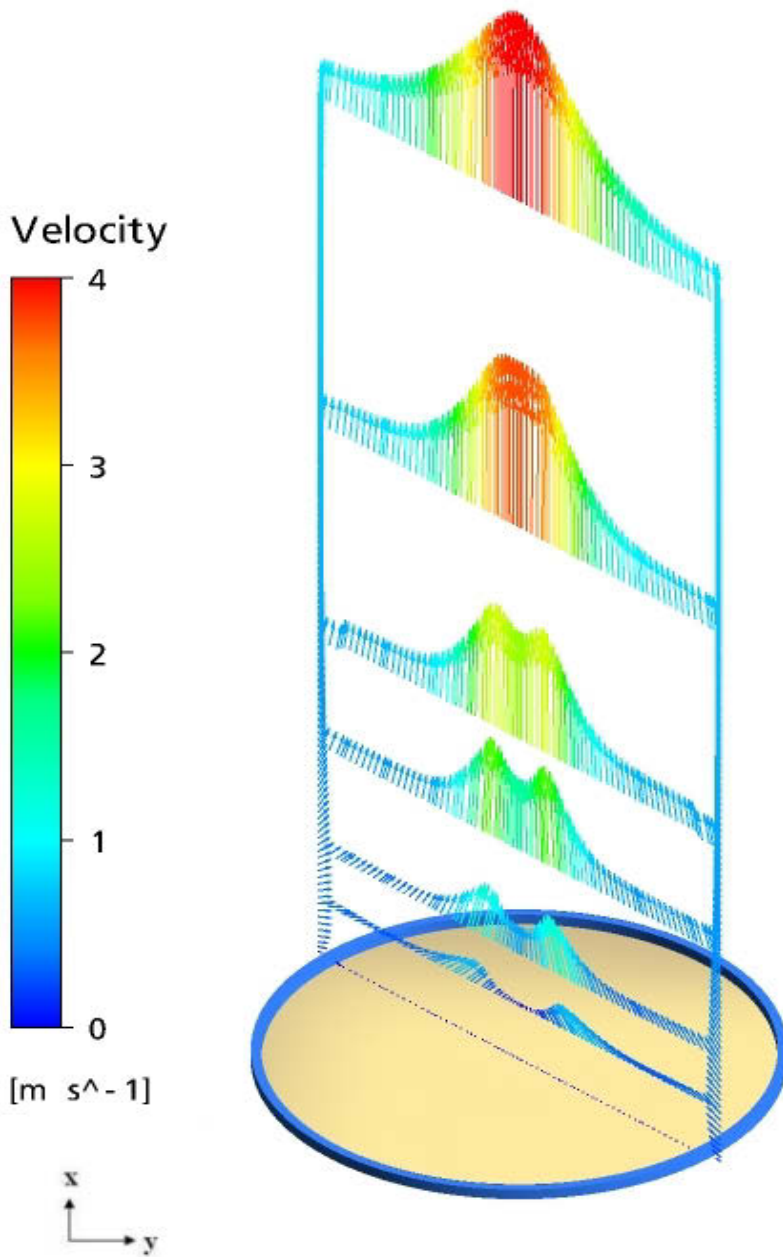


FIGURE 5.30: CFD predicted radial velocity profiles at different axial distances in a fully developed TBPB pool fire ($d = 0.18$ m)

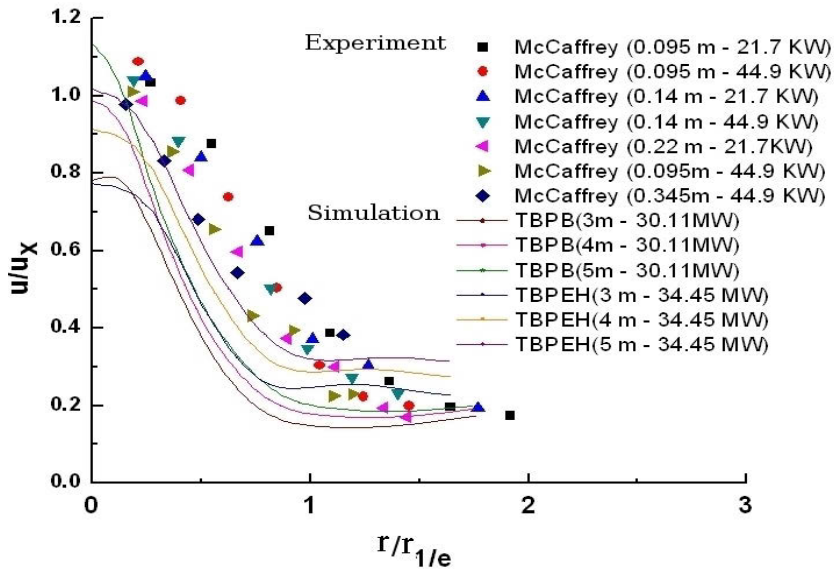


FIGURE 5.31: Relative flow velocities of flame gases in clear flame zone

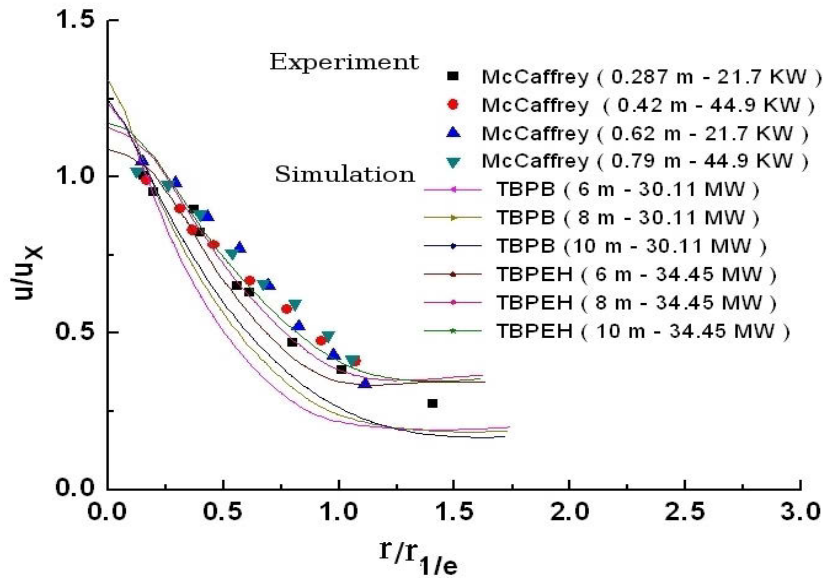


FIGURE 5.32: Relative flow velocities of flame gases in pulsation zone

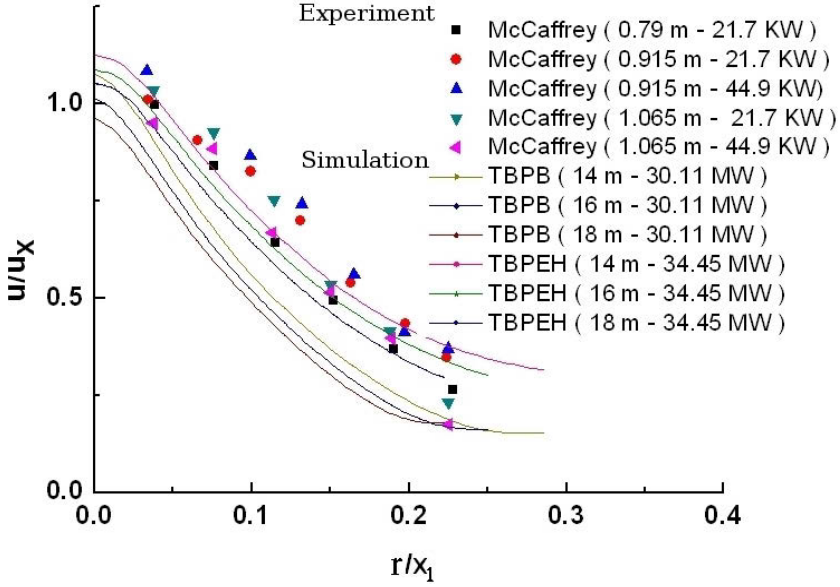


FIGURE 5.33: Relative flow velocities of flame gases in three different locations (x_1) in plume zone

relationship developed on the basis of experimental data. The deviations in the case of peroxide fires in clear flame zone is relatively large because the present sub-model of combustion does not take into account the elementary reactions and therefore the flow velocities are underpredicted. In case of TBPEH fire the CFD predicted velocity in intermittent and plume zones give good agreement with the hydrocarbon fire measurements [80].

5.7 Flame irradiance

The time averaged irradiance \overline{E} can be calculated by surface emissive power \overline{SEP} with the following equations:

$$\overline{E} = \varphi_{F,R} \tau \overline{SEP} \quad (5.17)$$

$$\overline{SEP} = \sigma \varepsilon_F (\overline{T}_{CFD}^4 - T_a^4) \quad (5.18)$$

The measured irradiances E versus time of nearest placed three radiometers (R_1 , R_2 , and R_3) for TBPEH and TBPB pool fire are shown in Figs. 5.34 and 5.35 respectively.

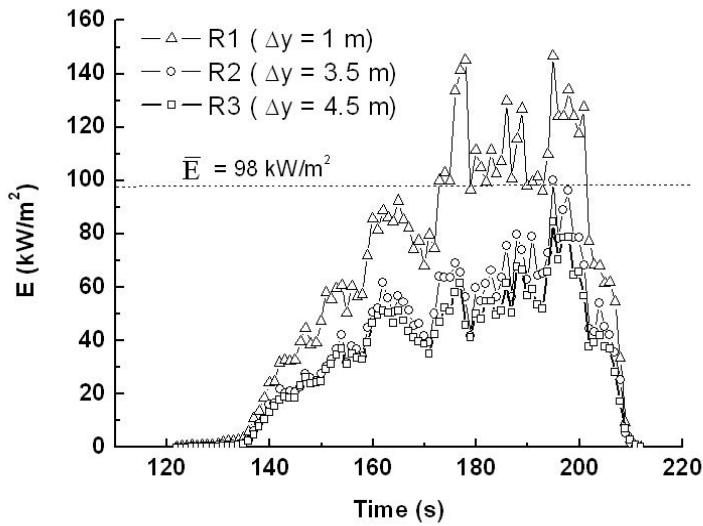


FIGURE 5.34: Instantaneous irradiance vs. time at different distances for TBPEH pool fire ($d = 3.4$ m)

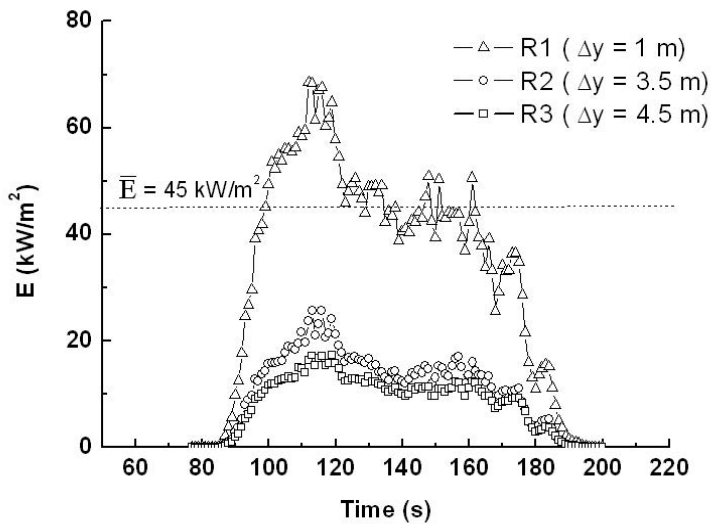


FIGURE 5.35: Instantaneous irradiance vs. time at different distances for TBPB pool fire ($d = 3.4$ m)

The time shown on abscissa is the total time from the point of start of sensors. The measured values of R_1 were used to obtain the time averaged irradiances \bar{E} . The peaks in the curves of R_1 coming from the natural fluctuation of the flame.

In case of TBPB (Fig. 5.35) the maximum irradiance measured by R_1 is almost half ($\sim 45 \text{ kW/m}^2$) of the TBPEH. The reason for the lower value for TBPB is the pulsation as shown in Fig. 5.20.

The time averaged irradiances $\bar{E}(\Delta y/d)$ as a function of non dimensional horizontal distance from pool rim is shown in Fig. 5.36. For predicting $\bar{E}(\Delta y/d)$ with CFD time averaged flame surface temperature \bar{T}_{CFD} in eqs. (5.17) and (5.18) is chosen:

$$\bar{E} = \varphi_{F,R} \sigma \tau \varepsilon_F (\bar{T}_{CFD}^4 - T_a^4) \quad (5.19)$$

where \bar{E} is the time averaged irradiance in W/m^2 at a certain distance from fire. σ is the Stefan Boltzmann constant ($5.67 \times 10^{-8} \text{ W/(m}^2\text{K}^4)$); τ is the atmospheric transmissivity assumed to be 1; ε_F is the emissivity assumed as 0.9 as most of the hydrocarbon pool fires at $d \geq 3 \text{ m}$ are optically thick [4, 7, 14, 60]. \bar{T}_{CFD} and T_a are average flame temperature and ambient temperature in Kelvin.

The view factor $\varphi_{F,R}$ from Flame (F) to Receiver (R) is given by the following equation [91]

$$\varphi_{F,R} = \frac{1}{2\pi} \left(\frac{B}{\sqrt{1+B^2}} \tan^{-1} \frac{C}{\sqrt{1+B^2}} + \frac{C}{\sqrt{1+C^2}} \tan^{-1} \frac{B}{\sqrt{1+C^2}} \right) \quad (5.20)$$

where B and C are defined as the ratio of flame width (b) to distance between flame and receiver (Δy) and flame height (\bar{H}) to distance between flame and receiver (Δy) respectively for approximation of flame as a rectangular surface [81].

The radiometers were able to measure the irradiance close to the flame. In the case of TBPEH flame the irradiance predictions with CFD simulation were not carried out. The CFD simulation for TBPB shows a good agreement with the measurements (Fig. 5.36).

If one follows the criterion described in [82] i.e. NFPA (National Fire Protection Agency) 59A Standard and the Federal Regulation, 49 CFR Part 193, the safety distance (also

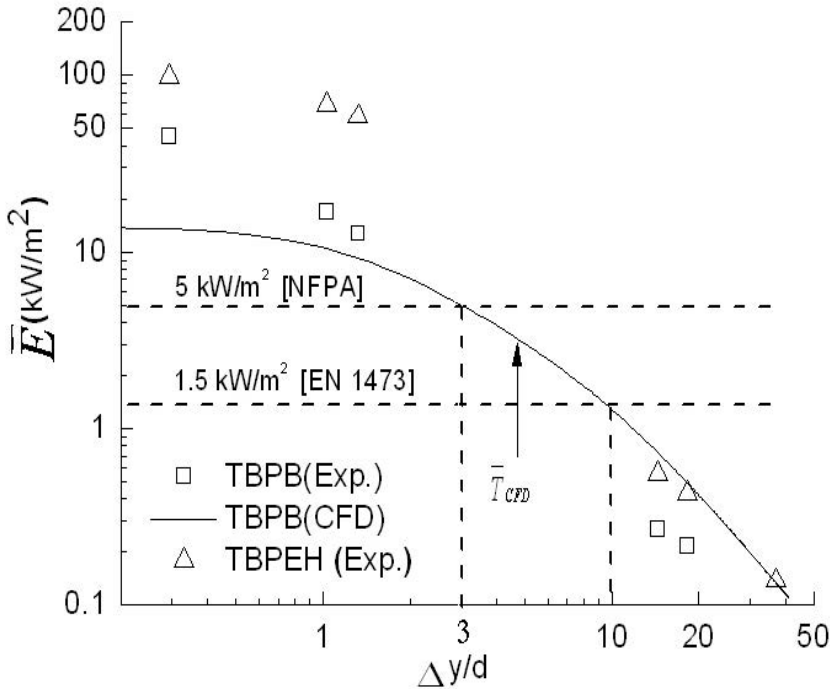


FIGURE 5.36: Irradiance vs. non dimensional distance from pool rim ($\Delta y/d$) of TBPB flame ($d = 3.4$ m) ($\bar{T}_{CFD} = 1012$ K)

given in Fig. 5.36) for organic peroxide pool fires can be predicted when \bar{T}_{CFD} is considered for calculation [84]. The criteria of 5 kW/m^2 is based on the phenomenon of skin burn caused by radiant heat exposure whereas EN 1473 recommends this limit to be 1.5 kW/m^2 [82, 83].

The reasons given for the uncertainties in the measurement of mass burning rates, flame lengths and flame temperatures are equally accountable for the uncertainties in the measurement of irradiances. The uncertainties in the present measurement of irradiances \bar{E} in the large pool fires are in the range of $\pm 23\%$ to $\pm 40\%$ [96, 98, 100]. The uncertainty analysis on the pool fires of diesel, JP-8 and jet fuel in [98] concludes that the combined convective and radiative environment in a large pool fire introduce errors in the measurement. The realistic determination of convective heat transfer coefficient and the sensitivities of radiometers to such convective and radiative atmosphere are the key issues in the correct measurement of irradiances.

5.7.1 CFD prediction of irradiance in a fire test of packaged fuel

The measured irradiance \overline{E} in all horizontal directions with calibrated radiometers in the large packaged fire test and the CFD predicted values are shown in Fig. 5.37. More details about the radiometer specification and location could be found in section 3.3.

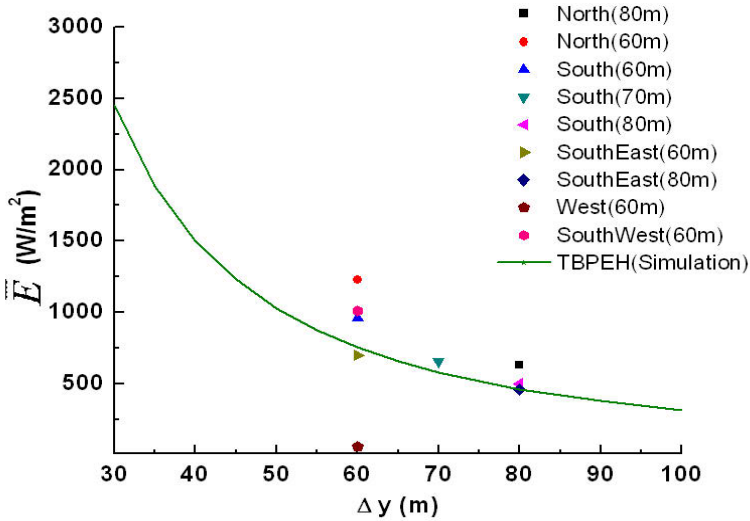


FIGURE 5.37: Time averaged measured and CFD predicted irradiance in fire test of packaged fuel ($\overline{T}_{\text{CFD}} = 1229$ K)

Data shown by symbols in Fig. 5.37 are data directly obtained from the radiometer measurements. The line is the result of eq. (5.19). The calculated value of \overline{E} agree well with the measurements [80].

5.8 Surface emissive power

5.8.1 Prediction of surface emissive power from thermograms and from CFD

The *SEP* is determined by evaluation of the thermograms. The experimental determination of the local distribution of surface emissive power $SEP(x, y)$ is done by using the

local temperature distribution $T(x, y)$ from thermograms (Chapter 5.5.3) [85]. Based on experimental data obtained from thermograms of TBPB and TBPEH the $SEP_{i,j}$ of flame is calculated with the help of eq. (5.21) where $T_{i,j}$ represents the temperature at a pixel element i, j . The selection of emissivity ($\varepsilon_F = 0.9$) was based on the facts reported in [60] for optically thick hydrocarbon pool fires. Because of a lack of experimental data on emissivity of pool fire of organic peroxides a selection (based on the data of emissivity of hydrocarbon fires and packaged material fires of organic peroxides) is made as an approximation for organic peroxide pool fires. The SEP of a pixel element can be given by:

$$SEP_{i,j} = \varepsilon_F \sigma T_{i,j}^4 \quad (5.21)$$

The time averaged surface emissive power of a pixel element \overline{SEP} can be calculated by

$$\overline{SEP}_{i,j} = \frac{\sum_1^{N_T} SEP_{i,j}(t)}{N_T} \quad (5.22)$$

The average surface emissive power SEP of flame can be written as

$$\overline{SEP}(d) \equiv \langle \overline{SEP}_{i,j}(d) \rangle = \frac{\sum_i \sum_j \overline{SEP}_{i,j}(d) a_x}{\sum_i \sum_j a_x} \quad (5.23)$$

Only the pixels with temperatures $T_{i,j} > 600$ K are considered for determination of SEP because the lower temperatures do not make a significant contribution to the thermal radiation of a pool fire. In eq. (5.23) the area a_x of a pixel-matrix element is used to take into account the size and current position of a pixel in the vertical and horizontal field.

During the combustion of hydrocarbons e.g. kerosene, a considerable amount of soot formed as a result of large residence time of fuel vapours which leads to incomplete combustion. The cold black soot obscured the flame surface and thus caused the heat to dissipate and therefore the surface temperature of the flame is decreased. As a consequence a lower flame surface temperature and lower SEP has been measured by the thermographic camera.

On the contrary to this TBPB and TBPEH show fast mixing, small residence time of fuel vapour and therefore ensure more complete combustion. The soot produced in the case of TBPB and TBPEH pool fires continuously receive the heat from the fast combustion

and therefore caused the luminosity of the flame until it reaches its maximum visible length and then becomes fully buoyant.

The measured and CFD predicted values of \overline{SEP} for various hydrocarbons and organic peroxides for different diameters are given in Table 5.5. The CFD predicted values represent \overline{SEP} of an averaged flame surface obtained after integration of 65 different isotherms along the radial direction of the pool [85]. \overline{SEP} of all hydrocarbon pool fires ($d = 1$ m to 80 m) are measured between 280 kW/m² and 30 kW/m² whereas the organic peroxides ($d = 1$ m to 3.4 m) show this range to lie between 180 kW/m² to 330 kW/m².

Fuel	Pool diameter d (m)	SEP (kW/m ²)	Remark
LNG	8.5 to 15	210 to 280	Narrow angle radiometers
Gasoline	1 to 10	130 (max) to 60	-
Kerosene	30 to 80	25 to 10 (average)	Wide angle radiometers
DTBP ^a	1 to 3.4	130 to 260	Thermographic camera
JP-5	30	30	-
TBPB ^a	3.4	196	Thermographic camera
TBPEH ^a	3.4	258	Thermographic camera

Table 5.5: Measured \overline{SEP} of hydrocarbons and organic peroxide pool fires [11, 62, 87]

^aMeasured at BAM.

The interesting thing is to note that TBPB shows lower \overline{SEP} than DTBP and TBPEH due to the fact of 'W' effect. The time averaged flame emission temperature of DTBP [88] is higher than for TBPEH and TBPB. The flame surface of DTBP is smaller than of TBPEH and TBPB. All these facts explained that the $\overline{SEP}_{DTBP} > \overline{SEP}_{TBPB, TBPEH}$. CFD simulation overpredicts the \overline{SEP} of TBPB and TBPEH pool fires due to enhanced mixing (Fig. 5.38).

A number of models based on various assumptions have been developed and tested for predicting the average surface emissive power. Recently a model proposed by Fay [9] assumes the flame as a grey gas with $\gamma\sigma T_F^4$ of 563 kW/m² (based on LNG, $d = 35$ m test, $T_F = 2300$ K, $\gamma = 0.36$) and an optical length of $\kappa\overline{H}$. Now the SEP can be calculated

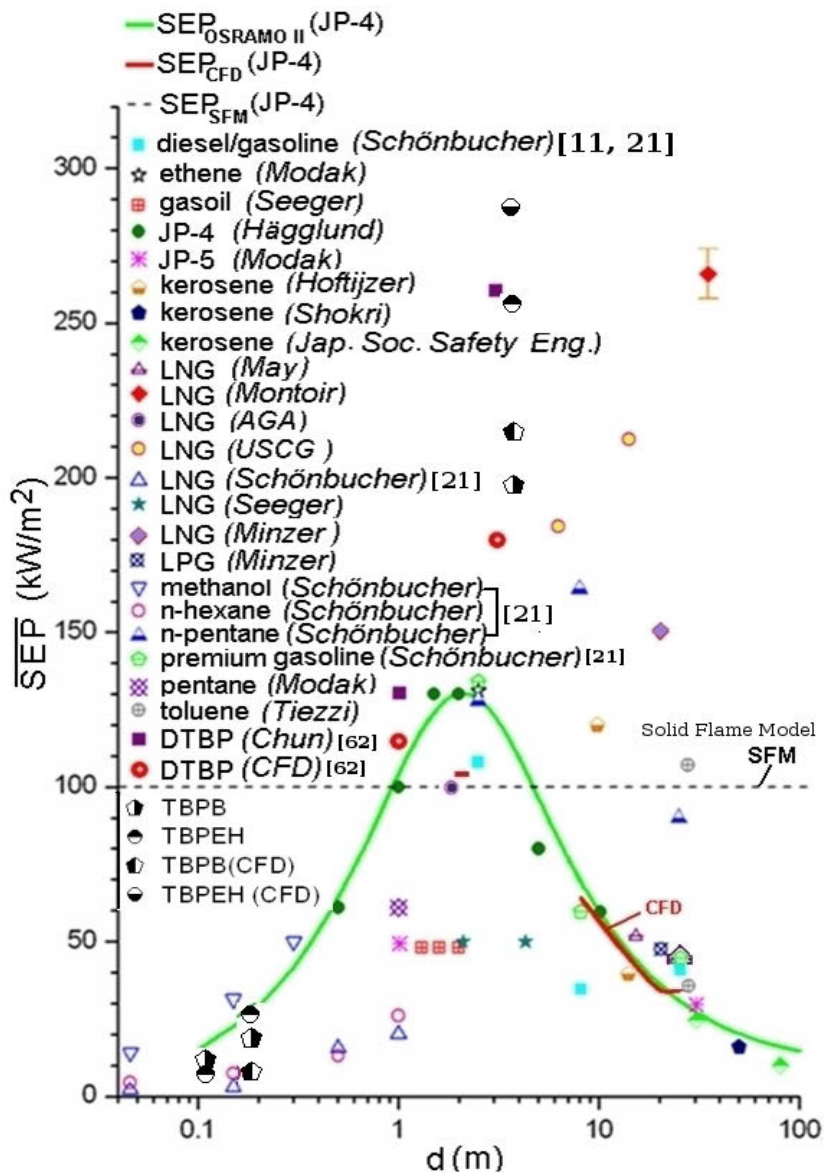


FIGURE 5.38: Measured and CFD predicted \overline{SEP} of hydrocarbons and organic peroxide pool fires [11, 21, 85, 87]

by using the following equation

$$\frac{\langle SEP \rangle}{\gamma \sigma T_F^4} = \frac{1}{\kappa \bar{H}} (1 - (1 + \kappa \bar{H}) \exp(-\kappa \bar{H})) \quad (5.24)$$

with $\kappa = 0.0233 \text{ 1/m}$ [9], for TBPB the $\bar{H} = 31 \text{ m}$ and for TBPEH $\bar{H} = 26 \text{ m}$. Under such assumptions an excellent agreement was found (Fig. 5.39) between the Fays model and those calculated with the eq. (5.24) with experimental values of \bar{H} , which is the only variable in eq. (5.24) [77].

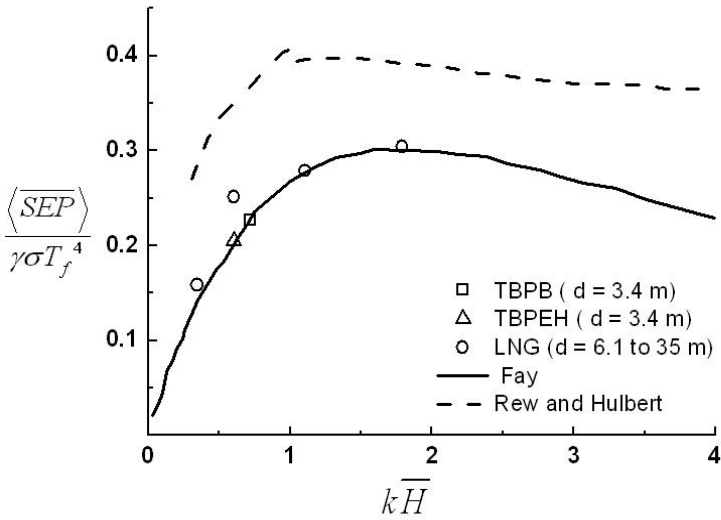


FIGURE 5.39: $\frac{\langle SEP \rangle}{\gamma \sigma T_F^4}$ of LNG and organic peroxide pool fires as a function $\kappa \bar{H}$

5.8.2 Soot mass fraction

Soot formation in large hydrocarbon pool fires influences the flame characteristics to a large extent. Modelling of continuous production and oxidation of soot particles in the present simulation has been done with the help of Magnussen soot model.

In Fig. 5.40 the dependence of soot mass fraction on x' for TBPB and TBPEH is shown. A pulsation effect can be seen for TBPB whereas TBPEH shows normal burning with

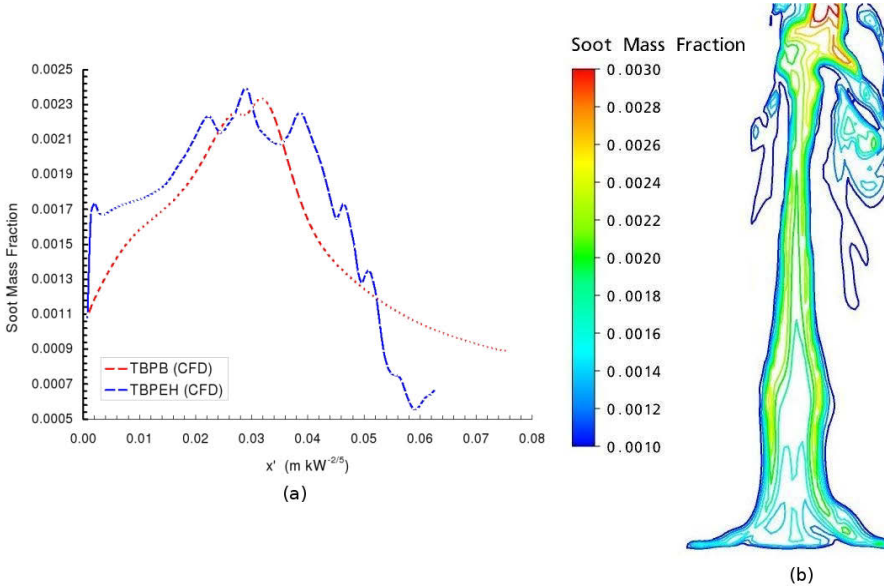


FIGURE 5.40: (a) CFD predicted soot mass fraction vs. x' in TBPB and TBPEH pool fire ($d = 3.4$ m); (b) CFD predicted contours of soot mass fraction of a TBPEH pool fire ($d = 3.4$ m)

natural frequency of fluctuation [84]. The reasons for the smaller soot mass fraction distribution is also caused by the 'W' -effect in the TBPB flame.

5.9 Validation of CFD simulation

Due to uncontrolled field conditions, limitation of measuring instruments and complicated physics, the measurement of pool fire characteristics are greatly influenced by a number of parameters. The same is also valid for CFD simulations where the lack of quality input parameters for turbulence, combustion and radiation models may introduce significant errors and uncertainties in predictions. The uncertainties in CFD simulation are analysed according to [99] and will be described as follows.

The magnitude of errors and uncertainties in the predictions of simulation largely depends on the accuracy and confidence assured in experimental results. Oberkampf et al. [99] give the quantitative way to estimate the error and uncertainties in computational results of a turbulent buoyant plume of helium. The method called 'Global Metrics' is

based on the error $F(x)$ associated with the each predicted size x written as [85, 99]

$$F(x) = y_m(x) - \bar{y}_e(x) \quad (5.25)$$

where $y_m(x)$ is the mean calculated value and $\bar{y}_e(x)$ is the mean experimental value.

The error in the field with 90% probability is given by

$$\left(F(x) - t_{0.05,t} \frac{S(x)}{\sqrt{n}}, \quad F(x) + t_{0.05,t} \frac{S(x)}{\sqrt{n}} \right) \quad (5.26)$$

$S(x)$ is the standard deviation and the distribution of t depends on the number of degree of freedom $f = n-1$ for n of x

$$\left| \frac{F}{\bar{y}_e} \right|_{\text{avg}} = \left(\frac{1}{x_u - x_l} \right) \int_{x_l}^{x_u} \left| \frac{y_m(x) - \bar{y}_e(x)}{\bar{y}_e(x)} \right| dx \quad (5.27)$$

$$\left| \frac{F}{\bar{y}_e} \right|_{\text{max}} = \max_{x_l \leq x \leq x_u} \left| \frac{y_m(x) - \bar{y}_e(x)}{\bar{y}_e(x)} \right| \quad (5.28)$$

where the maximum value of size x is x_u and the minimum is x_l . The average and maximum relative confidence indicator (CI) are given by [99]:

$$\left| \frac{CI}{\bar{y}_e} \right|_{\text{avg}} = \frac{t_{0.05\nu}}{(x_u - x_l)\sqrt{n}} \int_{x_l}^{x_u} \left| \frac{s(x)}{\bar{y}_e(x)} \right| dx \quad (5.29)$$

$$\left| \frac{CI}{\bar{y}_e} \right|_{\text{max}} = \frac{t_{0.05\nu}}{\sqrt{n}} \left| \frac{s(\hat{x})}{\bar{y}_e(\hat{x})} \right| \quad (5.30)$$

Using the above eqs. (5.27), (5.28), (5.29) and (5.30) the average and maximum error and confidence indicator can be quantitatively estimated.

The following tables summarize the results obtained from CFD simulation with SAS (scale adaptive simulation) turbulence model for the different sizes:

	SAS (1 million cells)
Maximum relative error	0.34
Confidence interval of maximum error	0.9 [99]

Table 5.6: Calculation of uncertainties in mass burning rate predicted by CFD simulation

	SAS (1 million cells)
Maximum relative error	0.41
Confidence interval of maximum error	0.9 [99]

Table 5.7: Calculation of uncertainties in flame length predicted by CFD simulation

	SAS (1 million cells)
Maximum relative error	0.06
Confidence interval of maximum error	0.9 [99]

Table 5.8: Calculation of uncertainties in flame temperature predicted by CFD simulation

	SAS (1 million cells)
Maximum relative error	0.86
Confidence interval of maximum error	0.9 [99]

Table 5.9: Calculation of uncertainties in surface emissive power predicted by CFD simulation

The above qualitative estimations of maximum relative errors are based on single experiment and simulation. The confidence interval for maximum error is based on the analysis carried for multiple data sets of measurements and simulations on buoyant plume of helium [99]. The average values of error and confidence interval for maximum error for the present measurements and simulations can be estimated with the help of eqs. (5.27) and (5.29) provided multiplicity of experiments and simulations are available.

Chapter 6

Conclusions and Future Work

Pool fires of liquid organic peroxides show fundamentally very different characteristics e.g. generally much higher mass burning rates, large flame lengths as well as high irradiances in comparison to liquid hydrocarbon pool fires. Such peroxides present a potential risk during storage and transportation. In order to measure, calculate and develop effective methods of protection and safety distances experimental studies and CFD simulations of TBPB (tert -butyl peroxybenzoate) and TBPEH (tert-butyl peroxy-2-ethylhexanoate) pool fires were performed.

The experimental investigations led to the observation that low heat of vaporisation and readily available oxygen atoms from the thermal decomposition in the combustion zone accelerate the combustion. Therefore, very high mass burning rates were measured. Due to this fast burning, fuel Froude numbers increase significantly which finally enlarges the visibility of luminous flame. As a consequence the irradiance and surface emissive power of flames were also enhanced significantly.

Probably due to discontinuous decomposition and vaporisation of TBPB an extraordinary self sustained pulsating effect ('W' -Effect) was observed.

CFD simulation is capable to predict the mass burning rate and flame lengths of TBPB and TBPEH which are qualitatively close to the measured values. CFD Simulation estimated the safety distances accurately when predicted time averaged flame surface temperature is used. An improvement of combustion model employed in the present simulation probably will lead to a better estimation of flame characteristics.

CFD simulations to compare the large storage fire characteristics with a corresponding pool fire characteristics is also developed and tested. The simulation results are in good

agreement with experimental data on the pool fires of hydrocarbons and organic peroxides. The CFD predicted flame temperature and irradiance are comparable when the small fluctuations in the variables are neglected. The present simulations were carried out based solely on the assumption of a complete combustion without wind influence.

For future simulations, the detailed chemical reaction mechanisms and combustion of TBPB (elementary reactions) in submodels could be implemented and validated. An evaporation model (liquid phase to gas phase) which takes into account the natural convection as well, needs to be developed.

From a safety point of view, it would also be very interesting to carry out CFD study on combustion of organic peroxides in packagings. This would enable the quantitative prediction of safety-relevant parameters.

The potential threat of fire damage requires the inclusion of results from experimental studies and simulations in the safety reports for emergency planning and quantitative risk analysis. The present work can be an addition in the lessons learnt from pool fires of liquid organic peroxides, on which very few studies have been carried out so far.

References

- [1] <http://www.buncefieldinvestigation.gov.uk/images/index.htm>.
- [2] <http://www.linkassociates.com/pdfdownloads/Review%20of%20reports%20on%20Buncefield.pdf>.
- [3] B. J. McCaffrey; C. L. Beyler; G. Heskestad: *SFPE Handbook of Fire Protection Engineering*, Third Edition, 2002, ISBN: 087765-451-4.
- [4] T. Steinhaus; S. Welch; R. O. Carvel; J. L. Torero: Large-scale pool fires, *Journal of Thermal Science* (2007)101–116.
- [5] V. I. Blinov, G. N. Chudjakov: Certain laws governing diffusive burning of liquids, *Doklady Akademiia Nauk, SSR Doklady* (1957)1094–1098.
- [6] R. L. Alpert: Review of Blinov and Khudjakovs paper on certain laws governing diffusive burning of liquids by Hoyt C. Hottel, *Journal of Fire Protection Engineering* 12(2002)5–7.
- [7] K. S. Mudan: Thermal radiation hazards from hydrocarbon pool fires, *Progress in Energy and Combustion Science* 10(1984)59–80.
- [8] B. J. McCaffrey: Purely buoyant diffusion flames: some experimental results, *NBSIR 79-1910*.
- [9] J. A. Fay: Model of large pool fires, *Journal of Hazardous Materials* B136(2006)219-232.
- [10] P. K. Raj: Large LNG fire thermal radiation, *AIChE Spring Meeting* April 13(2005)219-232.

- [11] A. Schönbacher, W. Brötz, C. Balluf, D. Göck, N. Schieß: Erforschung von Schadenfeuern flssiger Kohlenwasserstoffe als Beitrag zur Sicherheit von Chemieanlagen, *Chem.-Ing.-Tech.* 57 1985, 10, 823-834.
A. Schönbacher: Source term for large open hydrocarbon pool fires, *Institute for Chemical Engineering I, University of Duisburg-Essen, Germany*, November 2009, <http://www.uni-due.de/tech1chem/index.htm>.
- [12] P. Joulain: Behaviour of pool fires: state of the Art and new insights, *Proceedings, 27th Int. Combustion Symposium*, (1999)2691–2706.
- [13] V. Babrauskas: Estimating large pool fire burning rates, *Fire Technology* 19, 4(1983)251–261.
- [14] D. D. Drysdale: Introduction to fire dynamics, *John Wiley and Sons* 2005, 2nd edition, New York, USA.
- [15] M. Hertzberg: The theory of free ambient fires. The convectively mixed combustion of fuel reservoirs *Combustion and Flame* 21(1973)195-209.
- [16] P. H. Thomas: The size of flames from natural fires, *Proc. Combust. Inst.* 9(1963)844–859.
- [17] F. R. Steward: Prediction of the height of turbulent diffusion buoyant flames, *Comb. Sc. Tech.* 2(1970)203–212.
- [18] G. Heskestad: Fire plumes, flame height, and air entrainment, *SFPE Handbook of Fire Protection Engineering*, 2002, 2-1–2-3.
- [19] W. M. G. Malalasekera; H. K. Versteeg, K. Gilchrist: A Review of Research and an Experimental study on the pulsation of buoyant diffusion flames and pool fires, *Fire and Materials* 20, 6(1996)261–271.
- [20] M. E. Schneider; L. A. Kent: Measurement of gas velocities and temperature in a large open pool fire, *Fire Technology*, (1989)51–79.
- [21] C. Kuhr; S. Staus, A. Schönbacher: Modelling of the thermal radiation of pool fires, *Progress in Computational Fluid Dynamics* 2/3/4(2003)151–156.
- [22] H. Koseki, G. W. Mulholland: The effect of diameter on the burning of crude oil pool fires, *Fire Technology* (1991)54–65.

-
- [23] J. P. Gore; G. M. Faeth: Structure and radiation properties of luminous turbulent acetylene/air diffusion flames, *Journal Heat Transfer* 1, 110(1998)173–181.
- [24] J. Meijer; A. H. Hogt; B. Fischer: Organic peroxides in radical synthesis reactions, *Akzo Nobel Polymer Chemicals Laboratory Deventer*, 1-11.
- [25] Fire and explosion hazards of organic peroxides, *The National Board of Fire underwriters, USA* (1956)1-11.
- [26] United Nations Recommendations on the Transport of Dangerous Goods, Model Regulations *16th revised edition 2009* Vol. 1, New York and Geneva, chapter 2.5.3. United Nations Recommendations on the Transport of Dangerous Goods, Manual of Tests and Criteria, *5th revised edition 2009* New York and Geneva, section 28.
- [27] P. J. Rew; W. G. Hulbert: Development of pool fire thermal radiation model, *HSE Books* Report number 99/1966, ISBN 0 7176 1084 5.
- [28] The burning velocity of Liquid Organic Peroxides, *OCED-IGUS, Sub-Group 'Organic Peroxides'* Report Nr. 1983/Ga.
- [29] M. Malow; K. D. Wehrstedt: Prediction of the self-accelerating decomposition temperature (SADT) for liquid organic peroxides from differential scanning calorimetry (DSC) measurements, *Journal of Hazardous Materials* A120(2005)21-24.
- [30] Degussa Sicherheitsdatenblatt für TBPB and TBPEH, EG Nr:1907/2006.
- [31] Akzo Nobel safety data sheet for organic peroxides, (2008)18-25.
- [32] J. H. Ferziger; M. Perić: Computational methods for fluid dynamics, *Springer-Verlag*, 2002, Berlin.
- [33] M. Greiner; A. S. Anttila: Validation of the Isis-3D computer code for simulating large pool fires under a variety of wind conditions, *Journal of Pressure Vessel Technology* 126(2004)360-366.
- [34] Y. Xin; J. P. Gore; K. B. McGrattan; R. G. Rehm; H. R. Baum: Fire dynamics simulation of a turbulent buoyant flame using a mixture-fraction-based combustion model, *Combustion and Flame* 141(2005)329-335.

- [35] R. Hilbert; F. Tap; H. E. Rabii; D. Thévenin: Impact of detailed chemistry and transport models on turbulent combustion simulations, *Progress in Energy and Combustion Science* 30(2004)61-117.
- [36] www.me.ust.hk/~mejswu/MECH343/343Thermal-01.pdf
- [37] W. F. Hemminger; G. W. H. Höhne: Grundlagen der Kalorimetrie, *Akademie-Verlag Berlin* 1980.
- [38] E. L. Charsley; S. B. Warrington: Thermal analysis - techniques applications, *Royal Society of Chemistry* 1992.
- [39] P. W. Atkins: Physikalische Chemie- 2, Wiley-VCH Weinheim (1996).
- [40] R. C. Weast; M. J. Astle: CRC Handbook of Chemistry and Physics, *CRC Press Inc*, Boca Raton, Florida, 1981.
- [41] W. Minkina; S. Dudzik: Simulation analysis of uncertainty of infrared camera measurement and processing path, *Measurement* 39(2006)758-763.
- [42] W. Minkina; S. Dudzik Infrared thermography: errors and uncertainties *John Wiley Sons* September 2009, ISBN: 978-0-470-74718-6.
- [43] <http://www.omega.com>
- [44] <http://www.infraredtraining.com/irprimer.asp>
- [45] E. P. Cuchi; J. M. Chartris; C. Lopez; J. Arnaldos: Determination of flame emissivity in hydrocarbon pool fires using infrared thermography, *Fire Technology* 39(2003)261-273.
- [46] Richtlinie für das Zuordnen sonstiger explosionsgefährlicher Stoffe zu Lagergruppen-SprengLR011, April 1981, geändert durch die Bekanntmachung vom 8. Juli 1991 (bekanntgemacht im Bundesarbeitsblatt 5/1981 S.70. berichtigt 6/1981 S.88; 11/1991 S.40).
- [47] Large Scale Fire Tests on Tertiary Butylperbenzoate and Tertiary Butylper-2-ethylhexanoate, *OCED-IGUS Subgroup 'Organic Peroxides'* BAM, Tgb. -Nr.-4-2079/81.
- [48] Ansys CFX-11 User manual.

-
- [49] T. G. Ma; J. G. Quintiere: Numerical simulation of axi-symmetric fire plumes: accuracy and limitations, *Fire Safety Journal* 38(2003)467-492.
- [50] T. Poinso, D. Veyante: Theoretical and numerical combustion, *R.T.Edwards Inc.* 2001, ISBN 978-1-930217-10-2.
- [51] J. Warnatz, U. Mass, R. W. Dibble: Combustion-physical and chemical fundamentals, modelling and simulation, experiments, pollutant formation, *Springer-Verlag* 2001.
- [52] F. R. Menter; M. Kuntz; R. Bender: A scale-adaptive simulation model for turbulent flow predictions, *AIAA* 2003-0767.
- [53] ARTIST Software, Dortmund Databank Software DDBST, Oldenburg.
- [54] N. Peters: Turbulent combustion, *Cambridge Monographs on Mechanics, Cambridge University Press*, 2000.
- [55] A. Linan: On the internal structure of laminar diffusion flames, *PhD Thesis, CalTech*, 1963, <http://etd.caltech.edu/etd/available/etd-12072005-134536/>.
- [56] B. F. Magnussen, B. H. Hjertager: On Mathematical modelling of turbulent combustion with special emphasis on soot formation and combustion, *16th Symposium (Int.) on Combustion, Cambridge, USA, The Combustion Institute, Pittsburg, Pennsylvania* (1976)719-729.
- [57] P. A. Tesner; T.D. Snegirova; V. G. Knorre: Kinetics of dispersed carbon formation, *Combustion and Flame* (1971)253-260.
- [58] G. D. Raithby: Equations of motion for reacting, particle-laden flows, *Progress report, Thermal Science Ltd.*, 1991.
- [59] R. Siegel; J. R. Howell: Thermal Radiation Heat Transfer, ISBN 0-89116-506-1.
- [60] M. Muneoz; J. Arnaldos; J. Casal; E. Planas: Analysis of the geometric and radiative characteristics of hydrocarbon pool fires, *Combustion and Flame* 139(2004)263-277.
- [61] K. D. Wehrstedt; P. A. Wandrey: Experimental investigations of pool fires of organic peroxides, *PTB Report No. PTB-W-54* PTB Brunswick, 1993, 97-108, ISBN 3-89429-359-4.

- [62] H. Chun: Experimentelle Untersuchungen und CFD-Simulationen von DTBP-Poolfeuern, *BAM, Dissertationsreihe* Band 23, 2007, Berlin, ISBN 1613-4249. <http://www.bam.de/de/service/publikationen/dissertationen.htm>.
- [63] K. B. Mishra; K. D. Wehrstedt; A. Schönbacher: Impact of fuel properties on large pool fires (hydrocarbons and organic peroxides) characteristics, *Proceedings of 6th U.S. National Combustion Meeting*, 17-20 May 2009, 11B1, 1-11, University of Michigan, Ann Arbor, USA.
- [64] K. B. Mishra; K. D. Wehrstedt; A. Schönbacher: Prediction of burning rate of an accidentally released flammable fuel by means of CFD simulation, *Proceedings of 7th International Conference on CFD in the Minerals and Process Industries*, 9-11 December 2009, 164MIS, 1-6, CSIRO, Melbourne, Australia, ISBN 978 0 643 09825.
- [65] G. Heskestad: On Q^* and dynamics of diffusion flames, *NISTIR 6030*, June 1997. <http://www.fire.nist.gov/bfrlpubs/fire97/art109.html>.
- [66] K. B. Mishra; K. D. Wehrstedt; A. Schönbacher: On the dynamics of organic peroxide pool flames, *Proceedings of 35th National Conference on Fluid Mechanics and Fluid Power (FMFP-2008)*, 11-14 December 2008, 076, 643-650, Bangalore, India.
- [67] G. Heskestad: Dynamics of the fire plumes, *Phil. Trans. R. Soc. Lond.* 356(1998)2815-2833.
- [68] K. B. Mishra; K. D. Wehrstedt; A. Schönbacher: Pool flames of organic peroxides: experiments and CFD simulations, *Proceedings of 9. Fachtagung 'Anlagen-,Arbeits- und Umweltsicherheit' (Safety and Environmental Protection Group, DECHEMA and VDI)* Köthen, Germany, ISBN 13 978-3-89746-099-7
- [69] K. B. Mishra; K. D. Wehrstedt; A. Schönbacher: Safety characteristics of organic peroxide pool flames, *Proceedings of 9th Symposium on Fire Safety Science* 21 -26 September 2008, University of Karlsruhe, Germany.
- [70] K. B. Mishra; K. D. Wehrstedt: Brennstoff und Verwendung desselben (Fuel and its use), DE 10 2009 016 492.8.

-
- [71] K. B. Mishra; K. D. Wehrstedt: Verwendung eines Brennstoffs in einem selbstunterhaltenden pulsierenden Sauerstoff-Brennstoff-Verbrennungsprozess (Use of Self-controlled oxy-fuel-pulse combustion in process industries) DE 10 2009 039 893.7.
- [72] K. B. Mishra; K. D. Wehrstedt; A. Schönbacher: Pool flames of organic peroxides: experiments and CFD simulation, *Proceedings of 32nd International Combustion Symposium* 3-9 August 2008, 4P098, University of McGill, Montreal, Canada.
- [73] K. B. Mishra; K. D. Wehrstedt; A. Schönbacher: Safety characteristics of large pool fires of organic peroxides, *AK "Sicherheits Technische Kenngrößen Kolloquium* 31 March 2009, DECHEMA Haus, Frankfurt am Main, Germany.
- [74] Personal communication with Dr. Krebs (BAM II).
- [75] J. L. Woodward: Estimating the flammable mass of a vapour cloud *Centre for Chemical Process Safety, American Institute of Chemical Engineers* New York (USA) (1998)86-88.
- [76] K. B. Mishra; K. D. Wehrstedt; A. Schönbacher: Experimental and numerical investigations of pool flames of organic peroxides, *Proceedings of PET MASCOT 08*, 21-22 October 2008, IAC-CNR, Rome, Italy.
- [77] K. B. Mishra; K. D. Wehrstedt; A. Schönbacher: Radiative characteristics of large pool fires of organic peroxides, *Proceedings of 4th European Combustion Meeting* 14-17 April 2009, Vienna University of Technology, Vienna, Austria, 810353, 1-6, ISBN 978-3-902655-06-6.
- [78] T. Blanchat; T. O. Hern; S. Kearney; A. Ricks; D. Jernigan: Validation experiments to determine radiation partitioning of heat flux to an object in a fully turbulent fire, *Proceedings of the Combustion Institute* 32(2009)2511-2518.
- [79] K. B. Mishra; K. D. Wehrstedt; A. Schönbacher: Measurement and CFD prediction of gas velocities and temperatures in large pool fires of organic peroxides, *Proceedings of 36th National Conference on Fluid Mechanics and Fluid Power (FMFP-2009)*, (17-20 December), 58-CFD-5, 1-11, Pune, India.
- [80] K. B. Mishra; K. D. Wehrstedt; A. Schönbacher: A numerical revisit of large organic peroxide fire tests, *In Progress*

- [81] A. Schönbacher; D. Göck, R. Fiala; X. Zhang: Das experimentell validierte Ballenstrahlungsmodell OSRAMO, *Technische Überwachung* 33, 6(1992)219-222.
- [82] P. K. Raj: A review of the criteria for people exposure to radiant heat fluxes from fires, *Journal of Hazardous Materials* 159(2008)61-71.
- [83] EN 1473, European Standard on the Installation and Equipment for Liquefied Natural Gas Design of On-shore Installations, prEN 1473:2005(E), Standard Version 2.1c2, Prepared by the Technical Committee CEN/TC 282, AFNOR Secretariat, Brussels. See Installation and equipment for LNG, Table A.2, p 83, The Secretariat of which is held by AFNOR, 1 September 2005.
- [84] K. B. Mishra; K. D. Wehrstedt; A. Schönbacher: Numerical prediction of safety distances from large organic peroxide pool fires, *Proceedings of the 40th International Annual Conference of the Fraunhofer ICT* 23-26 June 2009, Karlsruhe, ISSN 0722-4087.
- [85] I. Vela: CFD prediction of thermal radiation of large, sooty, hydrocarbon pool fires, *PhD Thesis* University of Duisburg-Essen, Germany, 2009.
- [86] S. B. Pope: Turbulent flows, *Cambridge University Press, London* ISBN-13: 9780521598866, ISBN-10: 0521598869.
- [87] I. Vela, H.Chun, K. B. Mishra, M. Gawlowski, P. Sudhoff, M. Rudolph, K. D. Wehrstedt, A. Schönbacher: Vorhersage der thermischen Strahlung grosser Kohlenwasserstoff- und Peroxid-Poolfeuer durch CFD Simulation, *Forschung IngenieurWesen* 73(2009)87-97.
- [88] K. B. Mishra; K. D. Wehrstedt: Ein effizienter und sauberer Brennstoff für die Prozessindustrie (An efficient and clean fuel for process industry) DE 10 2009 039 894.5.
- [89] K. B. Mishra; K. D. Wehrstedt: Energiereiche Raketentreibstoffe (High energy rocket propellents), DE 10 2010 000 261.5.
- [90] H. Chun; K. B. Mishra; I. Vela; K. D. Wehrstedt; A. Schönbacher: Mass burning rates and flame heights of di-tert-butyl peroxide pool fires - Experimental investigation and CFD simulation, In preparation.

-
- [91] A. Schönbacher; B. Arnold; K. Banhardt; V. Bieller; H. Kasper; M. Kaufman; R. Lucas; N. Scheiß: , *21 Symp.(Intl.) on Combust., The Combustion Institute* 1986.
- [92] K. B. Mishra, K. D. Wehrstedt: PEROXY-BAM[®] Brenner für die Prozessindustrie (PEROXY-BAM[®] Burner for process industries), DE 30 2009 069 918.6.
- [93] Hu L. H., Liu S., Peng W., Huo R.: Experimental study on burning rates of square/rectangular gasoline and methanol pool fires under longitudinal air flow in a wind tunnel *Journal of Hazardous Materials* 169(2009)972-979.
- [94] M. Hailwood; M. Gawlowski; B. Schalau; A. Schönbacher: Conclusions drawn from the buncefield and naples incidents regarding the utilization of consequence models *Chem. Eng. Technol.* 32, 2(2009)207-231.
- [95] J. Inczédy; T. Lengyel; A. M. Ure: Compendium of analytical nomenclature, definitive rules 1997 *International Union of Pure and Applied Chemistry* Third Edition.
- [96] Heat flux transducers and infrared radiometers for the direct measurement of heat transfer rates, *64 Series* Meditherm corporation, Alabama, USA.
- [97] <http://www.hse.gov.uk/offshore/strategy/pool.htm>
- [98] James T. Nakos: Uncertainty analysis of steady state incident heat flux measurements in hydrocarbon fuel fires, *SAND2005-7144* Sandia National Laboratories, USA.
- [99] W. L. Oberkampf; M. F. Barone: Measures of agreement between computation and experiment: Validation metrics, *Journal of Computational Physics* 217(2006)536.
- [100] Personal communication with Dr. Rudolph (BAM II).
- [101] K. B. Mishra, K. D. Wehrstedt: Brenner für Peroxy-Brennstoffe und Ofen mit einem solchen Brenner (Peroxy-fuel burners and furnace with such a burner), DE 10 2010 000 248.8.
- [102] B. F. Magnussen: The eddy dissipation concept: A bridge between science and technology *Invited paper at ECCOMAS Thematic Conference on Computational Combustion* Lisbon, June 21-24, 2005.

- [103] K. B. Mishra, K. D. Wehrstedt: Brennstoffkontrollierte Impulsverbrennung in Industrietrocknern (Fuel driven pulse combustion in drying industries), DE 10 2010 016 831.9.
- [104] K. B. Mishra, K. D. Wehrstedt: Brennstoffgemisch und Anwendung derselben in Gasturbinen (Hybrid Fuel and its applications in gas turbine), DE 10 2010 016 833.5.
- [105] K. B. Mishra, K. D. Wehrstedt: Geräuschreduktion in Triebwerken durch brennstoffkontrollierte Impulsverbrennung (Noise reduction through fuel driven pulse combustion in jet engines), DE 10 2010 016 832.7.
- [106] K. B. Mishra, K. D. Wehrstedt: Fuel and use thereof, PCT/EP2010/054544.
- [107] K. B. Mishra, K. D. Wehrstedt: EP 008 990 319, PEROXY-BAM[®] Burner.

List of trade marks, patents and publications

Trade Marks

- K. B. Mishra, K. D. Wehrstedt, DE 30 2009 069 918.6 PEROXY-BAM[®] Brenner.
- K. B. Mishra, K. D. Wehrstedt, EP 008 990 319, PEROXY-BAM[®] Burner.

Patents

- K. B. Mishra, K. D. Wehrstedt, Brennstoff und Verwendung desselben (Fuel and its use), DE 10 2009 016 492.8.
- K. B. Mishra, K. D. Wehrstedt, Selbstunterhaltende pulsierende Sauerstoff-Brennstoff-Verbrennung (Self-controlled oxy-fuel-pulse combustion), DE 10 2009 039 893.7.
- K. B. Mishra, K. D. Wehrstedt, Ein effizienter und sauberer Brennstoff für die Prozessindustrie (An efficient and clean fuel for process industries), DE 10 2009 039 894.5.
- K. B. Mishra, K. D. Wehrstedt, Brenner für Peroxy-Brennstoffe und Ofen mit einem solchen Brenner (Peroxy-fuel burners and furnace with such a burner), DE 10 2010 000 248.8.
- K. B. Mishra, K. D. Wehrstedt, Energiereiche Raketentreibstoffe (High energy rocket propellents), DE 10 2010 000 261.5.
- K. B. Mishra, K. D. Wehrstedt, Brennstoffkontrollierte Impulsverbrennung in Industrietrocknern (Fuel driven pulse combustion in drying industries), DE 10 2010 016 831.9.

- K. B. Mishra, K. D. Wehrstedt, Brennstoffgemisch und Anwendung derselben in Gasturbinen (Hybrid Fuel and its applications in gas turbine), DE 10 2010 016 833.5.
- K. B. Mishra, K. D. Wehrstedt, Geräuschreduktion in Triebwerken durch brennstoffkontrollierte Impulsverbrennung (Noise reduction through fuel driven pulse combustion in jet engines), DE 10 2010 016 832.7.
- K. B. Mishra, K. D. Wehrstedt, Fuel and use thereof, PCT/EP2010/054544.

Publications

International Journals

- I. Vela, H.Chun, K. B. Mishra, M. Gawlowski, P. Sudhoff, M. Rudolph, K. D. Wehrstedt, A. Schönbacher, Vorhersage der thermischen Strahlung grosser Kohlenwasserstoff- und Peroxid-Poolfeuer durch CFD Simulation, Forschung Ingenieurwesen, 2009, 73, 87-97, doi:10.1007/s10010-009-0094-3.
- H. Chun, K. B. Mishra, I. Vela, K. D. Wehrstedt, A. Schönbacher, Mass burning rates and flame heights of di-tert-butyl peroxide pool fires, In progress for publication in Journal of Hazardous Materials.
- K. B. Mishra, K. D. Wehrstedt, A. Schönbacher, Numerical revisit of large packaged organic peroxides fire tests, In progress for publication in Journal of Hazardous Materials.

International Conferences

- K. B. Mishra, K. D. Wehrstedt, A. Schönbacher, Characterisation of pool fires of organic compounds containing oxygen atoms, Accepted for publication in 13th International Symposium on Loss Prevention and Safety Promotion in the Process Industries, Brugge, 6-9 June, 2010, Belgium.
- K. B. Mishra, K. D. Wehrstedt, A. Schönbacher, Prediction of burning rate of an accidentally released flammable fuel by means of CFD simulation from large organic peroxide pool fires, Proceedings of 7th International Conference on CFD in Minerals and Process Industries, CSIRO, 9-11 Dec. 2009, Melbourne, Australia, 164MIS, 1-6, ISBN 978 0 643 09825.

- K. B. Mishra, K. D. Wehrstedt, A. Schönbacher, Numerical prediction of safety distances from large organic peroxide pool fires, Proceedings of the 40th International Annual Conference of the Fraunhofer ICT, 23-26 June 2009, Karlsruhe, ISSN 0722-4087.
- K. B. Mishra, K. D. Wehrstedt, A. Schönbacher, Impact of fuel properties on large pool fires (hydrocarbons and organic peroxides) characteristics, Proceedings of 6th U.S. National Combustion Meeting, May 17-20. 2009, University of Michigan, Ann Arbor, 11B1, 1-11.
- K. B. Mishra, K. D. Wehrstedt, A. Schönbacher, Radiative characteristics of large pool fires of organic peroxides, Proceedings of 4th European Combustion Meeting, 14-17 April 2009, Vienna University of Technology, Austria, 810353, 1-6, ISBN 978-3-902655-06-6.

National Conferences

- K. B. Mishra, K. D. Wehrstedt, A. Schönbacher, Measurement and CFD prediction of gas velocities and temperatures in large pool fires of organic peroxides, Proceedings of 36th National Conference on Fluid Mechanics and Fluid Power (FMFP-2009) (17-20 December) Pune, India, 58-CFD-5, 1-11.
- K. B. Mishra, K. D. Wehrstedt, A. Schönbacher, On the dynamics of organic peroxide pool flames, Proceedings of 35th National Conference on Fluid Mechanics and Fluid Power (FMFP-2008) (11-14 December) Bangalore, India, FMFP-08, 076, 643-650.

Posters and Presentations

- K. B. Mishra, K. D. Wehrstedt, A. Schönbacher, Pool flames of organic peroxides: experiments and CFD simulations, Proceedings of 9. Fachachtung 'Anlagen-, Arbeits- und Umweltsicherheit' (Safety and environmental protection group, DECHEMA and VDI) (6 7 November 2008), Köthen, Germany, ISBN 13 978-3-89746-099-7.
- K. B. Mishra, K. D. Wehrstedt, A. Schönbacher, Safety characteristics of organic peroxide pool flames, Proceedings of 9th International Symposium on Fire Safety Science (21 -26 September 2008), University of Karlsruhe, Germany.

- K. B. Mishra, K. D. Wehrstedt, A. Schönbacher, Pool flames of organic peroxides: experiments and CFD simulation, 4P098, Proceedings of 32nd International Combustion Symposium (3-9 August 2008), University of McGill, Montreal, Canada.
- K. B. Mishra, K. D. Wehrstedt, A. Schönbacher, Experimental and numerical investigations of pool flames of organic peroxides, Proceedings of PET MASCOT-08 (21-22 October 2008), IAC-CNR, Rome, Italy.
- K. B. Mishra, K. D. Wehrstedt, A. Schönbacher, Numerical studies on the pool fire characteristics of organic peroxides, 28-30 October 2009, MASCOT-09, IAC-CNR, Rome, Italy.
- K. B. Mishra, K. D. Wehrstedt, A. Schönbacher, Safety characteristics of large pool fires of organic peroxides, 31 March 2009, AK "Sicherheits technische Kenngrößen Kolloquium, DECHEMA Haus, Frankfurt am Main, Germany.
- K. B. Mishra, K. D. Wehrstedt, A. Schönbacher, Turbulent combustion in large pool fires of organic peroxides, 25-29 May 2009, Short course on Turbulent Combustion, von Karman Institute for Fluid Dynamics, Brussels, Belgium.

Curriculum Vitae

Personal Details

- Name: Kirti Bhushan Mishra
- Date of Birth: 19-11-1978
- Place of Birth: Cuttack, India
- Nationality: Indian
- Gender: Male
- Marital Status: Single

Education

- 01.02.2007 – 12.05.2010 PhD in Fire safety engineering
Institute for Combustion and Gas dynamics, Department of Mechanical Engineering, University of Duisburg-Essen, Germany.
- 01.08.2001 – 20.10.2003 Master of Technology M.Tech (Hons) in Fluid mechanics and machines
Maulana Azad National Institute of Technology, Bhopal, India.
- 01.07.1997 – 01.07.2001 Bachelor of Engineering B.E.(Hons) in Mechanical engineering
Rajiv Gandhi University of Technology, Bhopal, India.

Work Experience

- 16.06.2010 – till date Junior Scientist
Division II.2, “Reactive Substances and Systems“ BAM Federal Institute for Materials Research and Testing, Berlin, Germany.
- 01.08.2005 – 31.01.2007 Scientific Co-Worker
Department of Chemical Engineering, University of Erlangen-Nuremberg, Erlangen, Germany.
- 20.01.2003 – 30.07.2005 Lecturer
Department of Mechanical Engineering, Madhav Institute of Technology and Science, Gwalior, India.

School Education

- 01.07.1984 – 01.07.1994 Matriculation (Distinction)
- 01.08.1994 – 01.06.1996 Senior Secondary School (Distinction) Madhya Pradesh
Board of Secondary Education, Bhopal, India

Berlin 16 July 2010